Synthesis and characterization of homogeneous interstitial solutions of nitrogen and carbon in iron-based lattices

Brink, Bastian Klüge

Publication date:
2015

Document Version
Publisher's PDF, also known as Version of record

Synthesis and characterization of homogeneous interstitial solutions of nitrogen and carbon in iron-based lattices

PhD Thesis

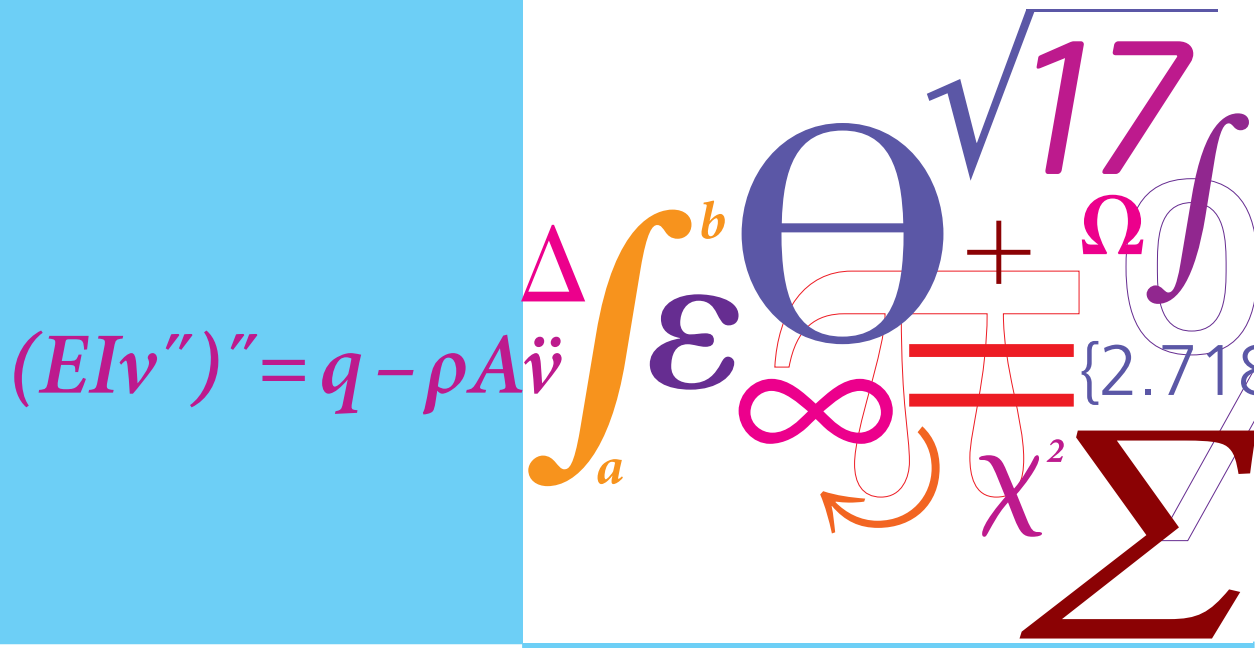

Bastian Klüge Brink
June 2015

DTU Mechanical Engineering
Department of Mechanical Engineering

Synthesis and characterization of homogeneous interstitial solutions of nitrogen and carbon in iron-based lattices

PhD thesis

Bastian Klüge Brink

Section of Materials and Surface Engineering
Department of Mechanical Engineering
Technical University of Denmark
June 2015

"The true worth of an experimenter consists in his pursuing not only what he seeks in his experiment, but also what he did not seek."

-Claude Bernard

Preface and acknowledgements

The present dissertation is submitted in partial fulfillment of the requirements for the PhD degree at the Technical University of Denmark. The presented work has been carried out at the Section of Materials and Surface Engineering, Department of Mechanical Engineering, during the period July 2012 to June 2015 under the supervision of Professor Marcel A. J. Somers and co-supervision of Senior Researcher Thomas L. Christiansen and Associate Professor Kenny Ståhl (DTU Chemistry). The PhD project was part of the research project ThInSol (Thermodynamics of Interstitial Solutions in Cubic and Hexagonal Host Lattices), financially supported by the Danish Research Council for Independent Research, Technology and Production Sciences (FTP), under grant No. 11-106293.

First and foremost, I would like to thank my supervisors Marcel A. J. Somers, Thomas L. Christiansen and Kenny Ståhl for their help and guidance throughout the project and for always being available for questions and inspiring scientific discussions. Additionally, I would also like to thank Kenny Ståhl for accompanying me on trips to various synchrotron and neutron facilities around Europe.

For practical assistance with measurements and providing insight into their respective fields, I would like to thank Associate Professor Mikkel Fougt Hansen for vibrating sample magnetometry, Professor Cathrine Frandsen for Mössbauer spectroscopy and Research Engineer Jette Oddershede for X-ray absorption spectroscopy and simulations of crystal defects. I also would like to thank Morten Bjørn Bakkedal for collaboration on the ThInSol project and Jeppe Fock for assistance with fitting of Mössbauer spectra.

In connection with my visits to various synchrotron and neutron research facilities, I would like to acknowledge the help of Dörthe Haase and Stefan Carlson at MAX-lab, Michael Krisch and Christoph Sahle at the European Synchrotron Radiation Facility (ESRF),

Robert C. Wimpory at BER II, Helmholtz-Zentrum Berlin (HZB) and Přemysl Beran at the Nuclear Physics Institute, Academy of Sciences of the Czech Republic (ASCR). Financial support for travel expenses from DanScatt, ESRF and the European Commission under the FP7 NMI3-II Framework Programme is gratefully acknowledged.

I would like to thank my friends and family for their support and past and present colleagues at the Section of Materials and Surface Engineering and the X-Ray Group at DTU Chemistry for contributing to a pleasant and engaging work environment. Finally, I would like to thank my loving wife, Cecilie, for her endless support and encouragement.

Kgs. Lyngby, June 30th 2015

Bastian Klüge Brink

Abstract

Since the advent of gaseous nitriding and nitrocarburizing processes in the early 20th century, numerous process variants and applications have been developed. Improved performance with respect to fatigue, wear and corrosion can be obtained for treated steel components. Despite the advantages and widespread application, the current understanding of the thermodynamics and kinetics governing the processes, as well as the resulting crystal structures and magnetic properties, is still far from complete.

An incomplete fundamental description hinders possible process optimization and has motivated the current work in synthesis and characterization of interstitial solutions of nitrogen and carbon in iron-based lattices. In order to avoid the influences of gradients in composition and residual stresses, which are typically found in treated surface layers, homogenous samples are needed. These were prepared from pure iron or austenitic stainless steel using gaseous mixtures of ammonia, hydrogen, acetylene and propene at elevated temperatures.

Structural and magnetic properties have been characterized with neutron diffraction, vibrating sample magnetometry and Mössbauer spectroscopy. Thermal expansion and decomposition was studied in inert atmospheres with *in situ* synchrotron X-ray diffraction. Thermal decomposition sequences for iron carbides and carbonitrides, as well as for so-called expanded austenite, were established.

In ε-iron nitride, partial substitution of nitrogen by carbon causes an increase in Curie temperature and specific magnetization. Changes in interstitial ordering were deduced from the observed effects on lattice parameters and related to relatively favorable interactions between nitrogen and carbon.

At room temperature expanded austenite is found to be paramagnetic for high and low nitrogen contents but ferromagnetic for intermediate contents. An anomalous variation in thermal expansion coefficients with interstitial content is caused by spontaneous volume magnetostriction in the ferromagnetic state.

Several structural models have previously been proposed for expanded austenite, but all have failed to successfully describe all features of X-ray diffraction data. In the current evaluation of diffraction data, the effects of stacking faults on *hkl*-dependent shifts of Bragg reflections were included. Comparison of simulations with experimental data does, however, show that the stacking fault model is not entirely acceptable. The apparent anisotropic deviations from cubic symmetry currently lack an exact quantitative interpretation.

Dansk resumé

Siden gas-fase nitrering og nitrocarburering blev udviklet som tekniske processer i begyndelsen af det forrige århundrede, er adskillige proces-varianter med udvidede anvendelsesmuligheder blevet tilføjet. Forbedret modstandsdygtighed overfor udmattelse, slid og korrosion kan opnås for behandlede stålkomponenter. På trods af fordelene og udbredt anvendelse, er den nuværende forståelse af den underliggende kinetik og termodynamik bag processerne, samt de resulterende krystalstrukturer og magnetiske egenskaber, langt fra fuldstændig.

En ufuldstændig grundlæggende beskrivelse hindrer mulig procesoptimering og har været motivationen for dette arbejde med syntese og karakterisering af interstitielle opløsninger af nitrogen og carbon i jern-baserede krystalgitre. For at undgå indflydelsen fra gradienter i komposition og residualspændinger, hvilke typisk forefindes i behandlede overflader, er homogene prøver nødvendige. Disse blev fremstillet af rent jern eller austenitisk rustfrit stål under opvarmning i gasblandinger af ammoniak, hydrogen, acetylen og propen.

Strukturelle og magnetiske egenskaber er blevet karakteriseret med neutrondiffraktion, magnetometri og Mössbauer spektroskopi. Termisk ekspansion og dekomponering i en inert atmosfære blev undersøgt med *in situ* synchrotron røntgendiffraktion. Termiske dekomponeringssekvenser er blevet fastlagt for jernkarbider og carbonitrider samt for såkaldt ekspanderet austenit.

I ε-jernnitrid bevirker partiel substitution af nitrogen med carbon en forhøjet Curie temperatur og specifik magnetisering. Ændringer i interstitiel ordning blev udledt fra observerede påvirkninger af gitterparametre og er relateret til forholdsvis favorable interaktioner mellem nitrogen og carbon.

Ved stuetemperatur er ekspanderet austenit paramagnetisk for både lavt og højt nitrogenindhold men ferromagnetisk for mellemliggende indhold. Spontan volumenmagnetostriktion i den ferromagnetiske tilstand forårsager en anomal variation i termisk ekspansionskoefficient ved ændringer i interstitielt indhold.

Adskillige strukturmodeller har tidligere været foreslået for ekspanderet austenit, men ingen af disse modeller har kunnet forklare de observerede diffraktionsdata i tilfredsstillende grad. Den indeværende evaluering af diffraktionsdata har inkluderet indflydelsen af stablefejl på *hkl*-afhængige forskydninger af Bragg-reflekser. Sammenligning af simuleringer og eksperimentelle data viser dog at stablefejlsmodellen ikke er helt tilfredsstillende. På nuværende tidspunkt mangler en eksakt kvantitativ fortolkning af den tilsyneladende anisotropiske afvigelse fra kubisk symmetri.

Publications and conference contributions

Publications

I Thermal expansion and phase transformations of nitrogen-expanded austenite studied with *in situ* synchrotron X-ray diffraction. Bastian Brink, Kenny Ståhl, Thomas L. Christiansen and Marcel A. J. Somers. *J. Appl. Cryst.* (2014). **47**, 819–826. (Appendix A.1)

Conference contributions

I Thermal Behavior of Expanded Austenite: Determination of Thermal Expansion and Decomposition using in-situ Synchrotron X-ray Diffraction. Bastian Brink, Kenny Ståhl, Thomas L. Christiansen & Marcel A. J. Somers. Poster at Danish Crystallographers Meeting (DKM43), Kgs. Lyngby, Denmark, 2014.

II Synchrotron X-ray Diffraction Study of Thermal Decomposition of Expanded Austenite. Bastian Brink, Kenny Ståhl, Thomas L. Christiansen & Marcel A. J. Somers. Poster at the European Powder Diffraction Conference (EPDIC14), Aarhus, Denmark, 2014.

III Thermal Stability and Decomposition of Carbon and Nitrogen Expanded Austenite. Bastian Brink, Kenny Ståhl, Thomas L. Christiansen and Marcel A. J. Somers. Talk at the Material Science & Technology Conference (MS&T'14), Pittsburgh, PA, USA, 2014.

List of abbreviations

ASCR	The Academy of Sciences of the Czech Republic (Nuclear Physics Institute in Řež, the Czech Republic)
b.c.c.	Body-centered cubic
ESRF	the European Synchrotron Radiation Facility (Grenoble, France)
EXAFS	Extended X-ray Absorption Fine Structure
f.c.c.	Face-centered cubic
FWHM	Full Width at Half Maximum
h.c.p.	Hexagonal close-packed
HZB	Helmholtz-Zentrum Berlin für Materialien und Energie (Berlin, Germany)
MAX-lab	National electron accelerator laboratory for synchrotron radiation research, nuclear physics and accelerator physics (Lund University, Sweden)
RT	Room temperature
SEM	Scanning Electron Microscopy
VSM	Vibrating Sample Magnetometer / Vibrating Sample Magnetometry
XRD	X-ray Diffraction
XRS	X-ray Raman Spectroscopy

Contents

Chapter 1

Introduction

Gaseous nitriding and nitrocarburizing are versatile thermochemical surface treatments with widespread applications. Treated components exhibit improved performance with respect to fatigue, wear and corrosion. Nitriding involves introduction of nitrogen into the surface of a component and was developed as a technical process in the early 20th century (Machlet, 1913; Fry, 1923). Since then, numerous process variants have been developed, one of which is nitrocarburizing, where carbon is introduced simultaneously with nitrogen. Different media, like plasmas and salt baths, can be used as nitrogen (and carbon) sources, but only gaseous processes allow for precise control of the thermodynamic conditions (Mittemeijer, 2013).

The case developing during treatment consists of a compound layer at the surface with enhanced wear and tribological performance and a diffusion zone underneath, which enhances fatigue performance. Nitriding is traditionally performed in the temperature range 750 – 800 K, with development of a diffusion zone as the primary purpose, while the main objective of nitrocarburizing is the development of a compound layer, with treatments usually performed at 810 – 860 K (Somers, 2014). The compound layer consists of iron (carbo)nitrides, γ'-Fe_4N_{1+x} and ε-$Fe_2(N,C)_{1-z}$, and the diffusion zone of a supersaturated interstitial solution of nitrogen (and carbon) in a metallic matrix and alloying element (carbo)nitrides (e.g., CrN and AlN), in the case of alloyed steels.

The relatively low temperatures used for nitriding and nitrocarburizing offer some advantages compared to traditional carburizing. Since the surface hardening effect is

obtained without a martensitic transformation of the material, major dimensional changes and distortions are avoided. The numerous possible applications, e.g. gears, valve components, and forging/forming dies, cover a wide range of industries including automotive, aerospace and nuclear, to name a few.

Despite the collective experience of approximately one century of nitriding, the understanding of the thermodynamics and kinetics governing the processes is still far from complete. This hinders successful modelling and therefore also optimization of the processes. The purpose of this work is to contribute to the understanding of the major phases developing on nitriding and nitrocarburizing of iron and steel, by controlled synthesis and characterization of interstitial solid solutions of nitrogen and carbon in iron-based lattices.

1.1 Dissertation outline

The first part of this dissertation consists of chapters introducing theory and applied experimental principles. Chapter 2 summarizes thermodynamic considerations and literature on the structural properties of relevant iron-based nitrides and carbides as well as nitrogen and carbon expanded austenite. Chapter 3 introduces the primary utilized experimental techniques: X-ray and neutron diffraction, Mössbauer spectroscopy and vibrating sample magnetometry. The subsequent chapters present the performed experimental work and obtained results.

Chapter 4 describes synthesis of phases in the iron-carbon-nitrogen system by gaseous nitrocarburizing in atmospheres of ammonia, hydrogen and propene. The process involves a pretreatment for preparing porous iron foils, which can be used in order to obtain homogeneous samples of iron carbides and nitrides. Thermal expansion and decomposition of the resulting structures has been studied with *in situ* synchrotron X-ray diffraction.

Chapter 5 presents results on the changes in interstitial ordering, lattice parameters and magnetic properties of ε-iron nitride due to partial substitution of nitrogen by carbon. Thermal expansion coefficients are also evaluated. Experimental data are obtained with neutron diffraction, vibrating sample magnetometry and Mössbauer spectroscopy.

Chapter 6 contains results of the investigation of nitrogen and carbon expanded austenite synthesized from powder or thin foils of AISI 316 austenitic stainless steel. Thermal expansion and decomposition has been studied with *in situ* synchrotron X-ray diffraction and magnetic and structural properties with vibrating sample magnetometry and Mössbauer spectroscopy. The first part of the study, concerning nitrogen expanded austenite, is published in Journal of Applied Crystallography (vol. 47, pages 819–826), which is included in Appendix A.1.

Chapter 7 evaluates the currently incompletely structural description of expanded austenite. Several structural models have been proposed, but all have failed to successfully describe all features of X-ray diffraction data for this structure. In the current work, the effects of dislocations described by so-called modified Williamson-Hall plots and simulations of the effects of stacking faults are compared to experimental diffraction data for nitrogen expanded austenite.

General conclusions and a summary of obtained results are given in Chapter 8. In addition, two appendices are included: Appendix A contains reprints of published scientific papers[1] and Appendix B describes additional experimental details regarding synthesis of nitrogen expanded austenite and X-ray Raman spectroscopy.

[1] Note that, at the time of completion of this dissertation, only one publication (Appendix A.1) has been finalized. Additional publications based on the remainder of obtained scientific results are in preparation.

Chapter 2

Background and literature review

In order to obtain a comprehensive understanding of nitriding and nitrocarburizing processes, an accurate description of the governing thermodynamics and kinetics is essential. This chapter introduces key thermodynamic considerations and summarizes available literature on the structural and magnetic properties of relevant iron-based nitrides and carbides. The last section introduces so-called expanded austenite, which is produced from low temperature treatments (nitriding, carburizing and nitrocarburizing) of austenitic stainless steel.

2.1 Thermodynamics

The binary phase diagrams for the iron-carbon and iron-nitrogen systems are given in Figure 2.1. These show stability regions for phases as a function of temperature and composition at 1 atm pressure. For the iron-carbon system both the stable diagram, including the phase graphite, and the technologically important metastable diagram, including the phase cementite, Fe_3C, are shown. Cementite, as well as other iron carbides, is unstable at normal temperature and pressures and prone to decomposition into iron and carbon (graphite), although kinetically hindered at low temperatures.

Molecular nitrogen gas, N_2, plays a similar role for the iron-nitrogen system as graphite does for the iron-carbon system. The presented iron-nitrogen phase diagram is, in fact, also metastable with iron nitrides being unstable with respect to formation of iron and

molecular nitrogen. Nitriding of iron-based components is thus only possible due to the limited kinetics of this decomposition. Significant porosity development due to formation of N_2 can, however, occur during nitriding as a consequence of non-negligible kinetics at the nitriding temperature.

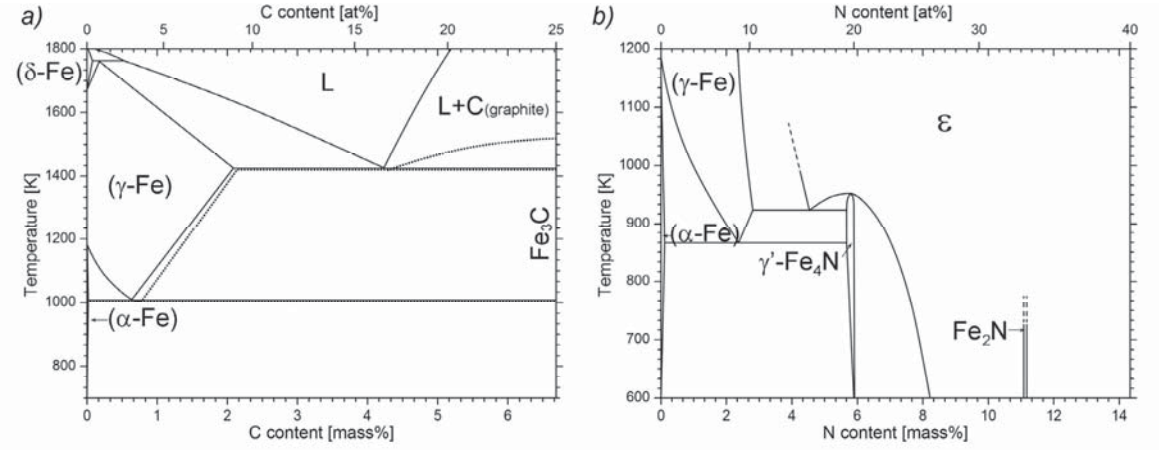

Figure 2.1: Binary phase diagrams for *a*) Fe-C (solid lines) and metastable Fe-Fe_3C (dotted lines) and *b*) the Fe-N system. Reproduced from Massalski (1996).

Thermodynamic control of nitriding and nitrocarburizing is achieved via gaseous processes. Due to the stability of N_2 there is virtually no thermal dissociation to atomic nitrogen within the typical temperature range used for nitriding. At these temperatures, nitrogen gas is thus only suitable as a nitriding media after it has been dissociated in plasma. In contrast, NH_3 exhibits a suitable dissociation rate in contact with iron or steel surfaces, allowing for precise control of the thermodynamic conditions by nitriding in gas mixtures of ammonia and hydrogen.

2.1.1 Gas-solid reactions, potentials and activities

Since the chemical potential of a species is a state variable and thus independent of the route taken to reach a certain state, nitriding in gas mixtures of ammonia and hydrogen can be formally considered as the result of bringing N_2 gas into contact with a metallic surface under a certain pressure (Mittemeijer & Slycke, 1996). The initial adsorption of nitrogen can be viewed as the sum of the following reactions:

$$NH_3 \rightleftarrows {}^1/_2\, N_2 + {}^3/_2\, H_2 \tag{2.1}$$

$${}^1/_2\, N_2 \rightleftarrows N_{ad} \tag{2.2}$$

The adsorbed nitrogen, N_{ad}, may then follow one of two routes; either diffusing into the solid phase resulting in the desired effect of atomic nitrogen dissolved in the metallic matrix, represented as [N]:

$$N_{ad} \rightleftarrows [N] \tag{2.3}$$

or recombine to form molecular nitrogen and desorbing from the surface, which counteracts nitriding:

$$N_{ad} + N_{ad} \rightleftarrows N_2 \tag{2.4}$$

Although reaction (2.4) is thermodynamically favored, the reaction rate is comparatively low (Grabke, 1968a) and can thus be neglected. Combining reactions (2.1), (2.2) and (2.3) yields the total nitriding reaction:

$$NH_3 \rightleftarrows [N] + {}^3/_2\, H_2 \tag{2.5}$$

It should be noted that the actual reaction involves adsorbed ammonia molecules that dissociate by stepwise removal of hydrogen atoms at the surface (Grabke, 1968b).

Thermodynamically, ammonia gas should be practically fully decomposed into nitrogen and hydrogen gas (catalytically activated by iron-based surfaces) at typical nitriding temperatures and pressure, according to reaction (2.1). Nitriding in ammonia-hydrogen gas mixtures is thus only possible due to the slow kinetics of ammonia dissociation. A stationary gas atmosphere is therefore inappropriate for controlled nitriding where a sufficiently high flow rate should be maintained in order to avoid dissociation.

Nitrocarburizing may be achieved by addition of suitable carbon sources to the gas mixture, for example CO and CO_2. The presence of both oxygen and hydrogen does, however, complicate thermodynamic control of the gas atmosphere due to side reactions involving water, H_2O. This is avoided in gas mixtures based on unsaturated hydrocarbons like acetylene (C_2H_2) or propene (C_3H_6), where the carburizing reaction proceeds by (Pedersen *et al.*, 2011):

$$C_xH_y \rightleftarrows x\,[C] + {}^y/_2\, H_2 \tag{2.6}$$

Assuming ideal gasses, the activity of dissolved nitrogen, a_N, and carbon, a_C, in the solid phase, can be defined as follows at 1 atm pressure:

$$a_N = K_{2.5} \cdot K_N \qquad K_N = \frac{p_{NH_3}}{p_{H_2}^{3/2}} \tag{2.8}$$

$$a_C = K_{2.6} \cdot K_C \qquad K_C = \sqrt[x]{\frac{p_{C_xH_y}}{p_{H_2}^{y/2}}} \tag{2.9}$$

where $K_{2.5}$ and $K_{2.6}$ are the temperature-dependent equilibrium constants of reactions (2.5) and (2.6), respectively. The process is controlled by adjusting the so-called nitriding potential, K_N, and carburizing potential, K_C, where p_{NH_3}, p_{H_2} and $p_{C_xH_y}$ are the partial pressures (in atm) of the gas components NH_3, H_2 and C_xH_y.

2.1.2 Local gas-solid equilibria and stationary states

Iron nitrides are metastable with respect to decomposition into iron and molecular nitrogen at normal temperature and pressures, but nitriding in ammonia-hydrogen gas mixtures at 1 atm corresponds to an equilibrium pressure of (hypothetical) N_2 several orders of magnitude higher than atmospheric pressure. The so-called Lehrer diagram (Lehrer, 1930) depicts the stability regions of iron-based nitrides in flowing ammonia-hydrogen gas mixtures (Figure 2.2).

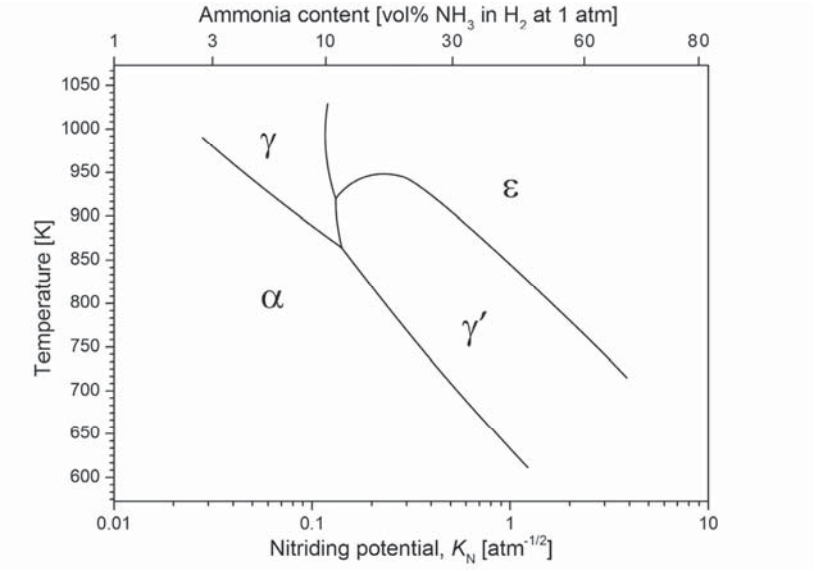

Figure 2.2: Lehrer diagram (Lehrer, 1930), depicting the stability of Fe–N phases as a function of temperature and nitriding potential (and the corresponding ammonia content in an NH_3-H_2 gas mixture at 1 atm). Reproduced from Mittemeijer & Slycke (1996).

Lines in the Lehrer diagram represent two coexisting solid phases in equilibrium with each other and the nitriding atmosphere, i.e. an imposed three-phase equilibrium. The nitriding potentials at each temperature (as well as activities and chemical potentials of nitrogen) are equal for the two iron-nitrogen phases. Similarly, the coexistence of three solid phases in equilibrium with a gas phase, i.e. a four-phase equilibrium, is represented by a point.

Due to the metastability of iron nitrides and carbides, thermodynamic equilibrium is only (at best) established at the very surface of a component in contact with the nitriding (or nitrocarburizing) atmosphere. The activities given in equations (2.8) and (2.9) are valid for local equilibrium between the gas phase and dissolved nitrogen and carbon in the solid phase. Such (local) equilibrium is, however, not always established and becomes increasingly difficult to realize for nitriding at high temperatures or high nitriding potentials (Mittemeijer, 2013). This is due to non-negligible recombination and desorption of adsorbed nitrogen according to reaction (2.4). In the case of no significant diffusion of dissolved nitrogen from the surface into the bulk of the specimen, a so-called stationary state is established when the rate of nitrogen absorption equals that of N_2 desorption. In this case, the activity (and chemical potential) of the dissolved nitrogen at the surface of the specimen is lower than that determined from the gas composition. Negligible nitrogen diffusion may be obtained for homogeneous samples or in the later stages of nitriding.

Similar to the Lehrer diagram for the Fe-N system, a phase stability diagram for the Fe–N–C system, as well as several isothermal sections of the ternary phase diagram, have been published (Naumann & Langenscheid, 1965a; b). The results were obtained from nitrocarburizing of iron powder in flowing NH_3–H_2–CO gas mixtures. The water vapor content in the applied gas mixtures was not provided, implying that the carbon activities in the reported diagrams are undetermined. This problem may be circumvented by using unsaturated hydrocarbons like acetylene (C_2H_2) or propene (C_3H_6). Since no oxygen is present, such gasses offer easier thermodynamic control of the gas atmosphere.

2.2 Iron-based nitrides and carbides

The structures of solid solutions of nitrogen and carbon in iron and its alloys are best considered in terms of hexagonal close-packing (h.c.p.), body-centered cubic (b.c.c.) and face-centered cubic (f.c.c.) unit cells. At ambient conditions pure iron exhibits the b.c.c. crystal structure and is denoted α-Fe or ferrite. The structure changes to f.c.c at 1185 K and this configuration is named γ-Fe or austenite. Two additional allotropes of iron exist; a high-temperature b.c.c. structure (δ-Fe) and a high-pressure h.c.p. structure (ε-Fe). In both ferrite and austenite, solid solutions of nitrogen and carbon are formed by these occupying interstitial sites. There are two distinct types of available sites; octahedral and tetrahedral

(Figure 2.3). In f.c.c lattices the available volume is largest for the octahedral positions and these are therefore preferred for dissolution in austenite. The interstitial atom is surrounded by six Fe atoms at equal distance and is thus associated with an isotropic local distortion of the lattice. The average lattice parameter increases with increasing interstitial content.

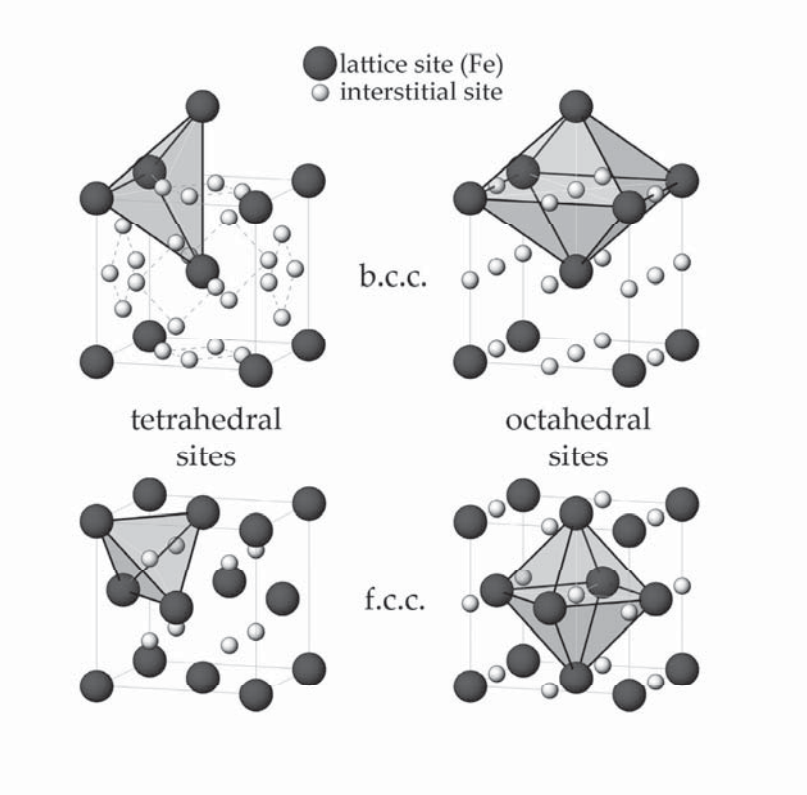

Figure 2.3: Octahedral and tetrahedral interstitial positions in face-centered cubic (f.c.c.) and body-centered cubic (b.c.c.) lattices.

In the b.c.c. lattice of ferrite, tetrahedral holes are largest, but the distorted octahedral sites are still preferred. This can be explained from the favorable relief of strain by displacement of the two nearest neighbor iron atoms (vertical in Figure 2.3). In comparison, more energy would be needed to displace the four nearest neighbors of the tetrahedral sites (Mittemeijer, 2010). In spite of the tetragonal symmetry of the distortion, the average lattice remains cubic due to the low amount of interstitials that can maximally be dissolved. Maximum solubilities are about 0.02 wt% C and 0.10 wt% N for ferrite and 2.1 wt% C and 2.4 wt% N in austenite (Mittemeijer, 2010). The larger solubility in austenite is in agreement with the larger available volume of the octahedral positions.

In a systematic study of the iron-nitrogen system by Jack (1948a, 1951a; b) it was shown that quenching from the austenite region forms nitrogen martensite, α', a tetragonally distorted body-centered structure, as is the case for the iron-carbon system. The b.c.c. configuration cannot incorporate the large amount of interstitial atoms. The tetragonal

distortion occurs since diffusion is limited by the cooling rate and precipitation of carbon or nitrogen-rich phases is hindered. Prolonged annealing of nitrogen martensite at 390 – 430 K leads to partial formation of an ordered martensite, α''-$Fe_{16}N_2$. Additional ordered phases are found in the iron-nitrogen system for increasing interstitial content, e.g. γ' and ε-nitrides cf. the phase diagram in Figure 2.1(*b*).

2.2.1 Nitrides: γ'-Fe_4N and ε-Fe_2N_{1-z}

The structure of γ'-Fe_4N consists of an f.c.c. arrangement of iron atoms with nitrogen in octahedral interstitial positions similar to austenite (Figure 2.3). Long range order, however, exists between nitrogen atoms, resulting in only one fourth of the octahedral sites being occupied (corner-sharing octahedra). This creates two inequivalent Fe sites; one with two nitrogen nearest neighbors and one uncoordinated, i.e. 12 iron nearest neighbors. Fe_4N is ferromagnetic with a Curie temperature, T_C, of approximately 767 K (Shirane *et al.*, 1962). In Mössbauer spectroscopy three inequivalent sites are observed (Nozik *et al.*, 1969; Blancá *et al.*, 2009) since the face-centered site (nitrogen nearest neighbors) generates two components or subspectra. These sites have tetragonal symmetry and the preferential direction of the magnetic moments makes the two axial and four equatorial sites inequivalent.

The structure of ε-Fe_2N_{1-z} is based on an h.c.p. iron lattice. In this arrangement octahedral sites sharing common faces are present, a feature not seen in f.c.c. lattices. The simultaneous occupation of two such sites induces strongly repulsive interactions and such a structural feature does not occur for any well-ordered interstitial compound (Parthé & Yvon, 1970). This limits the maximum nitrogen content to a composition of Fe_2N. At this composition, however, a rearrangement of N occurs under formation of the orthorhombically distorted ζ-Fe_2N (Jack, 1948a).

For ε-Fe_2N_{1-z} in the compositional range of $0.01 \leq z \leq 1/3$, Jack (1952) derived a structural model for nitrogen ordering. This was based on observed superstructure reflections in X-ray diffraction patterns requiring unit cell dimensions increased by $3^{1/2} \times 3^{1/2} \times 1$ with respect to the h.c.p. cell. The model is based on ideally ordered structures Fe_3N ($z = 1/3$) in space group $P6_322$ and Fe_2N ($z = 0$) in space group $P\bar{3}1m$ although only valid for $z \geq 0.01$, as noted. Microscopic thermodynamic models based on pair potentials between the interstitial atoms also predict these ordered low temperature phases (Hillert & Jarl, 1977; Kooi *et al.*, 1994). The intermediate range is described by *P312* symmetry. The superstructure cell contains six Fe atoms and six octahedral interstitial sites. The main difference between the space groups is the number of inequivalent octahedral sites, which is three for $P6_322$, four for $P\bar{3}1m$ and six for *P312* symmetry. Sites are labeled A1-C2 according to Table 2.1 (Leineweber & Jacobs, 2000) and the structures are shown in Figure 2.4. Starting from a composition of Fe_3N the sites A1 and B2 are filled. Increasing nitrogen content fills the C2 site.

Table 2.1: Site occupancies (ρ), Wyckoff sites (Wyc.) and coordinates (r) for octahedral sites in ε-Fe_2N_{1-z} according to the model of Jack (1952).

	ε-Fe_3N - $P6_322$			ε-Fe_2N_{1-z} - $P312$			ε-Fe_2N - $P\bar{3}1m$		
Site	ρ	Wyc.	r	ρ	Wyc.	r	ρ	Wyc.	r
A1	1	(2*c*)	(1/3 2/3 1/4)	1	(1*a*)	(0 0 0)	1	(1*a*)	(0 0 0)
A2	0	(2*d*)	(1/3 2/3 3/4)	0	(1*b*)	(0 0 1/2)	0	(1*b*)	(0 0 1/2)
B1	0	(2*d*)	(2/3 1/3 1/4)	0	(1*c*)	(1/3 2/3 0)	0	(2*c*)	(1/3 2/3 0)
B2	1	(2*c*)	(2/3 1/3 3/4)	1	(1*d*)	(1/3 2/3 1/2)	1	(2*d*)	(1/3 2/3 1/2)
C1	0	(2*b*)	(0 0 1/4)	0	(1*e*)	(2/3 1/3 0)	0	(2*c*)	(2/3 1/3 0)
C2	0	(2*b*)	(0 0 3/4)	1-3*z*	(1*f*)	(2/3 1/3 1/2)	1	(2*d*)	(2/3 1/3 1/2)

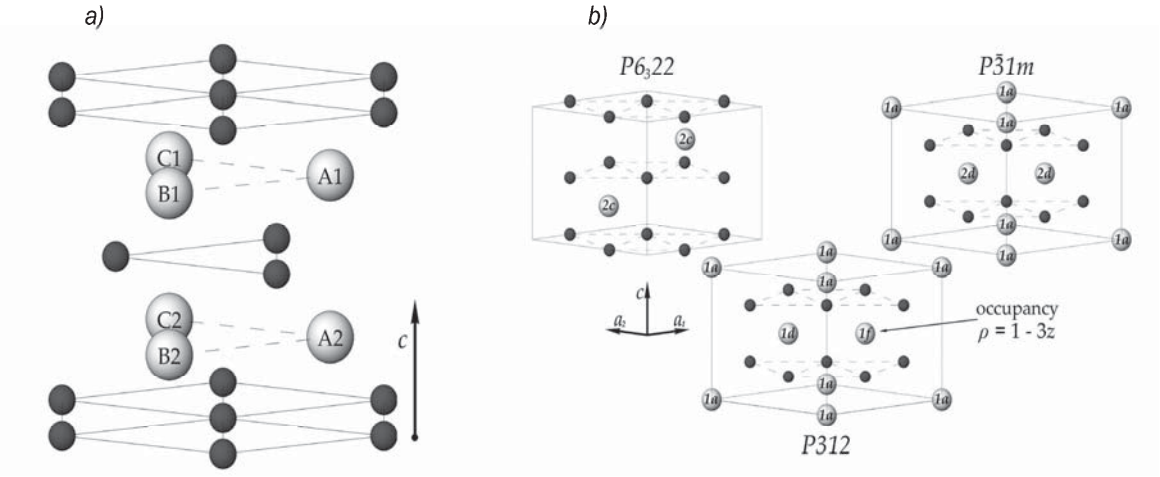

Figure 2.4: *a*) Octahedral interstitial positions in an h.c.p. structure of Fe atoms (dark spheres) and *b*) fully or partially occupied N sites in the structures of ε-Fe_3N, ε-Fe_2N_{1-z} and ε-Fe_2N. Note the different choice of origin for $P6_322$ symmetry as compared to $P\bar{3}1m$ and $P312$.

The different space groups, and thus the nitrogen ordering, can be distinguished in terms of superstructure reflections observed in diffraction experiments. For ε-type structures this information is contained in four different classes of reflections named after the first occurring representative reflection (Leineweber & Jacobs, 2000):

(110) class: $h - k = 3n$, l even
(001) class: $h - k = 3n$, l uneven
(100) class: $h - k \neq 3n$, l even
(101) class: $h - k \neq 3n$, l uneven

where n is an integer. The (110) class is always fundamental with respect to the ideal h.c.p. arrangement of the metal atoms. The overall structure factor is the sum of metal and interstitial contributions. The classes (100) and (101) are pure superstructure reflections, i.e. for an undistorted h.c.p. metal lattice there is only interstitial contribution. For the class (001) reflections there is no metal contribution for h, $k = 3n$, e.g. (001), (003), (301) and (331).

From Jack's *P312* model, superstructure reflections of the classes (101), (100) and (001) are expected. Leineweber *et al.* (2001) investigated ε-Fe_2N_{1-z} in the compositional range $0.07 \leq z \leq 0.27$ but only observed (001) reflections for $Fe_2N_{0.81}$. Other samples were modeled in $P6_322$ symmetry in which the (001) class is systematically extinct. Partial occupancy of the 2*b* site was found, and this deviates from the ideal model in that also site C1 will be partially occupied. The ε-nitrides become increasingly disordered at elevated temperatures. For a composition close to Fe_3N increasing, but reversible, disorder is observed above 470 K as nitrogen is partially transferred to the 2*b* Wyckoff site (Leineweber *et al.*, 1999). Additionally, it has been shown that the degree of disorder can be coupled to the axial ratio c/a (Leineweber, 2007). With increasing nitrogen content the ferromagnetic Curie temperature decreases from $T_C \simeq 575$ K for $z = 1/3$ to $T_C \simeq 10$ K for $z = 0.01$.

Iron sites in ε-Fe_2N_{1-z} can be differentiated with respect to the number of nearest neighbor nitrogen atoms using Mössbauer spectroscopy (Eickel & Pitsch, 1970). According to the ideal model each iron atom should be surrounded by two nitrogen atoms for $z = 1/3$. For increasing nitrogen content an increasing number of iron atoms are surrounded by three nitrogen atoms. Experimentally, two separate iron environments, each characterized by three nitrogen nearest neighbors, are observed (Chen *et al.*, 1983; Somers *et al.*, 1997), which may not readily be explained by the model.

Shang *et al.* (2006) proposed an explanation for the additional iron environment based on simultaneous occupation of the A1, B1 and C1 (or equivalently A2, B2 and C2) sites, i.e. the top (or bottom) plane of the trigonal prisms comprised of octahedral interstitial sites. This configuration also avoids octahedral sites sharing common faces, but is energetically unfavorable due to shorter distances between nitrogen atoms. The discrepancy between experimental and calculated values of hyperfine interactions (Shang *et al.*, 2006) and lack of additional experimental evidence for this type of ordering seems to disfavor this description. A simple explanation was offered by Chen *et al.* (1983) involving, for each iron atom with three nitrogen nearest neighbors, the surrounding iron atoms (second coordination shell). These may, themselves, be predominantly surrounded by either two or three nitrogen atoms, causing the two different observed iron environments.

In ε-iron nitrides, nitrogen may be partially replaced by carbon. The structure is similar to that of the pure nitrides (Jack, 1948b), but so far limited research has been performed on

the exact resulting structural modifications. The axial ratio *c/a* decreases with increasing carbon content (Naumann & Langenscheid, 1965b). In the investigation of a carbonitride with composition $Fe_2(N_{0.8}C_{0.20})_{0.92}$, class (001) reflections were observed without the presence of class (100) reflections (Leineweber *et al.*, 2001). Although allowed by symmetry, a situation where (100) reflections are not present is expected for ε-Fe_2N and a $P\bar{3}1m$ structural model was chosen. No extended conclusion regarding the interstitial ordering in the ε-carbonitrides can, however, be drawn from this single observation.

2.2.2 Carbides: θ-M_3C, χ-M_5C_2 and M_7C_3

Cementite (θ-Fe_3C) is one of the most commonly occurring constituents in the iron-carbon system. Together with Hägg carbide, χ-Fe_5C_2, and the Eckström-Adcock carbide, Fe_7C_3, cementite forms a group of iron carbides with trigonal prismatic coordination of carbon by iron atoms. The crystal structure of Fe_3C is described by an orthorhombic lattice in space group *Pnma*. It can be viewed as derived from a h.c.p. packing of iron atoms locally distorted to accommodate carbon (Fasiska & Jeffrey, 1965). The distortion of close-packed layers creates "pleated" sheets alternatively folded up and down as shown in Figure 2.5.

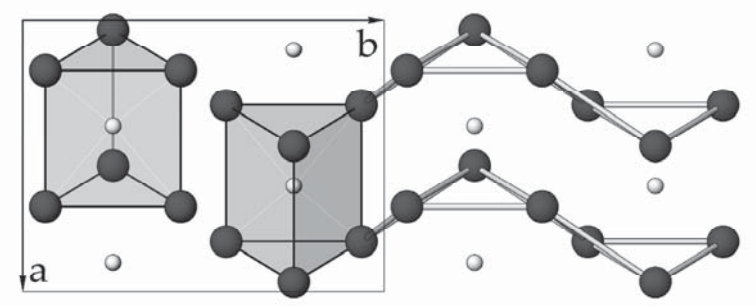

Figure 2.5: The trigonal prismatic coordination of carbon by six Fe atoms (left) and the pleated close-packed layers of Fe (right) in the structure of cementite. Dark spheres are Fe and light spheres C.

The iron-carbon arrangement in cementite is more closely packed than it would be if carbon occupied the octahedral holes of a close-packed metal-atom arrangement, with the volume per iron atom in Fe_3C being about 5% less than for austenite extrapolated to the same carbon content (Jack & Jack, 1973). Cementite is ferromagnetic at room temperature with a Curie temperature of approximately 480 K. Magnetic properties as well as thermal stability and unit cell dimensions are affected by the partial substitution of alloying elements found in commercial steels (Tsuzuki *et al.*, 1984), i.e. M_3C with M being the metallic composition.

Hägg carbide (χ-Fe_5C_2) is another common constituent of the iron-carbon system. The monoclinic structure (space group *C*2/*c*) of Hägg carbide closely resembles that of cementite with carbon located in trigonal prisms, but with prisms sharing additional edges, as seen in

Figure 2.6. A triclinic structure has been proposed (du Plessis *et al.*, 2007) but was shown to probably originate in misinterpretation of anisotropic microstrain broadening (Leineweber *et al.*, 2012). The Curie temperature of Hägg carbide is $T_C \simeq 520$ K (Hofer, 1966).

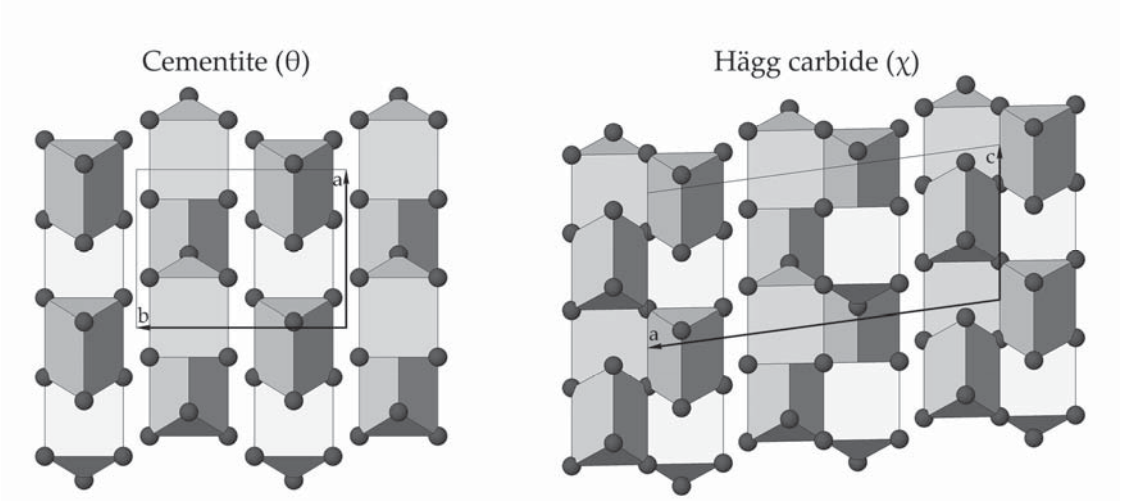

Figure 2.6: Arrangement of trigonal prisms of Fe atoms in the structures of cementite (left) and Hägg carbide (right).

It should be noted that, in iron nitrides nitrogen always occupies octahedral positions and is never surrounded by a trigonal prism of metal atoms. Nitrogen solubility in both θ and χ phases is negligible (Jack, 1948b) and the occurrence of different types of interstitial environments may be explained by the difference in electronegativity of the two non-metals (Jack & Jack, 1973).

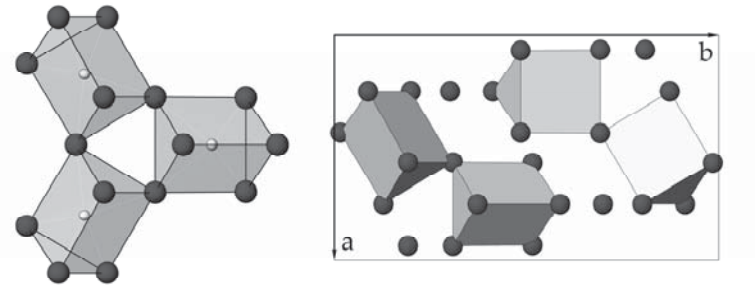

Figure 2.7: Arrangement of corner-sharing trigonal prisms in Fe_7C_3 (left) and the unit cell of the crystal structure (right). Dark spheres are Fe and light spheres C.

Fe_7C_3, or more generally M_7C_3 (M = Fe, Cr, W, etc.), is formed in various preparation and thermal treatment processes of alloys and steels (Fang *et al.*, 2009). The Curie temperature of Fe_7C_3 is $T_C \simeq 520$ K (Eckström & Adcock, 1950) similar to that of Hägg carbide and several structural models have been proposed; trigonal (Westgren, 1935), orthorhombic (Bouchaud & Fruchart, 1964) and hexagonal (Herbstein & Snyman, 1964). The proposed structures are

similar and may be considered as built up from the same structural elements consisting of three trigonal prisms (Figure 2.7). The correct crystal structure is orthorhombic and described in space group *Pnma* (Fruchart & Rouault, 1969), but crystals are heavily twinned and contain stacking faults. Ordered sequences of stacking faults essentially result in new crystal structures deviating from the orthorhombic symmetry (Kowalski, 1985).

2.2.3 Expanded austenite

Austenitic stainless steels are f.c.c. alloys of Fe, Cr and Ni (and may contain additional elements). The corrosion resistance of stainless steel is based on the presence of chromium in solid solution, which allows the development and maintenance of a passive chromium oxide layer at the surface. Nitriding, carburizing or nitrocarburizing is generally problematic for these steels as it will lead to the precipitation of chromium nitrides or carbides at high temperatures. Although a surface hardening effect can be achieved, the stainless character is lost as free chromium is no longer available to maintain the passive layer.

Formation of chromium nitrides and carbides can, however, be avoided with low temperature treatments. Nitriding of austenitic stainless steel below approximately 720 K introduces nitrogen into the surface-adjacent region and improves wear and fatigue performance (Christiansen & Somers, 2009; Dong, 2010). Corrosion resistance is retained and may even be improved by the process (Li & Bell, 2004; Fossati *et al.*, 2006) while the surface hardness can be increased by almost an order of magnitude (Christiansen & Somers, 2005). A solid solution of nitrogen forms in the nitrided zone containing 17–38 at.% N, corresponding to an occupancy of the interstitial f.c.c. sublattice of 0.16–0.61 (Christiansen & Somers, 2006a). As the developing case is essentially a supersaturated solid solution of nitrogen atoms in austenite, it is referred to as (nitrogen) expanded austenite, γ_N. Similarly, carbon expanded austenite is denoted γ_C.

Extended X-ray absorption fine structure (EXAFS) studies have shown that Fe, Cr and Ni exist in different local environments in nitrogen expanded austenite (Oddershede *et al.*, 2008b, 2010). Short range ordering of Cr and N occurs. The majority of Cr atoms have a first coordination shell with an average bond length shorter than, but in the vicinity of, the chemical compound CrN. The coordination number of Cr is maximally 5 (as compared to 6 for CrN), while no X-ray diffraction (XRD) indications of CrN development were found (Oddershede *et al.*, 2010). Martinavičius *et al*. (2012) found a coordination number of 5.7 and, using field ion microscopy, they observed precipitates preferentially at grain boundaries ascribed to CrN, which were not detectable with XRD. The authors suggested, for their samples produced by plasma-assisted nitriding, that the expanded austenite

structure consists of nanometric CrN precipitates embedded in a Fe_4N-like matrix. Whether these observations can be transferred to expanded austenite synthesized by other methods, e.g. gas nitriding, is still unclear. Although the (conversion electron) Mössbauer spectrum obtained by Martinavičius *et al.* for iron in expanded austenite is stated to be similar to that of Fe_4N, there are significant differences. Most notable is the necessity of including a hyperfine field distribution compared to the usually well-defined three Fe sites in Fe_4N (Blancá *et al.*, 2009).

For nanosized precipitates, partially coordinated surface atoms will effectively decrease the observed average coordination number. Additionally, surface atoms are not constrained to stay close to their nominal lattice positions, which may result in a contraction of surface atoms towards the core to minimize the surface energy (Huang *et al.*, 2008). This could explain the shorter Cr-N bond length in expanded austenite as compared to CrN. These observations may, however, also be the result of disorder in the system since, for EXAFS, this results in errors in bond lengths, coordination numbers, and disorder terms (Price *et al.*, 2012). In the analysis by Martinavičius *et al.*, the crystal structure was not constrained to the cubic symmetry of CrN, resulting in varying lengths of the scattering paths. Such constraints were implemented in the procedure by Oddershede *et al.*, yielding high disorder terms. Whether the apparent disorder is simply a size effect or the result of short range order between Cr and N while still constrained in the steel lattice is not clear. The results of Martinavičius *et al*. does not allow for a quantification of the precipitates. Although precipitation does seem evident, a large fraction of chromium atoms may very well exhibit a local environment similar to CrN while still being constrained in the lattice of the parent austenitic steel. In a recent study based on atom probe tomography, Martinavičius *et al.* (2015) concluded that nitrogen expanded austenite can be described as a mostly homogeneous nitrogen saturated phase with preferential MN (M = Cr, Fe) precipitation at defects such as stacking faults and/or twins; the majority of Cr is bonded to N either with short range order or in nanometer-sized precipitates, and some regions do not contain precipitates.

In assessing the crystallography of γ_N, the majority of published investigations have focused on samples of an expanded austenite zone grown into an austenite substrate rather than on homogeneous samples, see e.g. Fewell & Priest (2008). The resulting depth variation of the composition has several implications for the observed X-ray diffractograms. The compositional inhomogeneity within the investigated depth range causes asymmetric broadening, and the induced macrostress gradient over the expanded austenite zone causes *hkl*-dependent shifts of the diffraction peaks (Öztürk & Williamson, 1995; Xu *et al.*, 2000; Christiansen *et al.*, 2010). Asymmetric broadening is also anticipated from texture gradients (Rivière *et al.*, 2007).

Even for homogeneous samples, where the influences of composition-induced stresses and asymmetric broadening are avoided, diffraction peaks are still broadened and shifted from their ideal positions. It has been reported that peak-width anisotropies observed in diffraction profiles can be caused by screw dislocations in the structure, and that the dislocation density increases with interstitial nitrogen occupancy (Oddershede *et al.*, 2008a).

Currently, the best structural description for homogeneous samples (Christiansen & Somers, 2004) is an f.c.c. lattice with stacking faults contributing to systematic deviations of XRD peaks as described by Warren (1969). Faulting of the f.c.c. lattice causes both an *hkl*-dependent shift of diffraction peaks and asymmetric broadening. It should be noted that Warren's theory has been demonstrated to be insufficiently accurate (Velterop *et al.*, 2000), but the deviations are relatively small for the strongest f.c.c. reflections 111, 200 and 220, particularly for modest stacking fault probabilities. The structural description does, however, not explain all features of diffractograms of expanded austenite. This subject is explored in more detail in Chapter 7.

Chapter 3

Experimental methods

A wide array of experimental techniques exists for determining the properties of solids. The purpose of this chapter is to introduce the basic principles of the primary utilized experimental methods in this work: X-ray and neutron diffraction in combination with the so-called Rietveld method, as well as Mössbauer spectroscopy and vibrating sample magnetometry. Since these are all well-established techniques, additional information beyond this introduction may be found in various available handbooks on the subjects, e.g. by Gütlich *et al.* (2011) and Young (1993).

3.1 X-ray and neutron diffraction

X-ray diffraction is a valuable tool in identification and characterization of crystalline materials. Due to the periodic structure of crystals, these function as three-dimensional diffraction gratings for electromagnetic radiation in a suitable range of wavelengths. Wavelengths of 0.5 to 2.5 Å are of particular interest since these correspond to typical repeat distances and chemical bond distances in crystals. The conditions for observable diffracted intensity (constructive interference) is given by Bragg's law (Bragg, 1913):

$$n\lambda = 2d_{hkl}\sin\theta \tag{3.1}$$

where n is an integer, λ the wavelength of the radiation, d_{hkl} is the distance between parallel crystal lattice planes with Miller indices hkl, and θ is the angle between the incident radiation and the planes.

Diffracted intensity is thus only observed at specific angles and rotations of the crystal. For polycrystalline materials or powders there will always be many crystals in the right position for diffraction from any of the lattice planes. Diffraction data from polycrystalline samples are given as diffractograms showing intensity versus diffraction angle, 2θ. At angles where the Bragg condition is fulfilled, peaks or so-called Bragg reflections are observed. Peak positions depend on the distance between lattice planes and the symmetry of the crystal while the types of atoms present on the crystal lattice affect the observed intensity of the peaks. In addition to information on the atomic structure, diffractograms of polycrystalline specimens also contain information on other properties like particle sizes, residual stresses and texture, as well as quantitative information on the different phases in mixed samples. Diffractograms may also be presented as intensity versus the magnitude of the scattering vector, $q = 4\pi\sin\theta/\lambda$, which makes it easier to compare data obtained with different wavelengths.

In X-ray diffraction experiments, the radiation is scattered by the electron cloud surrounding each atom, and the scattering factor for X-rays increases linearly with the number of electrons in the atom. Therefore, heavy atoms are much more effective at scattering than light atoms, but due to the size of the electron distribution scattering from different parts of the cloud is not always in phase. The resulting destructive interference causes X-ray scattering factors to decrease with $\sin\theta/\lambda$.

Neutrons, on the other hand, interact directly with the nuclei of atoms, making neutron diffraction an excellent complimentary technique. Because of the small size of the nucleus, neutron scattering factors do not decrease with scattering angle and are similar in value for most atoms. The contribution to the diffracted intensity is different for each isotope, and light atoms may contribute strongly even in the presence of heavy atoms. The basic principles of diffraction (e.g. Bragg's law) are the same, although neutrons interact with matter differently than X-rays. Neutrons are neutral particles but possess a non-zero magnetic moment, which makes it possible to study magnetic as well as atomic structures.

Diffractograms from polycrystalline samples are basically one-dimensional projections of the three-dimensional reciprocal lattice[1] of a crystal. In all but the simplest structures, peak profiles of the reflections are not all resolved but partially overlap, increasingly so at higher diffraction angle. The overlap problem may be overcome by fitting a calculated diffraction profile based on simultaneously refined models for the crystal structure(s) to the

[1] The reciprocal lattice is a mathematical construction related to the three-dimensional (real) crystal lattice and is an essential tool in visualization and understanding diffraction phenomena.

entire observed diffraction pattern, the so-called Rietveld method. During refinement an improved description of the structure is obtained, which in turn improves the allocation of observed intensity to partially overlapping individual Bragg reflections. This inherent feedback mechanism is absent in the alternative, pattern decomposition methods, where initially all observed intensity is assigned to individual Bragg reflections. The derived Bragg intensities are subsequently used for structure refinement as a separate procedure.

3.1.1 The Rietveld method

The Rietveld method (Rietveld, 1967, 1969), also referred to as Rietveld analysis or Rietveld refinement, is an analytical tool for fitting a structural model to a diffractogram based on simultaneous refinement of structural parameters and background. The method is a least-squares procedure minimizing the residual, S_y:

$$S_y = \sum_i w_i (y_i - y_{ci})^2 \tag{3.2}$$

where y_i is the observed intensity at the ith step, y_{ci} is the calculated intensity at the ith step and w_i is the statistical weight; typically $w_i = 1/y_i$. A diffractogram of a polycrystalline material may be considered as a collection of individual reflection profiles, each characterized by a peak height, a peak position, a breadth and tails that decay gradually with distance from the peak position. The integrated area of the reflection profile is proportional to the absolute value of the structure factor, $|F_H|^2$, which is calculated from the structural model. The calculated intensities, y_{ci}, are determined by summing the calculated contributions from Bragg reflections for each phase N plus the background:

$$y_{ci} = \sum_N s_N \sum_H L_H \left|F_H\right|^2 \phi(2\theta_i - 2\theta_H) P_H A + y_{bi} \tag{3.3}$$

where H represents the Miller indices; h, k, l, of a Bragg reflection, L_K contains the Lorentz, polarization and multiplicity factors, ϕ is the reflection profile function corrected for angular offset, $2\theta_K$. P_K and A represent corrections for preferred orientation (texture) and absorption, respectively, and y_{bi} is the background intensity at the ith step. In multiphase samples the scale factor, s_N, may be used for quantitative phase analysis. The Rietveld method is not a structure solution method but offers a way to refine crystal structures. The least-squares procedure thus requires a reasonably good starting model.

Commonly reported residuals are the plain pattern residual, R_p, which is simply the normalized residual of the refinement and the weighted pattern residual, R_{wp}:

$$R_p = \frac{\sum |y_i - y_{ci}|}{\sum y_i} \tag{3.4}$$

$$R_{wp} = \left[\frac{\sum w_i (y_i - y_{ci})^2}{\sum w_i (y_i)^2} \right]^{\frac{1}{2}} \tag{3.5}$$

The latter is the normalized residual of the quantity being minimized in the least-squares procedure, S_y (equation 3.2). Note that, if a (correctly fitted) high background is present, misleadingly low *R*-values may be obtained since the denominator sums over observed intensities. Another useful numerical criterion, also related to the least-squares sum, is the *goodness-of-fit*, χ^2:

$$\chi^2 = \frac{\sum w_i (y_i - y_{ci})^2}{(n - p)} \tag{3.6}$$

where n is the number of observations and p the number of refined parameters. Values approaching unity are expected for satisfactory fits. A caveat to this is that χ^2 scales with observed intensity such that it is actually increased for high quality data. If only random errors arising from counting statistics are present (in most cases unlikely to be achieved), a value below unity indicates a model that contains more parameters than can be justified by the data quality. Residual values alone do not suffice in order to identify potential problems in the refinement. For this purpose a difference plot between calculated and observed intensities is essential.

3.2 Mössbauer spectroscopy

Recoil-free resonant absorption and emission of γ-rays, the so-called Mössbauer effect discovered in 1958 (Mössbauer, 1958, 1959), can be used to obtain precise information about the chemical, structural, magnetic and time-dependent properties of a material. Mössbauer spectroscopy requires a suitable γ-ray source to observe resonant absorption in a sample. A free nucleus recoils during emission or absorption of a γ-ray due to conservation of momentum. Nuclei in low-lying excited states, with a relatively slow decay rate, embedded in a crystal lattice may, however, transmit the recoil momentum from absorption or emission to the entire crystal, resulting in no loss of recoil energy. A well-defined frequency is thus obtained, allowing measurements of the small perturbations of the nucleus caused

by the atomic surroundings. Mössbauer spectroscopy can be performed using approximately 80 different isotopes with ^{57}Fe being the most commonly used.

A source containing ^{57}Co diffused into a metallic foil provides excited ^{57}Fe nuclei that decay to the ground state via a γ-ray cascade. This includes a 14.4 keV γ-ray that can excite a transition in the sample being studied if the energy matches the energy gap in the sample; i.e. it is absorbed resonantly. The emission line is Doppler shifted by moving the source with a given velocity, v, slightly adjusting the frequency of the γ-ray. By scanning the relevant velocity range, it is possible to probe splittings in the energy levels of the absorber nucleus, which might result from magnetic or other interactions. Mössbauer spectra thus contain the transmission of γ-quanta as a function of the Doppler velocity of the source. The extremely fine energy resolution of Mössbauer spectroscopy allows observation of subtle changes in the nuclear environment of the relevant atoms. The energy levels can be modified by their environment in three main ways; by the isomer shift, quadrupole splitting and magnetic splitting (Figure 3.1).

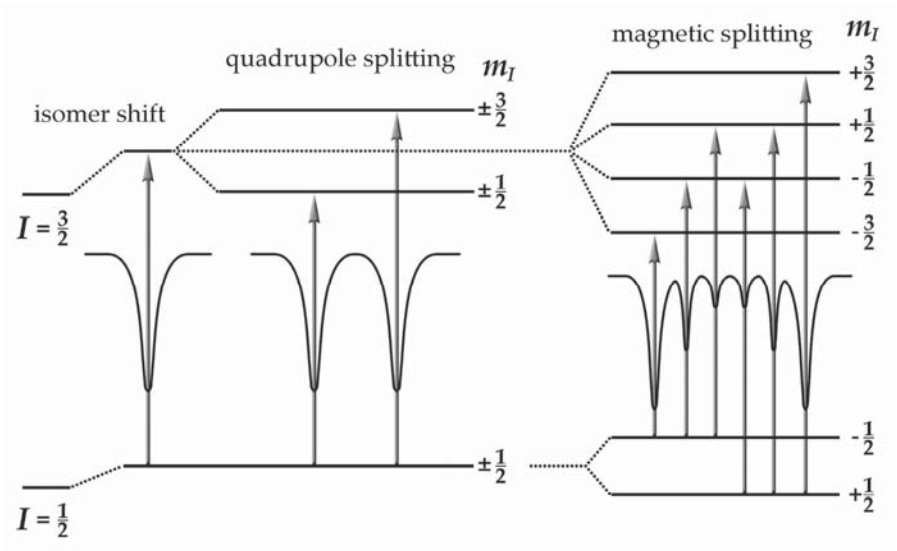

Figure 3.1: The effects of isomer shift, quadrupole splitting and magnetic splitting on the nuclear energy levels of ^{57}Fe. Arrows show the absorption transitions and the corresponding spectra are illustrated.

The isomer shift arises due to the finite size of the nucleus and the electronic charge distributions over the nuclear volume. Slight changes in Coulomb interactions due to differences in the *s*-electron environment between the source and absorber produce a shift in the resonance energy of the transition. This sets the centroid of the spectrum. Shifts are quoted relative to a known absorber, for example α-Fe at room temperature for ^{57}Fe Mössbauer spectra.

Nuclei in states with an angular momentum quantum number $I > {}^1/_2$ can have a non-spherical charge distribution that produces a nuclear quadrupole moment. In certain crystal environments the nucleus may be subjected to an electric field gradient. The interaction between the nuclear quadrupole moment and the electric field gradient splits the nuclear energy levels. For ^{57}Fe, the excited state ($I = {}^3/_2$) is split into a doublet, producing two lines in the Mössbauer spectrum.

Magnetic splitting is caused by the interaction between the nucleus and the local magnetic field. The nuclear spin moment experiences an interaction with the magnetic field that can split the $I = {}^1/_2$ ground state of ^{57}Fe into a doublet and the excited $I = {}^3/_2$ into a quadruplet corresponding to six possible lines (a sextet) in the Mössbauer spectrum. This effect makes it possible to measure local magnetic fields that depend on the chemical state of the probed atom. If hyperfine interactions are present an additional, usually smaller, quadrupole interaction will cause a shift in the energy levels and is commonly referred to as quadrupole shift.

3.3 Vibrating sample magnetometry

A vibrating sample magnetometer (VSM) is used to measure the magnetic properties of materials. The sample is placed in a uniform magnetic field, created between the poles of an electromagnet, which induces a dipole moment by aligning the magnetic domains, or the individual magnetic spins in the material under investigation. The sample is vibrated with sinusoidal motion perpendicular to the magnetizing field. The resulting alternating magnetic field will induce a sinusoidal electrical signal in suitably placed stationary pick-up coils. The signal is proportional to the magnetic moment of the sample, as well as to the amplitude and frequency of the vibration.

Measurements of the magnetic moment versus temperature in a given external magnetic field may be used for the determination of Curie temperatures. The Curie temperature (T_C) of a ferromagnetic material is the temperature where its uncompensated spins in zero field undergo a second order phase transition from a thermally disordered (paramagnetic) state to a magnetically ordered low temperature state (Fabian *et al.*, 2013).

The magnetic transition is usually not well-defined experimentally as a single point but covers a small temperature range. Since there is no clear general agreement about the accurate position of T_C within this temperature range, the following definition of Fabian *et al.* (2013) is used in the present work: The Curie point in external fields corresponds to the inflection point of the magnetization curve versus temperature, i.e. the second derivative is zero.

Chapter 4

Synthesis and characterization: Phases in the iron-carbon-nitrogen system

Synthesis of pure and homogeneous specimens of iron nitrides and carbides is practically limited by diffusion distances of nitrogen and carbon and by the metastability of the compounds with respect to decomposition into iron, graphite and nitrogen gas. An imposed equilibrium can be established at the very surface of a specimen in contact with a nitriding or carburizing medium, while elevated temperatures will promote decomposition below the surface. A thin starting material is thus required for the preparation of homogeneous samples. The ratio of surface area to bulk material of a thin iron foil may be further improved by exploiting the metastability of iron nitrides.

Figure 4.1 shows the thermogravimetric curve for such a pretreatment of 25 μm iron foil at 873 K. The initial treatment in gaseous ammonia, NH_3, causes nitrogen to be absorbed and diffuse through the foil. Away from the surface, nitrogen gas, N_2, is developed, which causes pore formation throughout the material. The final step, so-called denitriding in a hydrogen atmosphere, completely removes the remaining nitrogen, leaving behind a porous iron foil. The resulting increased surface area increases the reaction rate of subsequent nitrocarburizing, and since the required diffusion distances are reduced, homogeneous samples can be obtained.

The pretreatment was applied to six samples of iron foils, which were subsequently nitrocarburized in gas mixtures of ammonia, hydrogen and propene adjusted to different nitriding and carburizing potentials, resulting in formation of various iron carbides and nitrides. Samples are denoted S1 – S6 and represent a compositional series of progressive increase in nitrogen content and decrease in carbon content. Thermal expansion and phase transformations were studied with *in situ* synchrotron X-ray diffraction.

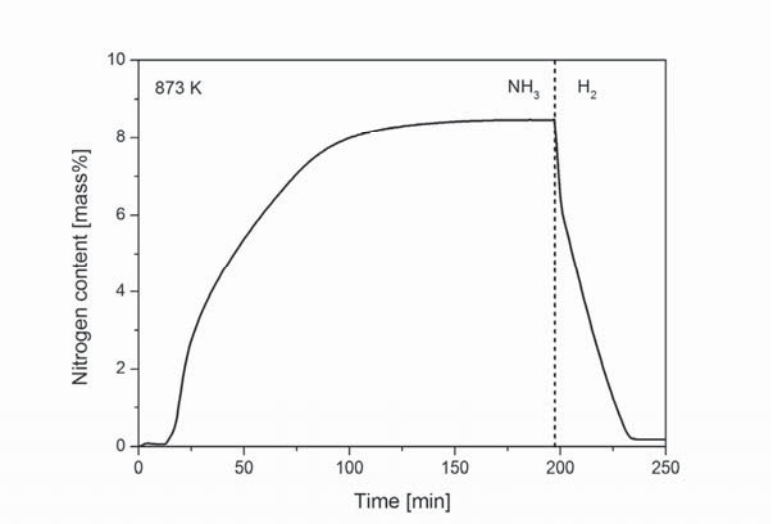

Figure 4.1: Thermogravimetric curve for gaseous pretreatment of 25 μm iron foil at 873 K in two steps; nitriding in ammonia (infinite nitriding potential) and denitriding in hydrogen (zero nitriding potential). The apparent difference in initial and final mass is the result of buoyancy effects due to changing temperature and gas composition.

4.1 Experimental

Unalloyed (Armco) iron foil pieces of 25 μm thickness were used for nitrocarburizing with ammonia, nitrogen and hydrogen gasses of 99.999% and propene of 99.5% purity. Both pretreatment to form porous iron foils and nitrocarburizing were performed in ceramic crucibles in a Netzsch STA 449 C Jupiter thermal analyzer. Nitrocarburizing at 718 K was continued until a stationary weight was obtained. Total gas flow rates of 58 – 108 mL/min were used including a constant N_2 flow of 5 mL/min for protection of electronics in the measurement compartment. Nitriding (K_N) and carburizing (K_C) potentials according to equations 2.8 and 2.9, treatment time and resulting phase composition for the six samples are given in Table 4.1. After cooling the porous samples were gently ground to powder in a mortar.

Resulting carbon and nitrogen content for all samples was determined by combustion infrared detection (carbon content) on a LECO CS230 and by inert gas fusion thermal conductivity detection (nitrogen content) on a LECO TN500. Since both S4 and S6 contain ζ

as a minority phase (see Figure 4.2), the composition of ε in these samples was determined assuming stoichiometric composition, $Fe_2(N,C)_1$, for ζ with a ratio between nitrogen and carbon atoms equal to that of the total sample composition.

Table 4.1: Nitriding (K_N) and carburizing (K_C) potentials according to equations 2.8 and 2.9, required time to reach a stationary weight, carbon and nitrogen content and resulting phase composition.

Sample	S1	S2	S3	S4	S5	S6
K_N [atm$^{-1/2}$]	0.2285	1.468	4.928	17.91	136.6	∞
K_C [atm$^{-2/3}$]	0.2096	0.6306	1.268	2.835	10.64	∞
Time [hours]	100	94	62	29	8.3	7.7
C [mass%]	6.44	6.22	6.12	3.88	0.96	0.48
N [mass%]	0.09	1.22	2.26	5.97	9.25	10.3
Composition	θ, χ, α	χ, θ, γ′, ε	χ, ε	ε, ζ	ε	ε, ζ

X-ray diffractograms were collected at a wavelength of either λ = 1.001952(5) Å or λ = 0.994426(3) Å in transmission mode with a Huber G670 Guinier camera at MAX-lab beamline I711 (Cerenius *et al.*, 2000). In order to reduce the influence of fluorescence, aluminium foils were positioned between the sample and the detector. Samples were either mounted on tape at room temperature or in 0.7 mm inner diameter quartz capillaries filled with an inert argon atmosphere to avoid oxidation and heated in a Huber 670.3 furnace. Temperature calibration and determination of the applied wavelength, as well as correction for diffraction angle (2θ) zero shift, were performed using a Si standard. For both S1 and S2, 31 diffractograms were measured in the temperature range 413 – 1055 K and for S3 – S6, 22 diffractograms in the range 450 – 1000 K. Data were collected in a 2θ range of 4 – 100° (corresponding to a q range from 0.4 to 9.7 Å^{-1}) with a fixed step size of 0.005° in 2θ and an exposure time of 240 seconds at each temperature step. After exposure, the temperature was immediately ramped to the next set point (average heating rate of 3 K/min). Rietveld refinements of intensity versus scattering angle (2θ) were carried out using the program *WINPOW*, a local variation of *LHMP* (Howard & Hill, 1986) in order to fit lattice parameters and mass fractions of the constituent phases. Pseudo-Voigt profile functions were applied together with Chebyshev background polynomials.

4.2 Results and discussion

Diffractograms for all six samples are shown in Figure 4.2. In all cases, except for one (S5), the samples consisted of more than a single phase. Remaining ferrite (α) due to incomplete formation of nitrides or carbides was only observed for S1, which was subjected to the lowest nitriding and carburizing potentials and required the longest treatment time to reach a stationary carbon/nitrogen uptake (Table 4.1). In addition to ferrite, the sample contains

small amounts of Hägg carbide (χ) and the main constituent, cementite (θ). For increasing potentials (S2), formation of Hägg carbide is favored with cementite, γ′-Fe_4N and ε-carbonitride as minor phases. S3 contains only Hägg carbide and ε-carbonitride. Further increase of the nitriding and carburizing potentials (S3 – S6) leads to formation of ε and ζ phases and drastically reduces the required treatment time.

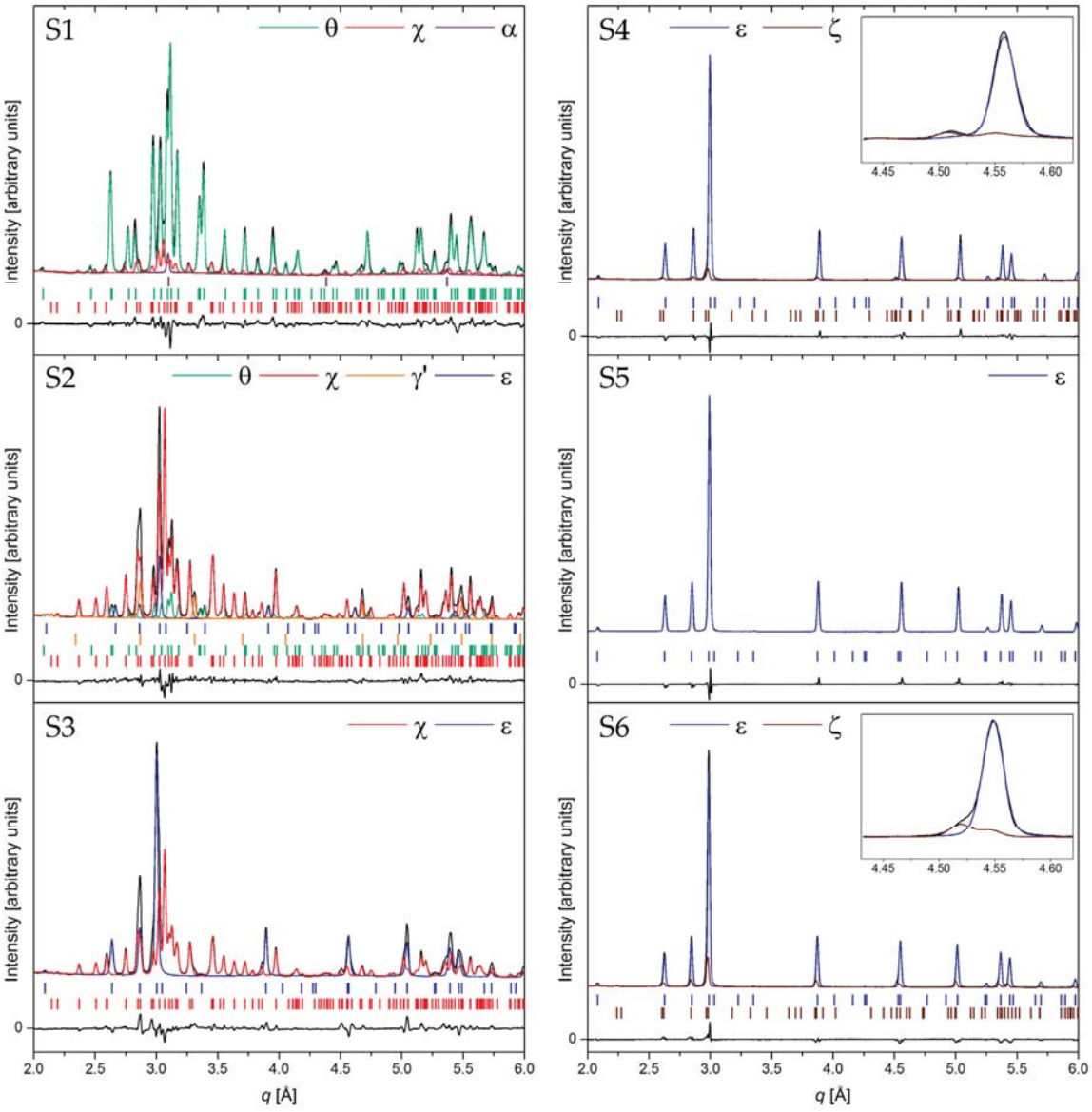

Figure 4.2: X-ray diffractograms, refined Rietveld profiles and difference curves up to q = 6.0 Å^{-1} for nitrocarburized porous iron foil. Insets show peaks of two distinct phases, ε and ζ. Profile residuals (R_p) and goodness-of-fit values (χ^2) are ≤ 2.52% and 2.51, respectively.

Comparing the phase compositions obtained at 718 K to the isothermal section at 773 K of the ternary Fe-C-N phase diagram (Naumann & Langenscheid, 1965b)[1], it is apparent that samples S1 and S2 each contain an additional phase compared to the expected compositions. The additional occurrence of Hägg carbide in S1 and γ'-(carbo)nitride in S2 suggests that a homogeneous distribution of nitrogen and carbon was not obtained, i.e. compositional variations exists in these samples. The expected phase composition is obtained for samples S3 and S5 whereas samples S4 and S6 contain ζ-Fe_2(N,C), which does not appear in the isothermal section at 773 K due to the limited thermal stability of this phase. Due to the relatively low X-ray scattering power of nitrogen and carbon, no superstructure reflections yielding direct information on the possible space groups for the ε-phases were observed. Consequently, Rietveld refinements were carried out in space group $P\bar{3}1m$ as reported for ε-$Fe_2(N_{0.8}C_{0.20})_{0.92}$ (Leineweber *et al.*, 2001).

In the synthesis of iron carbides and nitrides, a combination of low carburizing and nitriding potentials requires relatively long treatment times and primarily leads to formation of iron carbides. Formation of (carbo)nitrides is favored for increasing potentials, which also increase the reaction rate and thus reduce required treatment time.

4.2.1 *In situ* X-ray diffraction

Phase transformation maps as a function of temperature are given in Figure 4.3. The composition of sample S1 is constant up to approximately 850 K where initial decomposition of Hägg carbide (χ) to cementite (θ) is observed. Above 950 K, ferrite (α) is formed and austenite (γ) above 1025 K. Note that, from a mass balance perspective, carbon is missing as less C-rich phases are formed. This is likely due to formation of graphite, which was not detectable due to the high background from the diffuse scattering of the capillary. Similar considerations apply to all samples. For decomposition of nitrides, nitrogen is released as gaseous N_2.

For S2, the initial primary constituent, Hägg carbide, is transformed to cementite above 850 K, similarly to S1. Thermal decomposition of γ' and ε-phases occur above 900 K followed by formation of ferrite and austenite. Both Hägg carbide and ε-carbonitride decompose to cementite above 850 K, followed by formation of ferrite for S3. Austenite is not formed due to the lower final temperature (1000 K) compared to S1 and S2 where austenite was observed only above 1025 K. Similarly, samples S4 – S6 are composed either entirely of ferrite or in combination with cementite at the final temperature of 1000 K.

For S4 – S6, thermal decomposition of the ζ-phase, if present, is observed from 680 to 770 K while transformation of the ε-carbonitrides occurs between 795 and 900 K. Because of the low carbon content of S5 and S6 (Table 4.1) no cementite is formed. The nitrogen

[1] No isothermal section at 718 K is currently available.

content is gradually reduced as N_2 is released, causing formation of γ′-Fe_4N, followed by ferrite. For S4 and S6, austenite is briefly formed around 900 K in agreement with the iron-nitrogen phase diagram (Figure 2.1*b*), which shows that austenite is stabilized by the presence of nitrogen above 865 K. For the carbon-rich samples (S1 and S2), austenite is only observed above 1025 K, in accordance with the iron-carbon phase diagram in Figure 2.1(*a*). Note that Hägg carbide does not appear in this phase diagram but is actually thermodynamically favored over cementite below about 620 K (Schneider & Inden, 2001).

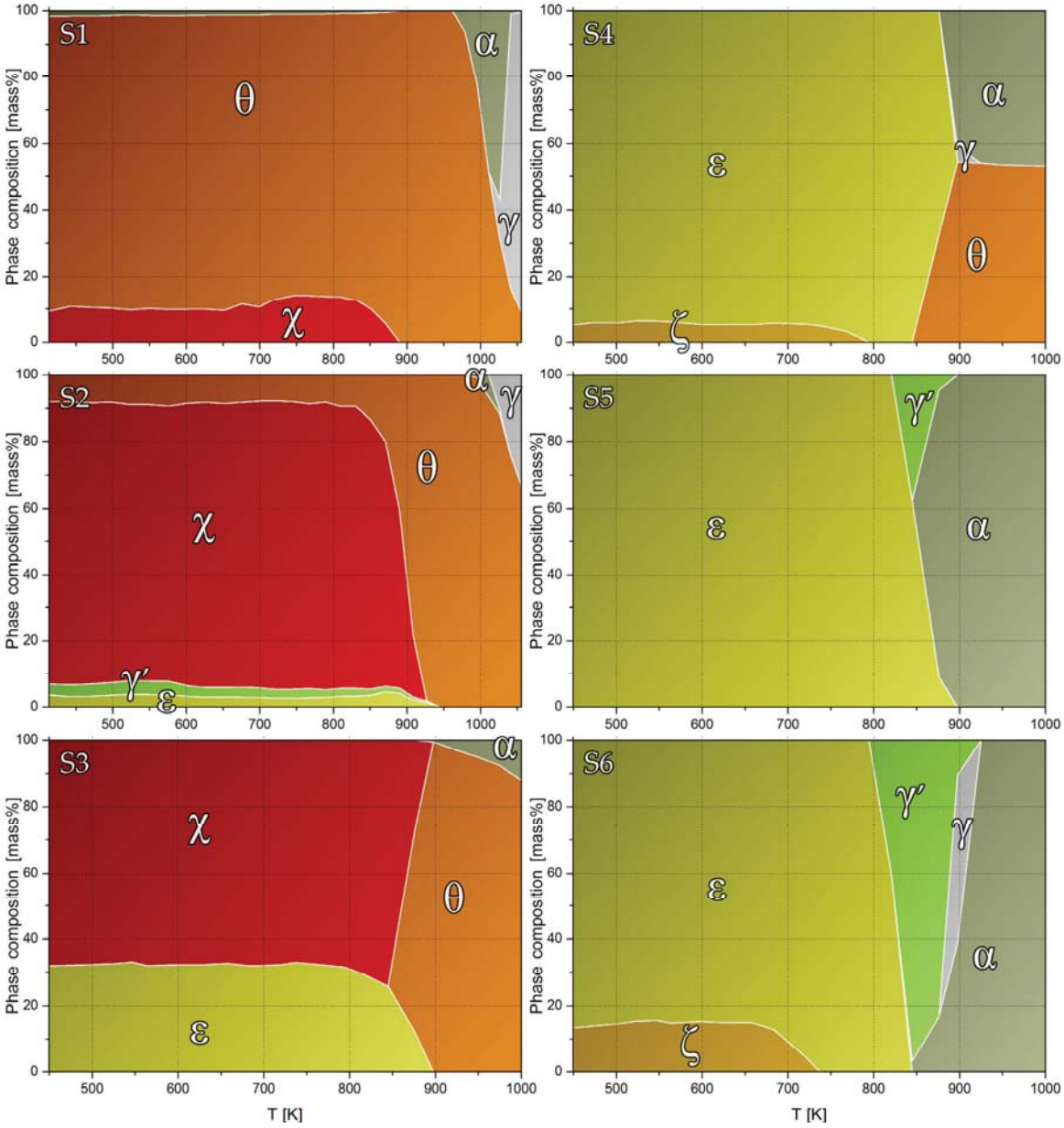

Figure 4.3: Phase transformation maps for samples S1-S6. Note the higher temperature range for S1 and S2. Estimated standard deviations from refinements are ≤ 1.1 mass%.

4.2.2 Thermal expansion

The commonly used mean (linear) coefficient of thermal expansion, α_{exp}, was fitted to the expression:

$$a(T) = a_{Tr}[1 + \alpha_{exp}(T\text{-}T_r)] \tag{4.1}$$

where a is the lattice parameter of the unit cell and a_{Tr} is the lattice parameter at a chosen reference temperature, T_r. The volumetric coefficient of thermal expansion was found by replacing the lattice parameter with the volume of the unit cell, V, in the above expression. A better description of the unit cell volume of cementite and Hägg carbide was obtained using a temperature-dependent expression (Fei, 1995):

$$V(T) = V_{Tr} \exp\left[\int_{T_r}^{T} \alpha_{exp}(T)dT\right] \tag{4.2}$$

with the expansion coefficient expressed as $\alpha_{exp}(T) = a_0 + a_1T$. Refined unit cell volumes and fitted expressions for thermal expansion for cementite and Hägg carbide are presented in Figure 4.4.

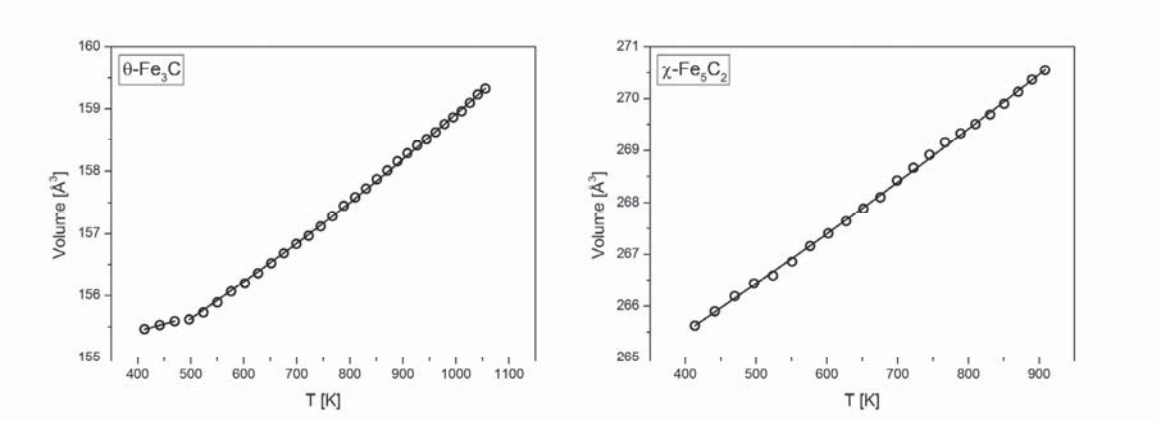

Figure 4.4: Unit cell volume versus temperature for cementite (left) and Hägg carbide (right). Estimated standard deviations are ≤ 0.1 Å^3. Lines correspond to fitted expressions for thermal expansion (equations 4.1 and 4.2).

For cementite up to 470 K, a volumetric expansion coefficient of α_{exp} = 1.5 × 10^{-5} K^{-1} is obtained from equation 4.1. Above this temperature, the expansion coefficient changes due to the transition from a ferromagnetic to a paramagnetic state. From equation 4.2 the following values were obtained in the temperature range 497 – 1055 K; a_0 = 2.7 (1) × 10^{-5} K^{-1} and a_1 = 2.0 (2) × 10^{-8} K^{-2}. This yields an average of α_{exp} = 4.3 (2) × 10^{-5} K^{-1} in excellent agreement with the value α_{exp} = 4.1 (1) × 10^{-5} K^{-1} obtained by Wood *et al*. (2004). The

expansion coefficient is slightly lower than that of b.c.c. iron, α_{exp} = 4.4 × 10^{-5} K^{-1} for a similar temperature range (Basinski *et al.*, 1955).

No published data for the thermal expansion of Hägg carbide is available. From equation 4.2 the values a_0 = 3.1 (1) × 10^{-5} K^{-1} and a_1 = 9.9 (2) × 10^{-9} K^{-2} are obtained. In the temperature range 413 – 908 K, this corresponds to an average volumetric expansion coefficient of α_{exp} = 3.8 (2) × 10^{-5} K^{-1}, which is slightly lower than for cementite. No magnetic transition affecting the unit cell volume was observed for Hägg carbide.

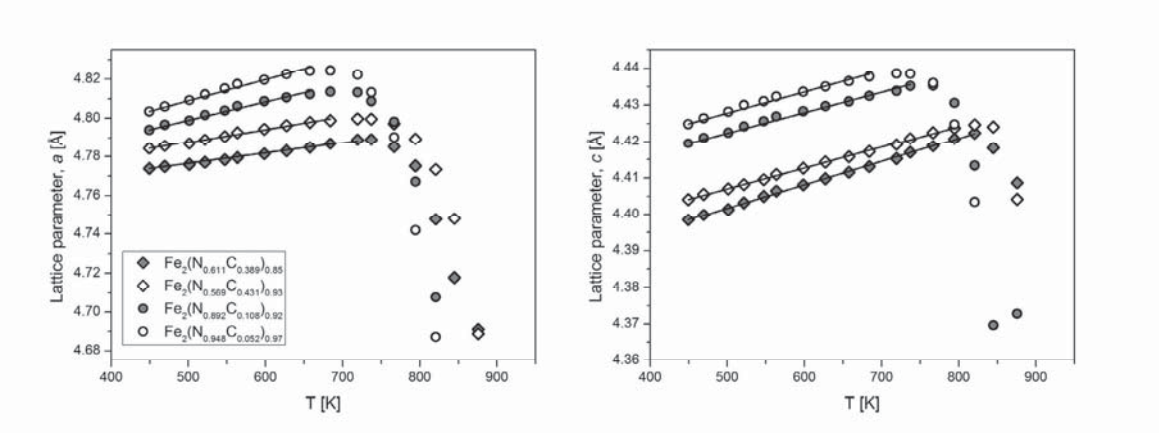

Figure 4.5: Lattice parameters *a* (left) and *c* (right) versus temperature for ε-$Fe_2(N,C)_{1-z}$. Estimated standard deviations are ≤ 10^{-3} Å. Lines correspond to fitted expressions for thermal expansion (equation 4.1).

Lattice parameters versus temperature for ε-carbonitride phases are presented in Figure 4.5. Thermal expansion is approximately linear and can be fitted to equation 4.1 until lattice parameters decrease due to removal of nitrogen and carbon from the structure. For the samples with initial high interstitial content, the driving force for N_2 and graphite formation is largest. The decrease in lattice parameter therefore occurs at a lower temperature compared to samples with lower interstitial content. Lattice parameters at room temperature, composition and thermal expansion coefficients are given in Table 4.2.

Table 4.2: Lattice parameters (*a* and *c*) at room temperature and expansion coefficients fitted to equation (4.1) in terms of the lattice parameters and unit cell volume (*V*) for ε-iron carbonitrides.

Sample	S3 $Fe_2(N_{0.611}C_{0.389})_{0.85}$	S4 $Fe_2(N_{0.569}C_{0.431})_{0.92}$	S5 $Fe_2(N_{0.892}C_{0.108})_{0.92}$	S6 $Fe_2(N_{0.948}C_{0.052})_{0.96}$
a(RT) [Å]	4.7655(2)	4.77513(4)	4.77729(5)	4.78556(5)
c(RT) [Å]	4.3865(2)	4.38934(4)	4.40799(3)	4.41398(3)
$\alpha_{exp}(a)$ [×10^{-5} K^{-1}]	1.11 (2)	1.37 (3)	1.97 (5)	2.25 (6)
$\alpha_{exp}(c)$ [×10^{-5} K^{-1}]	1.46 (1)	1.30 (1)	1.26 (2)	1.31 (3)
$\alpha_{exp}(V)$ [×10^{-5} K^{-1}]	3.67 (4)	4.04 (6)	5.28(13)	5.85(15)

Increasing total interstitial content increases both *a* and *c* parameters of the ε-carbonitrides at ambient temperatures, but values deviate from the published relation for pure nitrides (Somers *et al.*, 1997). Both volumetric thermal expansion and expansion coefficient in the *a*-direction, parallel to (001), is also increased. Thermal expansion decreases in the *c*-direction, perpendicular to (001), except for S6 containing $Fe_2(N_{0.948}C_{0.052})_{0.96}$, which deviates from this trend. The anisotropic lattice expansion for increasing interstitial contents, and at elevated temperatures for fixed contents, may be explained from edge-sharing contacts of octahedral positions in the hexagonal iron lattice (Jack, 1952; Leineweber *et al.*, 2004). Simultaneous occupation of such positions causes repulsive interactions. The edge-sharing contacts occur exclusively parallel to (001) and can be accommodated by preferential expansion of the structure in that direction.

The observed deviation in the trend of thermal expansion in the *c*-direction may be due to different carbon contents of the samples and magnetic properties may also affect the structure. The effects of partial substitution of nitrogen by carbon in ε-iron nitride on interstitial ordering and magnetic properties, as well as the deviation from published relations between nitrogen content and lattice parameters, is explored in more detail in the following chapter.

4.3 Conclusions

Samples of iron carbides and (carbo)nitrides were successfully synthesized by gaseous nitrocarburizing. In most cases, samples consisted of multiple phases. Pure single-phase specimens should be attainable by appropriate adjustments of the nitriding and carburizing potentials and optimization of the process, both in terms of treatment time and temperature but also the pretreatment for preparing porous iron foils. The pretreatment can be carried out in the same furnace as nitrocarburizing. If optimized, the process allows synthesis of homogeneous samples of tailored nitrogen and carbon content.

The process allows construction of a phase stability diagram for the Fe-N-C system similar to the Lehrer diagram for Fe-N system. Previous attempts based on gaseous nitrocarburizing in NH_3–H_2–CO atmospheres failed to provide water vapor contents of the gas mixtures (Naumann & Langenscheid, 1965a; b). This implies that activities of carbon were not determined. Since no oxygen is present in the current process, due to propene being used as carbon source, calculations of nitrogen and carbon activities are straightforward (equations 2.8 and 2.9).

A volumetric thermal expansion coefficient of $\alpha_{exp} = 1.5 \times 10^{-5}$ K^{-1} is obtained for the ferromagnetic state of cementite below approximately 480 K. Above this temperature (paramagnetic) the average value is $\alpha_{exp} = 4.3\ (2) \times 10^{-5}$ K^{-1} and for Hägg carbide the average

value is α_{exp} = 3.8 (2) × 10^{-5} K^{-1}. Initial lattice parameters as well as thermal expansion coefficients for ε-iron carbonitrides depend on the interstitial content.

Thermal decomposition of Hägg carbide (χ) and ε-carbonitride with high carbon content can by expressed by the following sequence: χ/ε → θ → α → γ. Decomposition to cementite (θ) occurs above 850 K. Above 950 K, ferrite (α) is formed and austenite (γ) above 1025 K. The sequential reduction in carbon content is presumably accompanied by graphite formation although this phase was not directly observed. Excess nitrogen is released as N_2.

For high nitrogen contents the decomposition sequence is: (ζ) → ε → γ′ → (γ) → α. If initially present, ζ is transformed to ε from 680 to 770 K, which decomposes to γ′ between 795 and 900 K as nitrogen is released as N_2. With further reduction of the nitrogen content, ferrite forms above 850 K. Austenite, stabilized by the presence of nitrogen, may be briefly formed around 900 K. Had experiments been continued to higher temperatures, above approximately 1025 K, the final decomposition product would have been austenite similar to the carbon-rich samples.

For the ε-nitride, the current results show that the structure is noticeably affected by partial substitution of nitrogen by carbon, at least in terms of lattice parameters. This could be a result of a change in interstitial ordering. In addition, possible changes in magnetic properties should also be considered. Structural and magnetic properties of the ε-carbonitrides are the subjects of the following chapter.

Chapter 5

Interstitial ordering and magnetism of ε-iron (carbo)nitride

Detailed information about the interstitial ordering in ε-iron carbonitrides is difficult to obtain with X-ray diffraction due to the low scattering power of nitrogen and carbon compared to iron. Light atoms may, however, contribute strongly to the diffracted intensity of neutrons, even in the presence of heavy atoms. The comparable nuclear scattering lengths of iron, nitrogen and carbon (Sears, 1992) enable a more accurate determination of interstitial occupancies. The occupational order of interstitials has previously been determined with neutron diffraction for several nitrogen contents in ε-Fe_2N_{1-z} and for one carbonitride of composition ε-$Fe_2(N_{0.80}C_{0.20})_{0.92}$ (Leineweber *et al.*, 2001). The occurrence of superstructure reflections, or lack thereof, was interpreted on the basis of thorough theoretical analysis of possible interstitial configurations (Leineweber & Jacobs, 2000). Complimentary information on the structural variation around iron sites can be obtained with Mössbauer spectroscopy (Chen *et al.*, 1983; Somers *et al.*, 1997).

No extended conclusions about the structure of the ε-carbonitrides can be drawn from the single observation of ε-$Fe_2(N_{0.80}C_{0.20})_{0.92}$ (Leineweber *et al.*, 2001). Even for the pure nitrides, the ordering of nitrogen is not completely understood, with apparent additional ordering occurring for the composition $Fe_2N_{0.81}$ and additional diffuse scattering observed in electron diffraction patterns for higher nitrogen contents (Leineweber *et al.*, 2001; Liu *et*

al., 2006). In order to investigate the interstitial ordering in ε-iron (carbo)nitrides, several samples with different nitrogen and carbon contents were synthesized and structural and magnetic properties characterized using neutron diffraction, vibrating sample magnetometry (VSM) and Mössbauer spectroscopy.

5.1 Experimental

Iron powder (99.0+% purity, Goodfellow Cambridge Ltd.) with a mean particle size of 6 – 8 μm were used for nitriding and nitrocarburizing with ammonia, nitrogen and hydrogen gasses of 99.999% and propene of 99.5% purity. Four samples were prepared in ceramic crucibles in a Netzsch STA 449 C Jupiter thermal analyzer at 718 K for 2.5 – 3 hours. Total flow rates of 55 – 68 mL/min were used with a constant N_2 flow of 5 mL/min for protection of electronics in the measurement compartment. In order to obtain sufficient amounts for all analyses, ten identical batches were combined to form each sample.

The compositions determined by combustion infrared detection (carbon content) on a LECO CS230 and by inert gas fusion thermal conductivity detection (nitrogen content) on a LECO TN500 is given in Table 5.1. The determined composition of $Fe_2(N_{0.757}C_{0.243})_{0.84}$ was corrected for the presence of small amounts (1.3% by mass) of γ′-Fe_4N in the sample, assuming stoichiometric composition and zero carbon content.

Table 5.1: Nitriding (K_N) and carburizing (K_C) potentials according to equations 2.8 and 2.9 and resulting sample composition.

K_N [atm$^{-1/2}$]	K_C [atm$^{-2/3}$]	Composition
∞	-	$Fe_2N_{0.91}$
21.26	-	$Fe_2N_{0.72}$
17.91	2.84	$Fe_2(N_{0.757}C_{0.243})_{0.84}$
49.09	5.44	$Fe_2(N_{0.819}C_{0.181})_{0.88}$

Two additional samples were prepared in a LAC PKRC55/09 furnace retrofitted for nitriding at 693 K for 55 to 80 hours. The applied gas flow rates and calculated sample compositions are given in Table 5.2. No hydrogen was added, which, assuming no dissociation of ammonia, leads to infinite potentials according to equations 2.8 and 2.9. Very similar sample compositions were obtained with a slightly higher carbon content using a propene flow rate of 19 mL/min.

An Agilent SuperNova diffractometer with an Atlas S2 CCD detector using Mo K_α radiation and calibrated with a LaB_6 standard was used for the determination of lattice parameters for $Fe_2N_{0.72}$. Neutron powder diffraction on the samples given in Table 5.2 was

performed using the MEREDIT diffractometer at the Nuclear Physics Institute ASCR in Řež, the Czech Republic. Samples were placed in vanadium containers with a diameter of 13 mm, and a monochromator consisting of three mosaic Cu(220) crystals provided a wavelength of λ = 1.46 Å. Data were collected at room temperature in a 2θ range of 4 – 144° (corresponding to a q range from 0.3 to 8.2 Å^{-1}) with a step size of 0.08° in 2θ.

Table 5.2: Gas flow rates of ammonia and propene, treatment time and resulting sample composition.

NH_3 [L/min]	C_3H_6 [mL/min]	Time [hours]	Composition
1	11	80	$Fe_2(N_{0.715}C_{0.285})_{0.92}$
1	19	55	$Fe_2(N_{0.706}C_{0.294})_{0.92}$

Additional neutron diffractograms were collected using the E3 diffractometer at Helmholtz-Zentrum Berlin (HZB), Germany (Wimpory *et al.*, 2008). Samples were placed in vanadium containers with a diameter of 8 mm under vacuum and data collected at room temperature, 373 K, 473 K and 573 K with a neutron wavelength of λ = 1.4892 Å. The applied wavelength and correction for diffraction angle (2θ) zero shift was determined from a Cu powder standard. Data were collected in a 2θ range of 40 – 103° (corresponding to a q range from 2.9 to 6.6 Å^{-1}) with a step size of 0.105° in 2θ. Rietveld refinements of intensity versus scattering angle (2θ) were carried out using the program WINPOW, a local variation of LHMP (Howard & Hill, 1986). Pseudo-Voigt profile functions were applied together with Chebyshev background polynomials.

Vibrating sample magnetometry was performed with a Lake Shore Cryotronics 7400 Series Vibrating Sample Magnetometer (VSM) equipped with either a single-stage variable temperature option (model 74035) or a low-temperature variable temperature cryostat (model 74018). The ^{57}Fe Mössbauer spectra were recorded using conventional constant acceleration spectrometers with sources of ^{57}Co in Rh on samples mixed with boron nitride powder. Spectra obtained at low temperatures were recorded in a closed cycle helium refrigerator (APD Cryogenics) and isomer shifts are given with respect to α-Fe at room temperature. Mössbauer spectra were fitted with Lorentzian line profiles and sextets were constrained to an intensity ratio of 3:2:1:1:2:3 and pairwise equal line widths.

5.2 Magnetic properties

Hysteresis curves and magnetization as a function of temperature for the ε-(carbo)nitrides (Figure 5.1) show a clear variation in magnetic properties with changing interstitial content. Except for $Fe_2N_{0.91}$, the saturation magnetization measured at 80 K in an applied field of B_0 =

1.6 T decreases for increasing interstitial content. A similar trend is noticed for the Curie temperatures, T_C, (Table 5.3) determined as the zero-point of the second derivative of the magnetization curves (Fabian *et al.*, 2013). Below the Curie temperature all samples can be classified as soft ferromagnetic materials. The decreasing magnetization and Curie temperature with increasing nitrogen content is well-known for ε-iron nitride (Bouchard *et al.*, 1974; Kano *et al.*, 2001; Leineweber *et al.*, 2001), but in one case deviations have been observed due to the presence of carbon (Leineweber *et al.*, 2001).

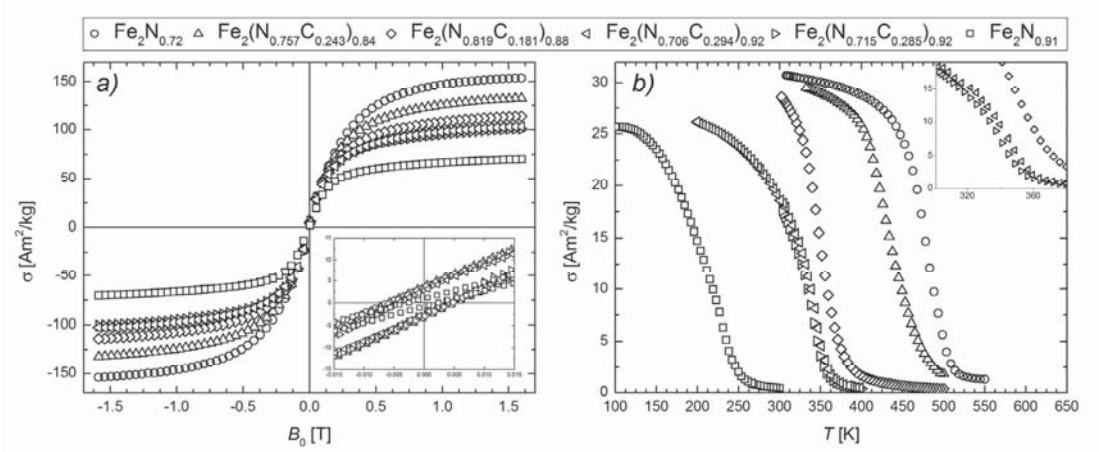

Figure 5.1: *a*) Magnetic hysteresis curves for ε-iron (carbo)nitrides at 80 K and *b*) specific magnetization versus temperature at B_0 = 0.05 T measured at a cooling rate of 1.5 K/min. For clarity only every 30th measurement point is shown except for the inset in *a*).

The variation in magnetic properties can, at least qualitatively, be explained by a simple donor model in which nitrogen partially donates 2*p* electron density to the iron 3*d* band (Eickel & Pitsch, 1970; Chen *et al.*, 1983). With increasing nitrogen content, holes in the partially filled band of minority spins are gradually filled, reducing the difference between majority and minority spins. Substitution of nitrogen by carbon has in one case been shown to cause an increase in both magnetization and Curie temperature (Leineweber *et al.*, 2001). This is in agreement with the donor model since carbon has only two 2*p* electrons compared to three for nitrogen.

Table 5.3: Curie temperature (T_C) and specific saturation magnetization (σ_s) at 80 K in an applied field of B_0 = 1.6 T determined for ε-iron (carbo)nitrides.

Sample	$Fe_2N_{0.72}$	$Fe_2(N_xC_{1-x})_{0.84}$	$Fe_2(N_xC_{1-x})_{0.88}$	$Fe_2(N_xC_{1-x})_{0.92}$	$Fe_2(N_xC_{1-x})_{0.92}$	$Fe_2N_{0.91}$
x	-	0.757	0.819	0.706	0.715	-
σ_s [Am²/kg]	154	132	114	103	101	71
T_C [K]	480	431	349	340	336	222

Curie temperatures for the two pure nitride samples are comparable to published literature values as seen in Figure 5.2. The values for the carbonitride samples are clearly increased compared to the relation between Curie temperature and interstitial content for pure ε-nitrides. The previously published single observation of increased magnetization and Curie temperature for ε-iron carbonitrides compared to nitrides of similar total interstitial content (Leineweber *et al.*, 2001) is thus confirmed as a general trend.

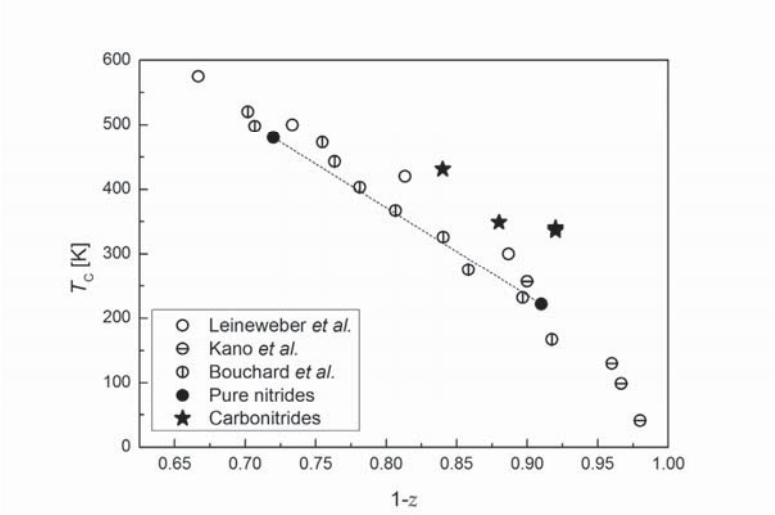

Figure 5.2: Curie temperature (T_C) obtained for ε-Fe_2N_{1-z} and ε-$Fe_2(N,C)_{1-z}$ compared to the values obtained for ε-Fe_2N_{1-z} by Leineweber *et al.* (2001), Kano *et al.* (2001) and Bouchard *et al.* (1974). A dotted line is drawn between the two pure nitride samples to emphasize the increased T_C of the carbonitrides.

5.2.1 Mössbauer spectroscopy

The presence of magnetic ordering at low temperatures is confirmed by Mössbauer spectroscopy. Each individual spectrum recorded at 18 K (Figure 5.3) could be fitted with a combination of three sextets. The sextet components correspond to Fe surrounded by one (I), two (II) or three (IIIa and IIIb) nitrogen or carbon atoms (Chen *et al.*, 1983; Somers *et al.*, 1997). In the ideal structure of ε-Fe_3N only component II should be observed, but increasing nitrogen or carbon contents, $z < 1/3$ for ε-$Fe_2(N,C)_{1-z}$, leads to some iron atoms having three N/C nearest neighbors. Four nearest neighbors are not observed due to the repulsive nature of the interactions of simultaneously occupied face-sharing octahedral positions.

The sextet corresponding to just one nitrogen nearest neighbor was only observed for $Fe_2N_{0.72}$ (Table 5.4). This configuration occurs according to the reaction 2 (II) → (I) + (III) due to partial disordering (Chen *et al.*, 1983; Leineweber *et al.*, 2001). The fractional occupancy of interstitials per two iron atoms (=1-*z*) for ε-$Fe_2(N,C)_{1-z}$ can be calculated as $\Sigma f_i(i/3)$, where f_i is the relative area of sextets corresponding to iron atoms surrounded by i = 1, 2 or 3 nitrogen or carbon atoms.

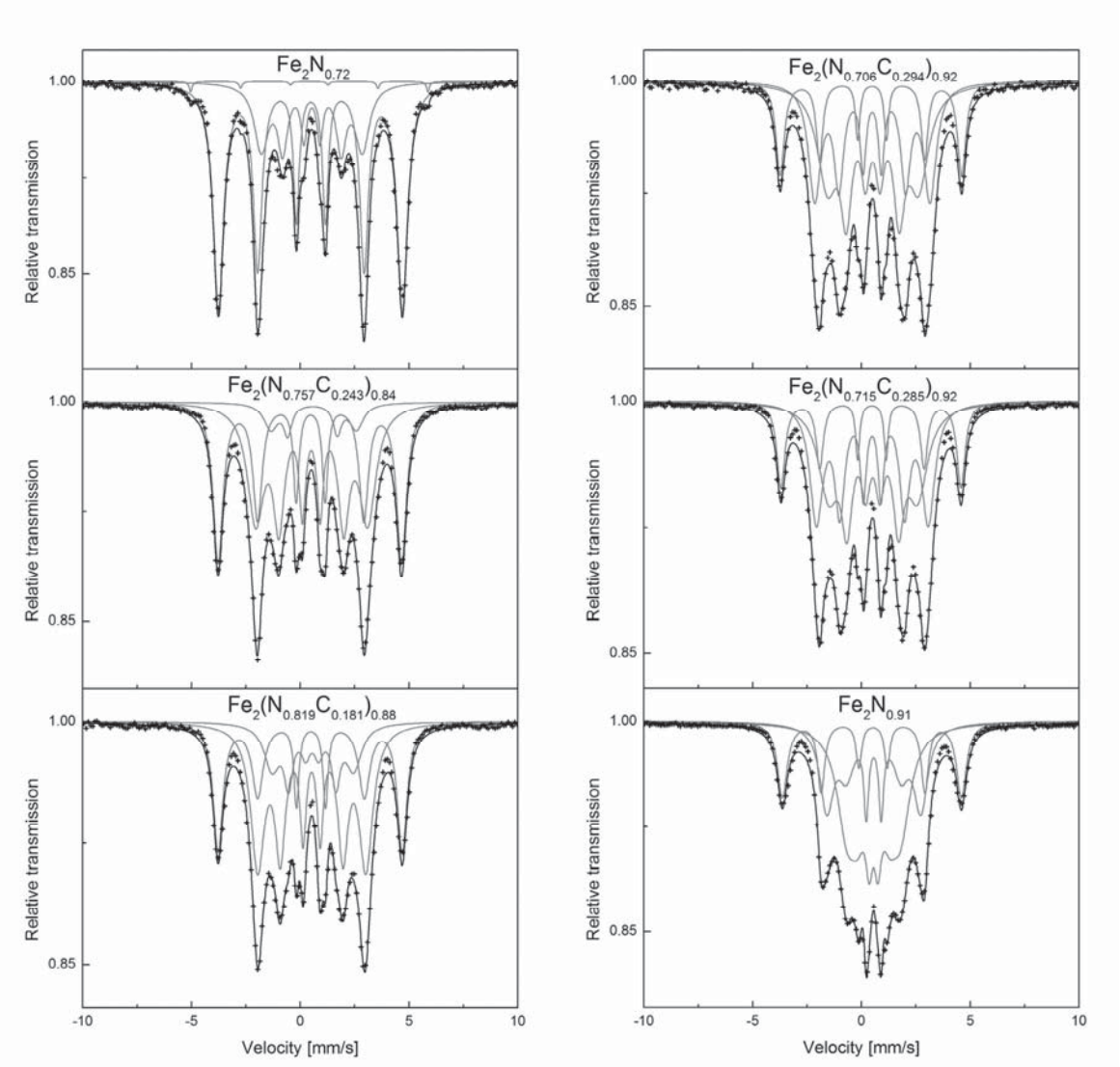

Figure 5.3: Mössbauer spectra of ε-iron (carbo)nitrides recorded at 18 K. Data are presented as points, fits as black lines and the individual sextet components as grey lines.

The calculated values only slightly overestimate the total interstitial content (Table 5.4). A perfect agreement is not expected within experimental accuracy, but the systematic deviation is likely a consequence of fitting individual sextets to components that are actually characterized by a distribution in hyperfine fields (Chen *et al.*, 1983). This is evident from broadening of spectral lines, and particularly the component corresponding to three interstitial nearest neighbors requires at least two sextets (IIIa and IIIb) in order to obtain reasonable fits. Line widths in excess of 1 mm/s are observed compared to an instrumental value of approximately 0.25 mm/s. Chen *et al*. offered an approximate interpretation involving the surrounding iron atoms (second coordination shell). These may, themselves, be predominantly surrounded by either two or three interstitial atoms, causing the two

different observed iron environments. With a few exceptions available literature data for ε-Fe_2N_{1-z} (Chen *et al.*, 1983; Somers *et al.*, 1997; Pekelharing *et al.*, 1999) qualitatively agrees with this simplified interpretation.

The entire distribution in hyperfine fields presumably depends on the various exact configurations around neighboring iron atoms. First principles calculations of hyperfine interactions have, so far, focused on fully ordered systems without contributions from possible configurations of surrounding iron atoms (Shang *et al.*, 2006). This limits the possibility for quantitative interpretation of the distributions, and the individual components typically fitted for the ε-nitrides was therefore used.

Table 5.4: Hyperfine field (B_{hf}), isomer shift (δ) and relative contribution (f_i) of sextets designated I, II, IIIa and IIIb fitted to Mössbauer spectra of ε-$Fe_2(N,C)_{1-z}$ powder samples recorded at 18 K. $\Sigma f_i(^i/_3)$ is the fractional occupancy of interstitials per two iron atoms (= 1-*z*) as calculated from the relative contributions of iron atoms surrounded by i = 1, 2 or 3 nitrogen or carbon atoms.

	Sample	$Fe_2N_{0.72}$	$Fe_2(N_{1-x}C_x)_{0.84}$	$Fe_2(N_{1-x}C_x)_{0.88}$	$Fe_2(N_{1-x}C_x)_{0.92}$	$Fe_2(N_{1-x}C_x)_{0.92}$	$Fe_2N_{0.91}$
	x	-	0.243	0.181	0.294	0.285	-
	B_{hf} [T]	33.8	-	-	-	-	-
I	δ [mm/s]	0.41	-	-	-	-	-
	f [%]	0.8	-	-	-	-	-
	B_{hf} [T]	26.2	26.2	26.2	25.9	25.7	25.5
II	δ [mm/s]	0.47	0.46	0.47	0.46	0.46	0.50
	f [%]	71.2	41.1	31.7	18.5	17.5	21.0
	B_{hf} [T]	14.4	16.0	15.4	16.4	15.9	13.4
IIIa	δ [mm/s]	0.53	0.51	0.52	0.50	0.50	0.56
	f [%]	28.0	49.5	49.9	34.4	38.2	31.9
	B_{hf} [T]	-	12.2	11.7	13.0	12.7	7.7
IIIb	δ [mm/s]	-	0.59	0.56	0.52	0.52	0.56
	f [%]	-	9.4	18.4	47.1	44.3	47.1
	Σf_i ($^i/_3$)	0.76	0.86	0.89	0.94	0.94	0.93

Fitted hyperfine fields (B_{hf}) and isomer shifts (δ) are given in Table 5.4. Quadrupole shifts are small and the quality of the fits does not deteriorate if constrained to zero, in agreement with the results of Chen *et al*. (1983). These values are therefore not tabulated. Hyperfine fields and isomer shifts are compared to values for ε-Fe_2N_{1-z} in Figure 5.4. Hyperfine fields for the carbonitrides are consistently higher than for nitrides of similar total interstitial content, which is consistent with the donor model and magnetization measurements.

The donor model also explains the reduced isomer shifts of the carbonitrides since reduced screening from *d*-electrons increases the effective *s*-electron density at the iron nuclei. It is noted that the trend is not apparent for component IIIb, which also displays significantly scattered literature values. This is most likely caused by the difficulty in fitting superimposed components and the discussed distributions in hyperfine fields, as opposed to well-defined sextets.

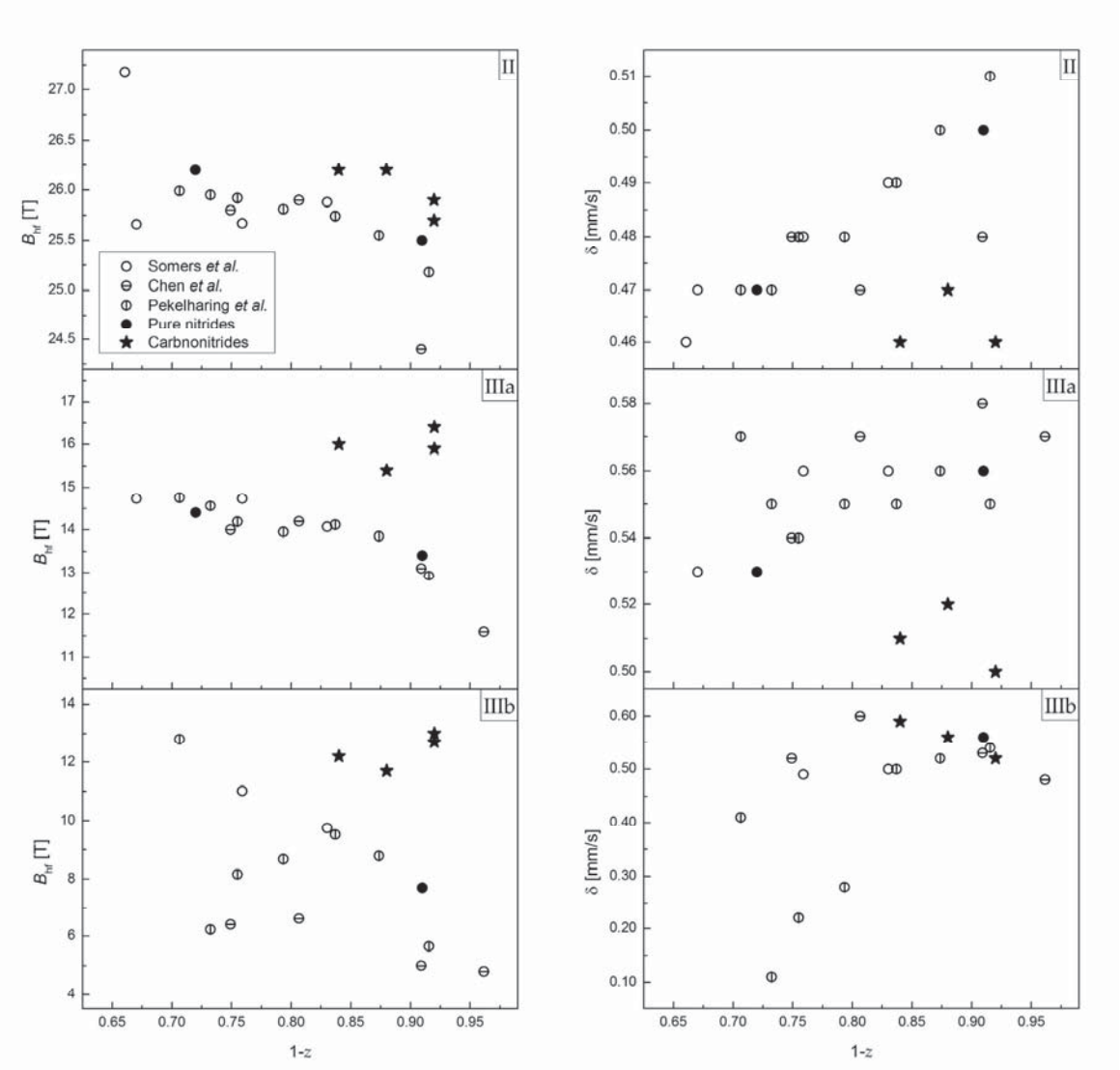

Figure 5.4: Hyperfine fields (B_{hf}) and isomer shifts (δ) for ε-Fe_2N_{1-z} and ε-$Fe_2(N,C)_{1-z}$ at 18 K compared to the values obtained for ε-Fe_2N_{1-z} by Chen *et al.* (1983), Somers *et al.* (1997) and Pekelharing *et al.* (1999) at 4.2 K.

5.3 Neutron diffraction

Figure 5.5 shows neutron diffractograms recorded using the diffractometer MEREDIT@NPI for the two samples $Fe_2(N_{0.706}C_{0.294})_{0.92}$ and $Fe_2(N_{0.715}C_{0.285})_{0.92}$. In both cases, class (001) superstructure reflections were observed, which are systematically extinct for space group $P6_322$ (see Section 2.2.1 for a description of structural models for ε-iron nitride and classes of superstructure reflections). Additional reflections, which coincide with the superstructure reflections, are present due to a small $\lambda/2$-contribution (intensity ratio 0.4% of the primary

neutron wavelength, λ) from the applied monochromator. For space group $P6_322$, the $\lambda/2$-contribution cannot entirely explain the observed intensities (Figure 5.5*c-f*). The presence of class (001) superstructure reflections and thus the $P\bar{3}1m$ structural model for the ε-carbonitrides, as suggested by Leineweber *et al.* (2001), is therefore confirmed.

A comparison of the structural models shows that going from space group $P6_322$, with Wyckoff positions 2*b* and 2*c* occupied, to $P\bar{3}1m$ with occupation of 1*a* and 2*d* corresponds to an increase in the degree of long range order. The structure of ε-Fe_2N_{1-z} described in space group $P6_322$ leads to occupation of Wyckoff site 2*b* (i.e. C1 and C2, cf. Table 2.1 and Figure 2.4) for $z < 1/3$ (Leineweber *et al.*, 2001). Since occupation of C1 sites directly above or below occupied C2 sites does not occur, the structure can only be realized by short range ordering. For the carbonitrides in space group $P\bar{3}1m$ short range ordering is not necessary if only positions 1*a* and 2*d* are occupied.

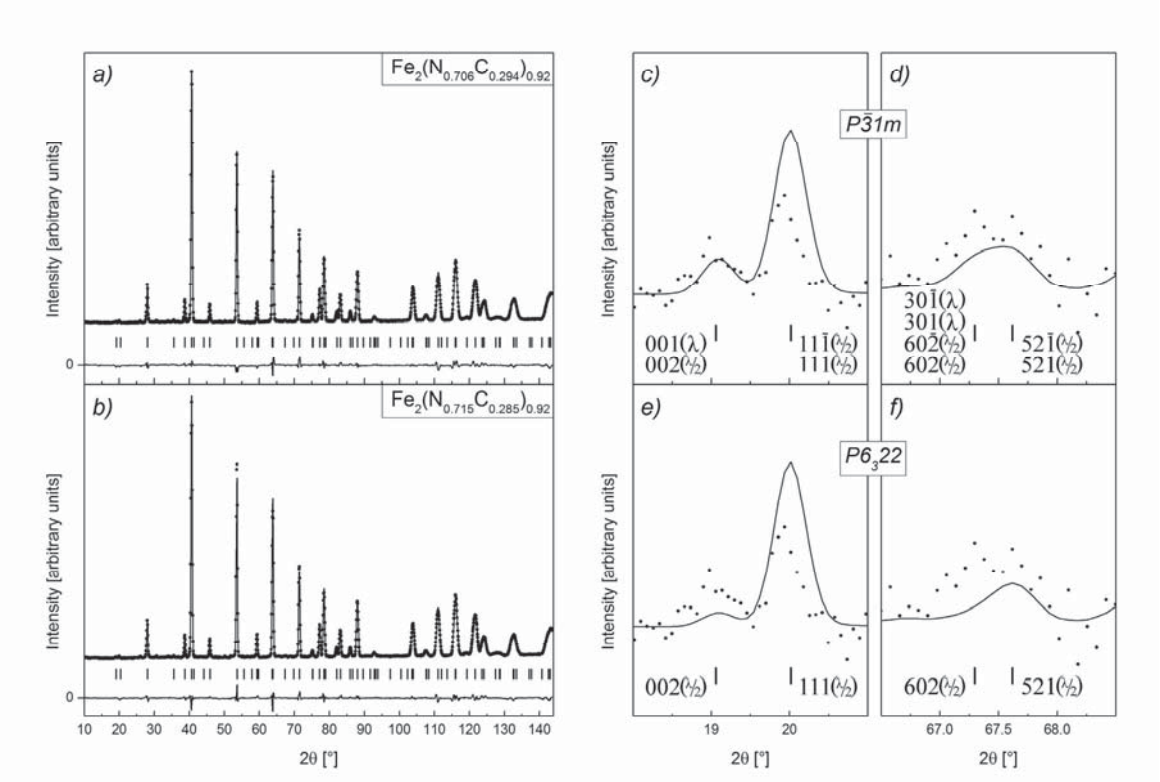

Figure 5.5: Neutron diffractogram (MEREDIT diffractometer, λ = 1.46 Å), refined Rietveld profile and difference curve for *a*) $Fe_2(N_{0.706}C_{0.294})_{0.92}$ and *b*) $Fe_2(N_{0.715}C_{0.285})_{0.92}$. Comparison of superstructure reflections of structural models in space group $P\bar{3}1m$ (*c+d*) and $P6_322$ (*e+f*) for $Fe_2(N_{0.715}C_{0.285})_{0.92}$. Note the $\lambda/2$-contribution (intensity ratio 0.004).

Refinements were carried out with fixed C/N ratios at each site and the total number of interstitials constrained to the determined nitrogen and carbon content. Refined C/N occupancies are listed in Table 5.5. For Wyckoff positions 1*b* and 2*c* occupancies refined to slightly negative values and were consequently fixed to zero.

Table 5.5: Lattice parameters (*a* and *c*), combined occupancy of Wyckoff sites by nitrogen and carbon (ρ), profile residual (R_p) and goodness-of-fit value (χ^2) obtained from Rietveld refinements.

Sample	$Fe_2(N_{0.706}C_{0.294})_{0.92}$	$Fe_2(N_{0.715}C_{0.285})_{0.92}$
a [Å]	4.7813(2)	4.7830(2)
c [Å]	4.4019(1)	4.4020(1)
$\rho(1a)$	0.882(10)	0.994(13)
$\rho(2c)$	0.070 (4)	0.122 (4)
$\rho(2d)$	0.876 (2)	0.767 (4)
R_p [%]	4.17	3.75
χ^2	9.26	5.40

Minor changes in interstitial content is seen to noticeably affect refined occupancies, with a slight increase in carbon content causing a more even distribution of interstitials, $\rho(1a) \approx \rho(2d)$. It should, however, be noted that this result is obtained assuming a fixed N/C ratio at each interstitial position, which is unlikely to be the case as discussed in Section 5.4. In addition, treatment times were markedly different for the two samples and thermal history may affect interstitial ordering (Liapina *et al.*, 2004).

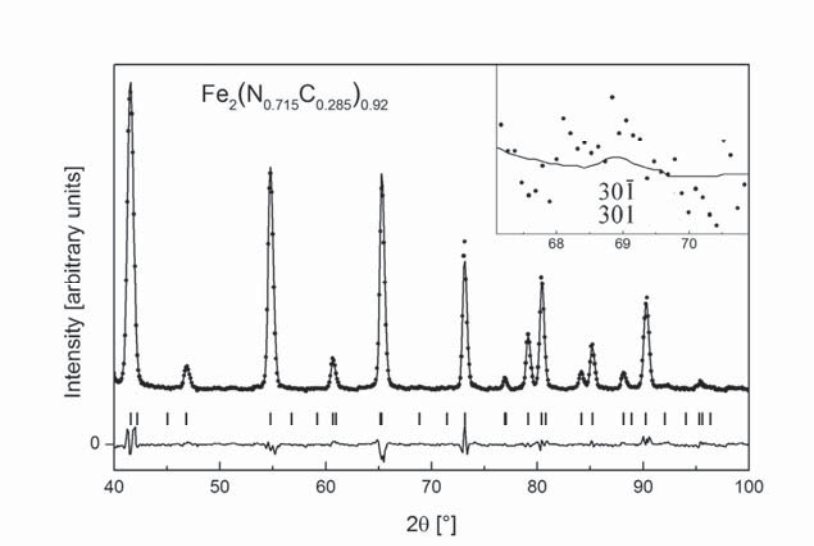

Figure 5.6: Neutron diffractogram (E3 diffractometer, λ = 1.4892 Å), refined Rietveld profile and difference curve for $Fe_2(N_{0.715}C_{0.285})_{0.92}$ with occupancies fixed at the values given in Table 5.5.

Due to a lower signal/noise ratio and a limited 2θ range of neutron diffractograms for the remaining samples (E3 diffractometer at HZB), refined occupancies did not yield consistent results. Figure 5.6 shows the neutron diffractogram and Rietveld profile for $Fe_2(N_{0.715}C_{0.285})_{0.92}$ with occupancies fixed at the values given in Table 5.5. Although reliable

occupancies were not obtained, refinements did indicate increased disorder at elevated temperatures as evidenced by increasing occupancy of Wyckoff site 2*d* for $Fe_2N_{0.91}$ ($P6_322$) and 2*c* for the carbonitrides ($P\bar{3}1m$). Lattice parameters are consistent between the two data sets as seen by comparing the values for $Fe_2(N_{0.706}C_{0.294})_{0.92}$ and $Fe_2(N_{0.715}C_{0.285})_{0.92}$ listed in Tables 5.5 and 5.6.

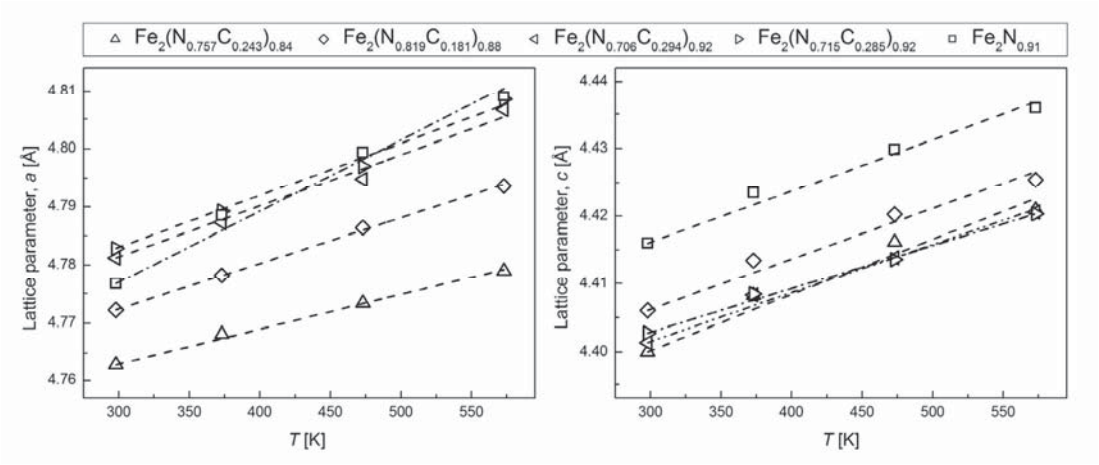

Figure 5.7: Lattice parameters (*a* and *c*) versus temperature for ε-iron (carbo)nitrides. Estimated standard deviations are ≤ 10^{-3} Å. Lines correspond to fitted expressions for thermal expansion (equation 4.1).

Thermal expansion in terms of lattice parameters *a* and *c* is approximately linear up to the maximum investigated temperature of 573 K and can be fitted to equation 4.1 (Figure 5.7). Initial lattice parameters and expansion coefficients (Table 5.6) follow the general trends outlined in Chapter 4; i.e. increasing interstitial content increases *a* and thermal expansion in that direction (except for $Fe_2N_{0.91}$) while a more complicated relation exists for *c*.

Table 5.6: Lattice parameters (*a* and *c*) at room temperature and expansion coefficients fitted to equation (4.1) in terms of the lattice parameters and unit cell volume (*V*) for ε-iron (carbo)nitrides.

Sample	$Fe_2(N_{1-x}C_x)_{0.84}$	$Fe_2(N_{1-x}C_x)_{0.88}$	$Fe_2(N_{1-x}C_x)_{0.92}$	$Fe_2(N_{1-x}C_x)_{0.92}$	$Fe_2N_{0.91}$
x	0.243	0.181	0.294	0.285	-
a(RT) [Å]	4.7630(7)	4.7723(5)	4.7812(3)	4.7829(2)	4.7768(4)
c(RT) [Å]	4.4000(4)	4.4060(3)	4.4014(2)	4.4027(2)	4.4160(3)
$\alpha_{exp}(a)$ [×10^{-5} K^{-1}]	1.23 (3)	1.65 (2)	1.84 (8)	1.87 (7)	2.56(11)
$\alpha_{exp}(c)$ [×10^{-5} K^{-1}]	1.87(13)	1.70(10)	1.62 (6)	1.45 (4)	1.71 (8)
$\alpha_{exp}(V)$ [×10^{-5} K^{-1}]	4.35(17)	5.02(12)	5.32(15)	5.21(15)	6.87(31)

5.4 Discussion

Since most of the studied samples have Curie points above room temperature, contributions from magnetic ordering in neutron diffractograms are expected. For the ε-(carbo)nitrides nuclear and magnetic reflections coincide, but some disagreement exists over whether magnetic moments are aligned perpendicular (Leineweber *et al.*, 1999, 2001) or parallel (Robbins & White, 1964; Fang *et al.*, 2013) to the hexagonal *c* axis. Several magnetic models were attempted in analyzing the current data, but magnetic structures could not be resolved and are therefore not included in Rietveld refinements.

Lattice parameters for ε-$Fe_2(N,C)_{1-z}$, including samples discussed in Chapter 4, are plotted versus total interstitial content (1-*z*) in Figure 5.8(*a*). Within experimental accuracy the *a* parameter corresponds to published relations for pure ε-nitrides (Somers *et al.*, 1997; Liapina *et al.*, 2004) and carbonitrides (Firrao *et al.*, 1979) while there are significant deviations for *c*. The deviations increase for increasing carbon content.

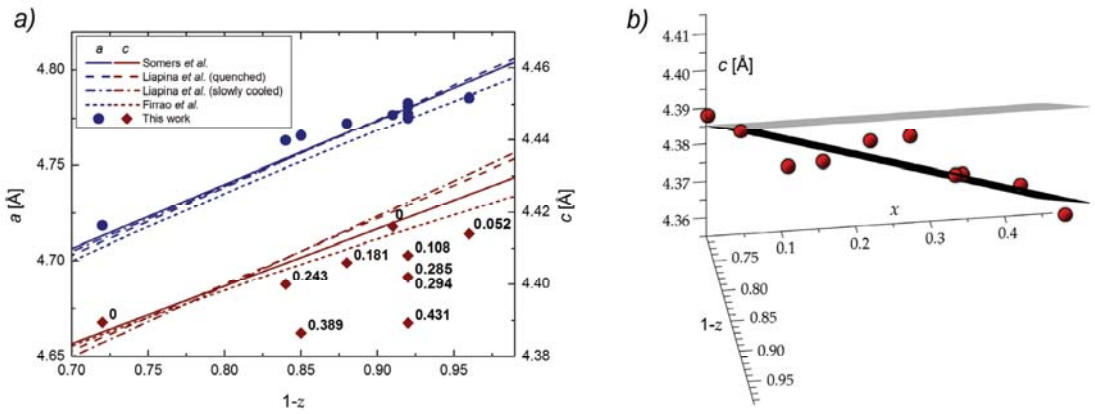

Figure 5.8: *a*) Lattice parameters versus interstitial content for ε-$Fe_2(N_{1-x}C_x)_{1-z}$ compared to published relations for pure nitrides by Somers *et al.* (1997) and Liapina *et al.* (2004) and carbonitrides by Firrao *et al.* (1979). Labels denote the fraction of interstitial carbon atoms, *x*. *b*) Lattice parameter *c* plotted against published relation (Somers *et al.*, 1997) assuming no change on substitution of nitrogen by carbon (grey) and fitted relation (black) with correction for carbon content (equation 5.1).

A reduced compositionally induced expansion in *c* while *a* is mostly unaffected is in contradiction to the initial results obtained by Jack (1948b), where a reduction in both *a* and *c* were observed for partial substitution of nitrogen by carbon. The current observations are, however, supported by later findings of Naumann & Langenscheid (1965b).

Based on the published relation between lattice parameter *c* and interstitial content for ε-Fe_2N_{1-z} by Somers *et al.* (1997), *c* [Å] = 4.2723 + 0.159(1-*z*), a correction term can be added for the fraction of interstitial carbon atoms, *x*, in ε-$Fe_2(N_{1-x}C_x)_{1-z}$. A least squares fit to the

current data yields a value for the correction term of –0.057(6) Å, resulting in the following relation for *c*:

$$c\ [\text{Å}] = 4.2723 + 0.159(1\text{-}z) - 0.057x \tag{5.1}$$

This fit does not completely describe the changes in lattice parameter for the carbonitrides but is a significant improvement compared to using the relation for the pure nitrides (Figure 5.8).

The anisotropic effect on lattice parameters suggests that carbon does not randomly substitute nitrogen, i.e. carbon preferentially occupies certain crystallographic sites. This cannot be directly verified by the refined occupancies since Rietveld refinements were carried out with a fixed N/C ratio at each interstitial position. It can, however, be understood from the nature of the compositionally induced lattice expansion. As noted in Section 4.2.2, edge-sharing contacts of octahedral interstitial positions occur exclusively parallel to (001). Simultaneous occupation of these positions causes repulsive interactions, which are accommodated by preferential expansion of the structure in that direction. For an ideal structure described in space group $P\bar{3}1m$, only Wyckoff sites 1*a* and 2*d* are occupied, corresponding to sites designated A1, B2 and C2 cf. Table 2.1. Edge-sharing contacts occur between B2 and C2 (2*d*). Since the lattice parameter *a* is comparable for ε-nitrides and carbonitrides it can thus be assumed that these sites are preferentially occupied by nitrogen.

The expansion perpendicular to (001) is primarily governed by occupation of site A1 (1*a*). For preferred carbon occupancy of this site, a reduced lattice parameter *c* can be seen as a result of favorable (less repulsive) C-N interactions compared to N-N. If only interstitials are considered for an ordered structure, in which nitrogen fully occupies 2*d* and carbon 1*a*, each nitrogen atom is surrounded by three N nearest neighbors in directions parallel to (001). Carbon, on the other hand, is surrounded by twelve N nearest neighbors, although separated by a slightly larger distance (by a factor of approximately 1.3). The structure may thus be viewed as a result of maximizing the number of relatively favorable C-N interactions.

Variations in the axial ratio *c*/*a* at elevated temperatures can be interpreted in terms of thermal disorder, although magnetic interactions prevail for low interstitial contents (Leineweber *et al.*, 2004). Disordering leads to an increased number of edge-sharing contacts. Both increasing disorder and increasing interstitial content thus cause a preferential expansion of the structure parallel to (001) planes. Increasing interstitial content will therefore tend to decrease the ratio of expansion coefficients $\alpha_{exp}(c)/\alpha_{exp}(a)$ as seen in

Figure 5.9. Increased ratios are observed for higher carbon contents due to the relatively favorable C-N interactions.

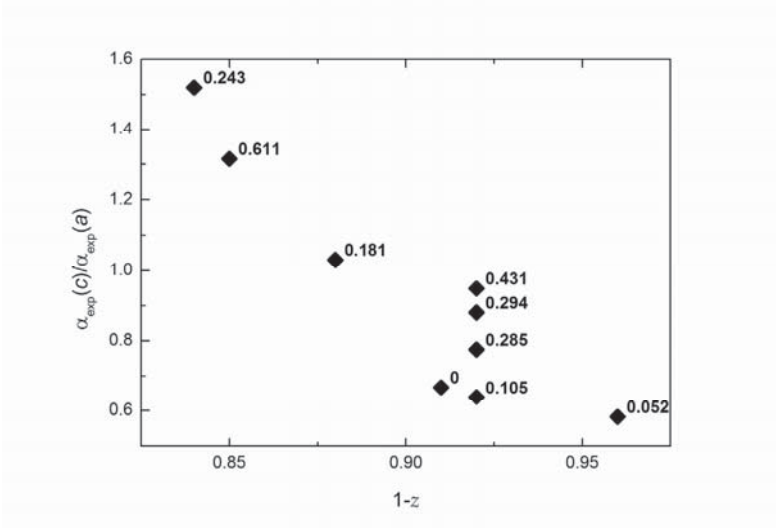

Figure 5.9: Ratio of thermal expansion coefficients $\alpha_{exp}(c)/\alpha_{exp}(a)$ for ε-$Fe_2(N_{1-x}C_x)_{1-z}$. Labels denote the fraction of interstitial carbon atoms, x.

5.5 Conclusions

Partial substitution of nitrogen by carbon in ε-iron nitride affects both magnetic and structural properties. Trends in magnetic properties can be explained by the donor model in which nitrogen and carbon partially donate 2*p* electron density to the iron 3*d* band. Curie temperatures, magnetization and hyperfine fields are increased, while isomer shifts of iron are decreased in the carbonitrides, since carbon has only two 2*p* electrons whereas nitrogen has three.

The two components identified in Mössbauer spectra corresponding to iron atoms surrounded by three nitrogen or carbon atoms (IIIa and IIIb) should be interpreted as an approximation for the distribution in hyperfine fields caused by both the number and configuration of interstitial atoms around neighboring iron atoms.

The carbonitrides are described in space group $P\bar{3}1m$ as opposed to $P6_322$ for the pure nitrides, evidenced by the presence of class (001) superstructure reflections. The thresholds in both total interstitial content and carbon content that must be exceeded in order to change the symmetry have not been investigated. Changes in interstitial ordering are deduced from the observed effects on lattice parameters. Relatively favorable C-N interactions lead to additional ordering and a decrease in the lattice parameter *c* while *a* is largely unaffected. These effects are also apparent for the anisotropic thermal expansion.

Chapter 6

Expanded austenite: Thermal expansion, decomposition and magnetism

The thermal stability of nitrogen expanded austenite has previously been investigated with thermogravimetry and differential thermal analysis, and it was demonstrated that under an inert atmosphere it is associated with the development of molecular nitrogen gas, chromium nitride, ferrite and nitrogen-depleted austenite (Christiansen & Somers, 2006b). For austenitic stainless steel containing molybdenum (AISI 316L), it was hypothesized, on the basis of scarce data, that decomposition occurred by discontinuous precipitation, while for molybdenum-free stainless steel (AISI 304L), a eutectoid transformation contributed to decomposition.

This chapter presents results on the thermal behavior of expanded austenite investigated using *in situ* synchrotron XRD and Rietveld refinement. Homogeneous samples are needed in order to avoid the influences of composition-induced stresses and asymmetric broadening of diffraction peaks. For this reason, austenitic stainless steel powder was used in order to obtain a homogeneous distribution of interstitials throughout the entire sample. Powder samples of expanded austenite were synthesized with high and low nitrogen contents, high and low carbon contents and one sample incorporating both nitrogen and carbon. Additional samples of nitrogen expanded austenite were synthesized

from thin foils of austenitic stainless steel. The last section of the chapter presents results on the magnetic properties of expanded austenite produced from thin foils.

6.1 Nitrogen expanded austenite

For the initial investigation of the composition dependent thermal expansion and decomposition, two powder samples of nitrogen expanded austenite, γ_N, were produced. In order to describe the obtained diffraction data, a structural model similar to that described by Christiansen & Somers (2004) was used: an f.c.c. lattice with stacking faults contributing to systematic deviations of XRD peaks as described by Warren (1969). There are certain problems with this model (see Section 2.2.3 and Chapter 7), but no entirely acceptable and implementable structural description exists at this point.

6.1.1 Experimental

Gaseous nitriding of 5 μm AISI 316 grade stainless steel powder (Höganäs AB), with composition from chemical analysis given in Table 6.1, was performed in ceramic crucibles in a Netzsch STA 449 C Jupiter thermal analyzer. Ammonia, nitrogen and hydrogen gasses of 99.999% purity were applied. A sample with high nitrogen content was synthesized in an atmosphere of 95 vol.% NH_3 and 5 vol.% N_2 (corresponding to an infinite nitriding potential cf. equation 2.8) in two temperature steps: initially at 693 K for 4 hours followed by 673 K for 25 hours. A sample with low nitrogen content was produced by denitriding the high-nitrogen sample at 693 K for 2 hours in a gas consisting of 91 vol.% H_2 and 9 vol.% N_2 (corresponding to a nitriding potential of zero). Thermogravimetric curves are given in Figure 6.1.

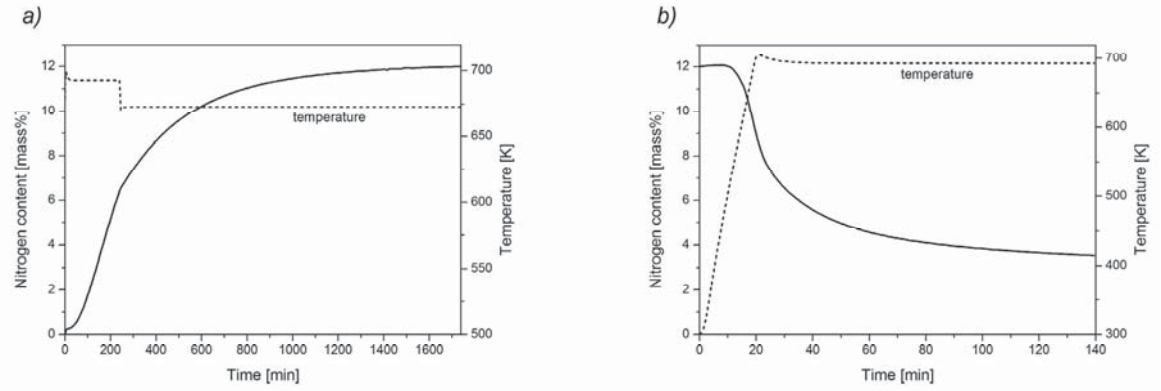

Figure 6.1: Thermogravimetric curves for *a*) expanded austenite with high nitrogen content synthesized with a two-step temperature program; 693 K followed by 673 K with infinite nitriding potential and *b*) low nitrogen content synthesized by denitriding the high-nitrogen sample with a nitriding potential of zero. Denitriding was carried out at 693 K with the retraction of nitrogen occurring already during heating.

Table 6.1: Chemical composition of untreated AISI 316 powder in mass%.

Fe	Cr	Ni	Mo	Mn	C	N	S
Balance	16.2	13.3	2.3	<0.2	<0.05	<0.05	<0.005

The nitrogen content in the nitrided samples was calculated from the total nitrogen uptake/release during nitriding/denitriding. In order to remove the passive oxide film prior to nitriding, a proprietary process for surface activation has been applied, for which additional details cannot be disclosed. Unless otherwise stated, this method was applied for all synthesized samples of nitrogen expanded austenite, and is referred to simply as *activation* (For exceptions see Section 6.4.1 and Appendix B.1).

6.1.1.1 Synchrotron X-ray diffraction

Diffractograms were collected at a wavelength of λ = 1.07051(2) Å in transmission mode with a Huber G670 Guinier camera at MAX-lab beamline I711 (Cerenius *et al.*, 2000). In order to reduce the influence of fluorescence radiation, aluminium foils were positioned between the sample and the detector. Samples were mounted in 0.7 mm inner diameter quartz capillaries filled with an inert argon atmosphere to avoid oxidation and heated in a Huber 670.3 furnace. Temperature calibration and determination of the applied wavelength were performed using a Si standard. The correction for diffraction angle (2θ) zero shift was determined from the untreated reference sample. For each sample, 26 diffractograms were measured in the temperature range 385 – 920 K. Data were collected in a 2θ range of 4 – 100° (corresponding to a q range from 0.4 to 9.0 Å^{-1}), with a fixed step size of 0.005° in 2θ and an exposure time of 240 seconds at each temperature step. After exposure, the temperature was immediately ramped to the next set point, and the average time for reaching and stabilizing at each set point temperature prior to exposure was 226 seconds. Rietveld refinements of intensity versus scattering angle (2θ) were carried out using the program *WINPOW*, a local variation of *LHMP* (Howard & Hill, 1986), in order to fit lattice parameters and mass fractions of the constituent phases. Pseudo-Voigt profile functions were applied together with Chebyshev background polynomials. In order to incorporate the effect of stacking faults on the peak positions of expanded austenite reflections, the relation derived by Warren (1969) was included in the Rietveld refinements. For all refinements residual values of $R_p \leq 1.29\%$ and goodness-of-fit values $\chi^2 \leq 1.43$ were obtained.

6.1.2 Results and interpretation

The morphology of the powder is shown on the scanning electron microscopy (SEM) micrograph in Figure 6.2, which confirms a mean particle size of 5 μm. X-ray diffractograms (Figure 6.3) show that the untreated powder contains two phases; austenite (γ) and a

significant amount of a ferritic b.c.c. phase (α). The thermodynamic equilibrium of AISI 316 is a mixture of austenite and ferrite (Kjeldsen, 2013), but chromium-rich δ-ferrite could also have formed during solidification of the powder. The phase composition determined by Rietveld refinement (Figure 6.3*a*) is 13.7(1) mass% α and 86.3(1) mass% γ. In order to avoid sintering of the fine powder, it was not fully austenitized before nitriding and the presence of ferrite thus had to be tolerated.

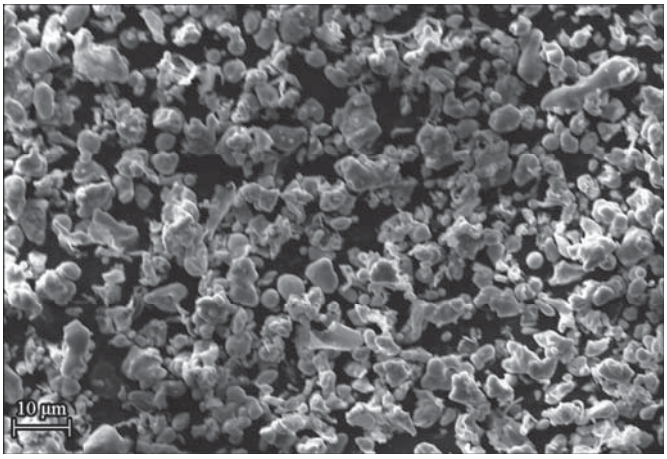

Figure 6.2: SEM secondary electron image showing the morphology of the AISI 316 powder; the mean particle size is 5 mm.

The high-nitrogen sample was obtained by nitriding of the AISI 316 powder until a stationary weight gain was reached, suggesting an imposed equilibrium between nitrogen in the gas phase and in the stainless steel. After 29 hours treatment time, all austenite was transformed and the nitrided sample consisted mainly of expanded austenite (Figure 6.3*b*). Previous investigations on precipitation hardening stainless steel have shown that nitriding of b.c.c. phases leads to a tetragonal distortion, followed by transformation to γ_N for sufficiently high nitrogen activities, owing to the austenite-stabilizing effects of N (Frandsen *et al.*, 2006). This effect is not immediately apparent from the present data since the ferritic phase is partially retained in the nitrided sample, although a slight broadening of ferrite peaks was observed. An additional broad peak is present between the 111 and 200 reflections of expanded austenite (q = 2.99 A^{-1}), which cannot be explained by the α or γ_N phases. This peak is attributed to the presence of the nitride ε-M_2N_{1-z}, with M representing the metallic composition of the AISI 316 matrix. The nitride is based on an h.c.p. lattice of metal atoms and a composition corresponding to $z \simeq 0.1$ is estimated from comparison with the lattice parameters reported for ε-Fe_2N_{1-z} (Somers *et al.*, 1997). No higher-order reflections from this phase are discernible, but additional diffractograms recorded to verify the identity (not shown) did indicate the presence of a 112 peak of the ε-phase.

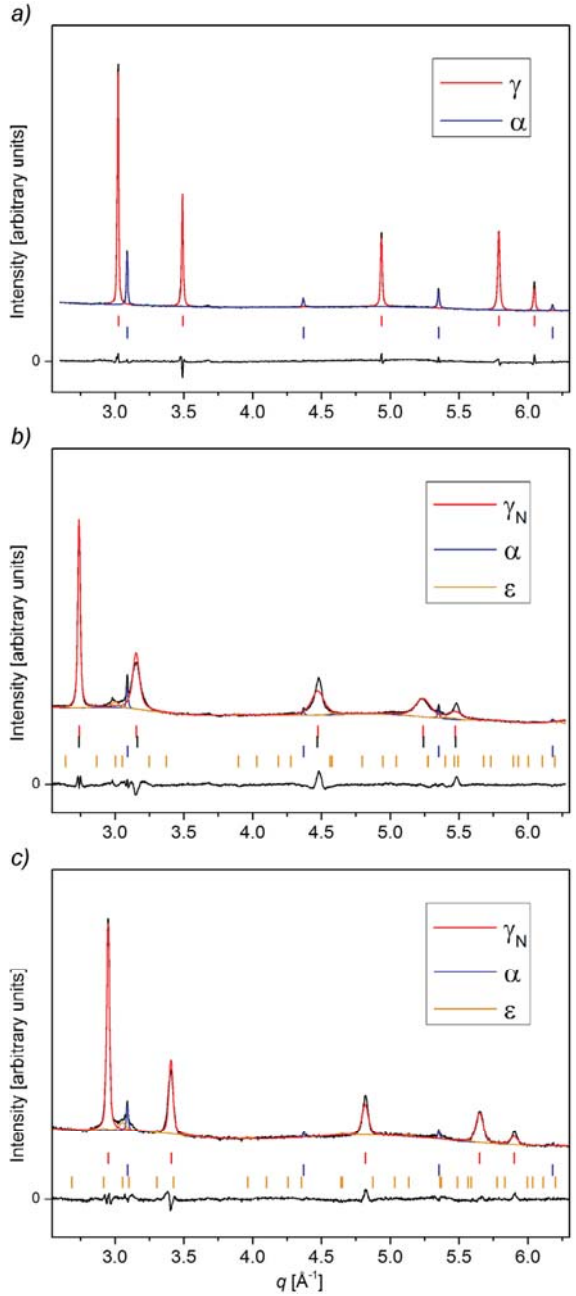

Figure 6.3: X-ray diffractogram, refined Rietveld profile and difference curve up to q = 6.3 Å^{-1} for *a*) the AISI 316 reference sample, *b*) the high-nitrogen sample and *c*) the low-nitrogen sample. Vertical lines mark Bragg positions. Black markers in *b*) indicate ideal unfaulted f.c.c. positions.

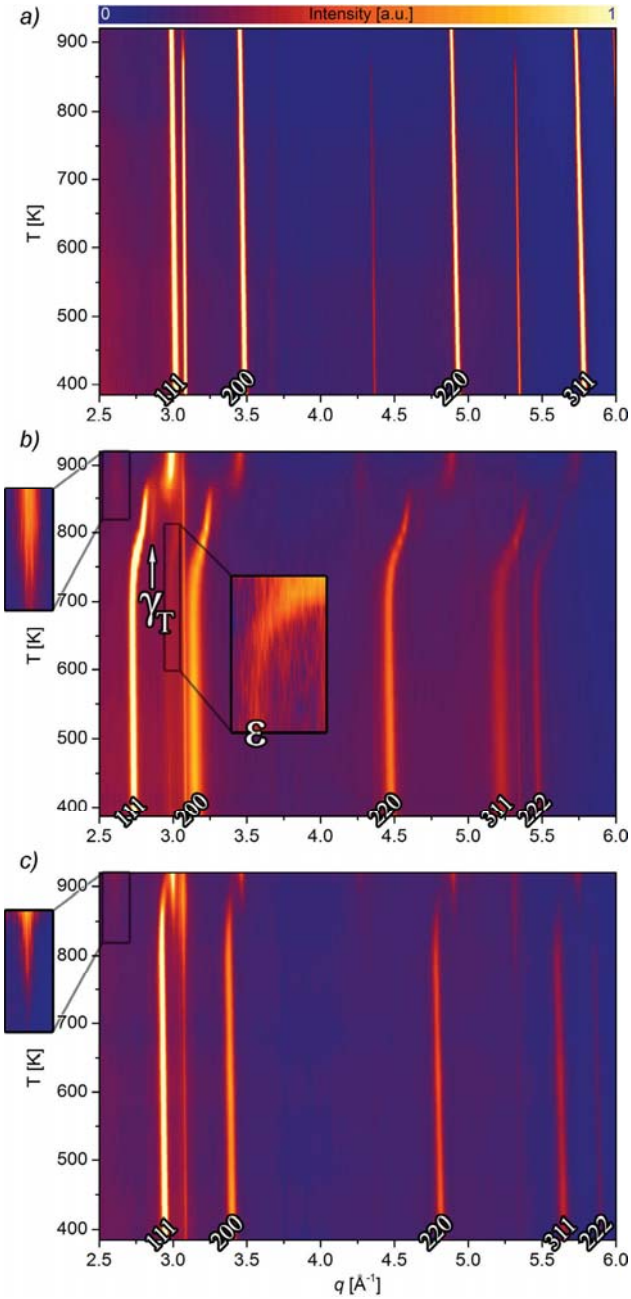

Figure 6.4: Contour plots of recorded diffraction profiles up to q = 6.0 Å^{-1} versus temperature for *a*) the AISI 316 reference sample, *b*) the high-nitrogen sample and *c*) the low-nitrogen sample. Indexed peaks are (expanded) austenite and the 111 peak of the γ_T phase is indicated with an arrow. Higher-order reflections are faint but visible. Intensity-rescaled inserts are added to emphasize the emerging 111 peak of CrN and the q shift of the ε 111 peak.

Initial experiments had shown that this phase could form on prolonged nitriding of fully austenitic foil pieces at 693 K. It is likely that the nucleation of the ε-phase is promoted by the large surface area on nitriding a fine powder.

Two major differences are noticed between the untreated and nitrided sample: Firstly, diffraction peaks for expanded austenite are considerably broadened and shifted towards lower q, and secondly, although the q shift is expected from the expansion of the crystal structure, peaks do not fit ideal f.c.c. positions. The broadening observed for expanded austenite is usually (at least) partially explained by an inhomogeneous nitrogen distribution in the nitrided sample (Christiansen & Somers, 2005). This effect should, however, be limited as 5 μm powder was used, and it is noted that no pronounced tailing of the line profiles towards high q is observed. This is in accordance with limited inhomogeneities in the nitrogen distribution, i.e. no concentration gradients. Therefore, broadening is interpreted as a consequence of the faulted structure of expanded austenite, which is also the origin of the *hkl*-dependent displacement of the diffraction peaks from their ideal f.c.c. positions. The peak positions can be described by including the stacking fault probability, α_{sf}, as a fit parameter. The systematic *hkl*-dependent deviations of XRD peaks from their ideal positions, as described by Warren (1969), were adopted for this purpose. The refinement profile does not entirely describe the observed broadening of γ_N diffraction peaks. Since these peaks are partly overlapping with peaks from α and ε-phases, and the contributions from screw dislocations and potential microstrain and size effects should also be taken into account, no further fitting of the broadening was attempted.

The low-nitrogen sample was denitrided in an H_2 atmosphere, which retracts loosely bound interstitial nitrogen. Correspondingly, in Figure 6.3(*c*) the shift of the diffraction peaks for expanded austenite to lower q is not as pronounced as in Figure 6.3(*b*). The broad peak attributed to ε-M_2N_{1-z} is slightly shifted towards higher q. This is an indication of a broad compositional range consistent with the nitride structure, because the shift corresponds to a reduction in nitrogen content. The ferrite phase is still present.

The interstitial nitrogen content of γ_N can be estimated from the lattice parameter, a, of expanded austenite using the reported relation between a and the interstitial nitrogen occupancy, y_N (Christiansen & Somers, 2006a). Since diffractograms were recorded starting from 385 K, it is necessary to use fitted coefficients of thermal expansion to obtain the values at room temperature. See Section 6.1.3 for a detailed discussion on how the lattice parameters evolve with temperature. For the high-nitrogen sample this yields an occupancy of $y_N = 0.56$, where y_N is the fraction of the interstitial sublattice occupied by nitrogen atoms, which, for f.c.c., is equivalent to the number of N atoms per metal atom. This corresponds to a nitrogen-to-chromium ratio (cf. Table 6.1) of 3.22, in excellent agreement with the previously reported maximum solubility in AISI 316 (Christiansen & Somers, 2006a).

The lattice parameter for the low-nitrogen sample is below the minimum value in the reported relation, and extrapolation is not feasible since the lattice parameter does not linearly approach that of the untreated steel. Another relation exists for low interstitial contents, as reported for carbon-expanded austenite (Hummelshøj *et al.*, 2010). Using this as an approximation yields y_N = 0.14, which is indeed lower than the previously reported minimum solubility. This is not surprising since the Cr content in the presently applied steel is lower than the one used by Christiansen & Somers (2006a), and the retained nitrogen is interpreted as trapped by Cr, which has the highest affinity for N of the elements present in the sample. The nitrogen-to-chromium ratio obtained is, however, also lower than anticipated: N:Cr = 0.804 as compared to the expected minimum N:Cr = 0.891. It appears that the minimum obtainable solubility of N in homogeneous samples of expanded austenite depends on the Cr content, but is not constrained to a fixed ratio. Alternatively, the lower obtained ratio may be explained by an initial formation of δ-ferrite on solidification of the original powder. This lowers the concentration of Cr in the austenite phase, thereby limiting the nitrogen content, and leads to an underestimated calculated nitrogen-to-chromium ratio.

6.1.2.1 In situ diffraction

Recorded diffraction profiles as a function of temperature are given as contour plots in Figure 6.4. Indexed peaks are those corresponding to (expanded) austenite (see Figure 6.3 for α and ε peak positions). For the untreated sample (Figure 6.4*a*), the ferrite phase transforms into austenite above 820 K, in good agreement with Thermo-Calc results of ferrite and austenite stability in AISI 316 (Kjeldsen, 2013). At the highest investigated temperature, 920 K, the sample contains 97.1(5) mass% austenite. As a consequence of thermal expansion of austenite and ferrite, a slight shift of the diffraction peaks towards lower q is observed with increasing temperature.

For the high-nitrogen sample the only evident change up to 700 K is thermal expansion. Above this temperature, a deflation of the lattice parameter of expanded austenite, as manifested by an increase in q for γ_N reflections, is caused by a decrease in interstitial content. Above 840 K, formation of an austenite phase with lattice parameters comparable to those of the untreated sample is visible. The release of nitrogen from expanded austenite causes a gradual decrease in the lattice parameters, but the transformation of γ_N to the final austenite phase, γ, is accompanied by a discontinuity. A transitional phase, γ_T, with an intermediate lattice parameter was observed, indicated by an arrow in Figure 6.4(*b*). The 111 peak of ε-M_2N_{1-z} shifts towards higher q in the same temperature range as expanded austenite and disappears beyond 900 K, indicating a nitrogen depletion of the ε-phase, in

accordance with the broad compositional range of this nitride. Formation of CrN from the decomposition of expanded austenite was detected above 750 K.

The first change in phase composition for the low-nitrogen sample is an increase in intensity of the ferrite peaks above 750 K (Figure 6.4*c*). Following this, the decomposition of expanded austenite becomes apparent from the decreasing lattice parameter. Note that, unlike the high-nitrogen sample, the change in composition of the γ_N phase is negligible up to almost 850 K. The 111 peak of ε-M_2N_{1-z} shifts slightly towards higher q beyond 750 K before disappearing at 840 K. The initial formation of CrN takes place at 800 K and γ peaks are observed at 840 K.

6.1.2.2 Phase transformations

Phase transformation maps showing the refined mass fractions are given in Figure 6.5. Formation of CrN from the decomposition of expanded austenite starts at 750 K and increases up to a final mass fraction of 18% at 920 K. The amount of ε-M_2N_{1-z} remains almost constant up to 900 K. The transitional phase, γ_T, constitutes a maximum mass fraction of 17% at 860 K before the amount decreases at higher temperatures. The initial total nitrogen content in the sample obtained from thermogravimetry during nitriding was 12 mass%, while the final mass fraction of CrN accounts for a total nitrogen content of 3.8 mass%. A significant amount of the dissolved nitrogen content has thus been released as N_2, in accordance with previously reported observations on annealing expanded austenite in an inert (N_2) atmosphere (Christiansen & Somers, 2006b).

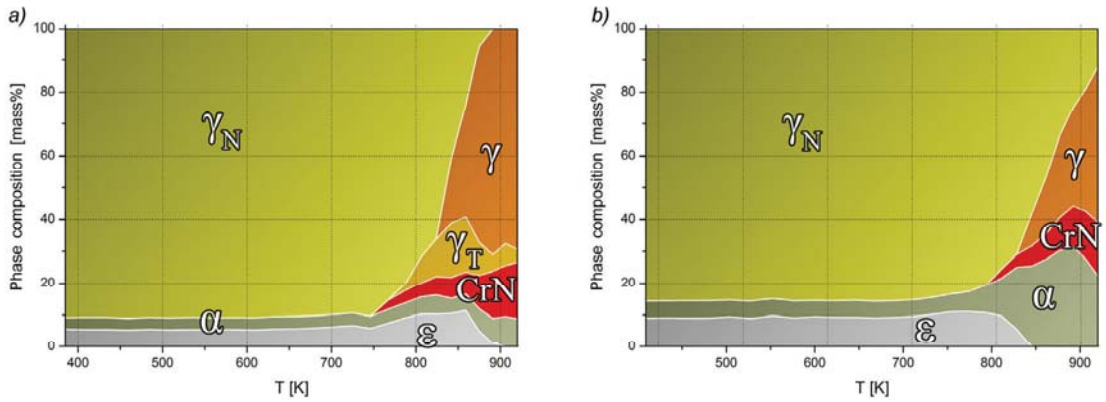

Figure 6.5: Phase transformation map for *a*) the high-nitrogen sample and *b*) the low-nitrogen sample. Estimated standard deviations from refinements are ≤ 1.8 mass%.

The first change in phase composition for the low-nitrogen sample (Figure 6.5*b*) occurs at 750 K, where the amount of ferrite increases at the cost of expanded austenite. This is interpreted as the first indication of the decomposition of expanded austenite and is directly followed by development of CrN. The decrease of the lattice parameters of γ_N at 840 K

coincides with decomposition of the ε-phase and the formation of an austenite phase with lattice parameter comparable to that of the untreated sample. The formation of ferrite from decomposition of γ_N at temperatures below 900 K is in agreement with Thermo-Calc results of ferrite and austenite stability in AISI 316 containing nitrogen (Christiansen & Somers, 2006b). Above 900 K, ferrite is transformed into austenite and the final decomposition products for both samples are austenite and CrN, in good agreement with the Thermo-Calc calculations. Ferrite formation was not observed in the high-nitrogen sample, most likely as a consequence of the abundant presence of austenite-stabilizing N.

6.1.3 Discussion

The lattice parameters obtained with Rietveld refinement for the (expanded) austenite phases in all samples as a function of temperature are presented in Figure 6.6. The lattice of austenite in the reference sample expands monotonically in the entire investigated temperature range. For expanded austenite, the lattice parameters start to decrease above a certain temperature. The relatively low temperature where this is observed in the high-nitrogen sample is ascribed to N_2 formation. The release of nitrogen from expanded austenite as N_2 has been demonstrated before (Christiansen & Somers, 2006b) and is an immediate consequence of thermodynamically stable N_2 compared with N in solid solution (Grabke, 1968b). For high nitrogen content, the driving force for N_2 release is higher than for low nitrogen content. For the low-nitrogen sample, the decreasing lattice parameter is caused only by CrN formation. The final mass fraction of CrN accounts for a total nitrogen content of 3.5 mass%, which is the amount that was retained after denitriding. Note that the observed stability range up to about 800 K for the low-nitrogen sample is only valid for the thermal history of the sample, i.e. approximately eight minutes in between measurements, and does not represent completed transformation at the various temperatures. For prolonged (isothermal) annealing, decomposition of nitrogen-expanded austenite has been reported for temperatures as low as 600 K (Li *et al.*, 1999; Öztürk & Williamson, 2002; García Molleja *et al.*, 2013).

The observation of a transitional f.c.c. phase with a value of $a \simeq 3.8$ Å in the range 770 – 860 K has not been reported before on the basis of X-ray diffraction. The lattice parameter value coincides with that of the ordered iron-based nitride γ′-Fe_4N with stoichiometric composition (Somers *et al.*, 1989b), which matches the dependence of the lattice parameter of expanded austenite on nitrogen content (Christiansen & Somers, 2006b). The presence of a γ′-Fe_4N type structure has been reported on the basis of transmission electron microscopy observations of superlattice reflections, but with a reported lattice parameter larger than that of γ′-Fe_4N (Xu *et al.*, 2000; Xiaolei *et al.*, 2005; Stróz & Psoda, 2010). The present result suggests that the composition M_4N with $y_N = 0.25$ can indeed occur and may be

thermodynamically favored over expanded austenite with short range order of nitrogen atoms.

Initially, expanded austenite in the high-nitrogen sample has a significantly larger lattice parameter than that of the low-nitrogen sample. For both samples, the lattice parameter of the developed γ phase approaches that of the reference sample after decomposition, implying that the austenite present in the samples at 900 K is essentially free of nitrogen in solid solution.

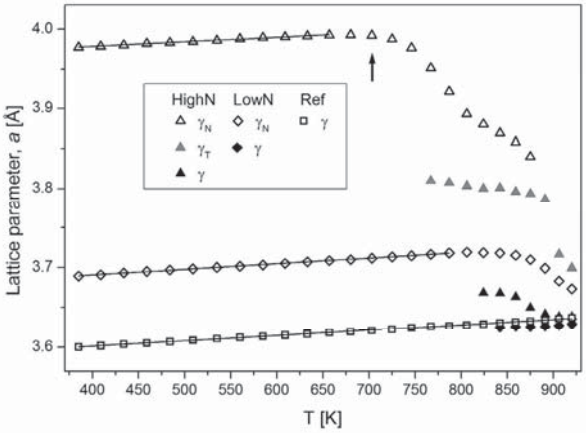

Figure 6.6: Lattice parameters for (expanded) austenite phases in all samples. Estimated standard deviations are ≤ 10^{-3} Å. The symbols in the legend are grouped by sample designation. Lines correspond to fitted expressions for thermal expansion (equation 4.1). The start of N_2 formation is marked by an arrow.

Slightly lower lattice parameter values were obtained for the low-nitrogen sample, as compared to the high-nitrogen sample. A slight reduction in lattice parameter is expected because of chromium depletion of the austenitic matrix (Babu *et al.*, 2005) due to formation of CrN. It is noted that the transition from expanded austenite to nitrogen-free austenite is not associated with a gradual continuous decrease of the lattice parameter (or nitrogen content), but that a temperature range exists where both high- and low-nitrogen-containing austenite are present in the same sample. This observation can be related to the mechanism of the transformation, which is consistent with discontinuous precipitation, as previously demonstrated (Christiansen & Somers, 2006b). For the low-nitrogen containing sample, the decomposition at a lower temperature showed the development of ferrite (presumably) during a eutectoid transformation. Ferrite formation is observed before CrN, which may be explained by coherent diffraction of small CrN particles with ferrite. Nitrogen-lean austenite developed at a higher temperature. Apparently, at temperatures well below the stabilization temperature for austenite, ferrite can develop, most likely promoted by a favorable Baker–Nutting orientation relationship between CrN and ferrite (Somers *et al.*,

1989a). Evidently, at higher temperatures, a favorable interfacial energy between CrN and the matrix is insufficient to promote ferrite formation, and austenite develops instead. It is hypothesized that the transformation of ε-M_2N_{1-z} to ferrite is, in principle, also possible. At high pressures, b.c.c. iron transforms into h.c.p. ε-Fe (Bundy, 1965). The presence of a high amount of nitrogen in the metallic lattice, and the formation of ε-M_2N_{1-z}, could be conceived as consequence of a 'high internal pressure' associated with nitrogen dissolution. The removal of interstitial nitrogen ('internal pressure') from ε-M_2N_{1-z} might induce the formation of ferrite.

6.1.3.1 Coefficients of thermal expansion

The commonly used mean (linear) thermal expansion coefficient, α_{exp}, was fitted to equation (4.1). The volumetric coefficient of thermal expansion was found by replacing the lattice parameter with the volume of the unit cell in the expression (for isotropic materials the volumetric thermal expansion coefficient is three times the linear coefficient). Note that, although expansion in the investigated range is approximately linear, expansion coefficients are not, in general, independent of temperature. The number of data points in the investigated range did not allow statistically reliable fits of the temperature dependence (see Appendix A.1). The resulting fits of equation (4.1) are shown in Figure 6.6 and all values obtained are presented in Table 6.2.

Table 6.2: Fitted coefficients of volumetric (V) and linear (a) thermal expansion for (expanded) austenite phases as defined by equation (4.1). The value for γ'-Fe_4N (Somers *et al.*, 1989b) is included for comparison, the volumetric coefficient calculated as the reported linear coefficient multiplied by three.

Phase	T range [K]	α_{exp} [$\times 10^{-5}$ K^{-1}]	
γ_N (high)	385 – 657	V	4.32 (5)
		a	1.43 (2)
γ_N (low)	385 – 787	V	5.71 (2)
		a	1.891 (8)
γ (reference)	385 – 920	V	5.60 (2)
		a	1.851 (7)
γ'-Fe_4N	293 – 773	V	2.28 (24)
		a	0.76 (8)

The sample with low nitrogen content exhibits larger thermal expansion than the untreated reference material, while the sample with the high nitrogen content has an expansion coefficient significantly lower than that of the other samples. This is explained by the underlying cause of the expansion, i.e. thermal vibrations of composing atoms. The additional vibrations of the interstitial nitrogen atoms cause an added separation of the

metal atoms with increasing thermal energy. The additional nitrogen vibrations are less significant for higher interstitial content where the average distance between the metal atoms is larger. In fact, the high-nitrogen sample exhibits the lowest thermal expansion owing to the large intermetallic distances, but the value is still almost twice that reported for γ'-Fe_4N (Somers *et al.*, 1989b). No expansion coefficient could be determined for the M_4N phase that develops beyond 770 K. For reference, the linear expansion coefficient obtained for the ferrite phase is $1.131\ (5) \times 10^{-5}\ K^{-1}$.

It is noted that the observation of a dependence of the thermal expansion coefficient on the nitrogen content has implications for the development of residual stress in expanded austenite zones developing on stainless steel. Residual stresses in expanded austenite are highly compressive and generally largely composition induced (Christiansen & Somers, 2009). A variation in thermal expansion coefficient over the thickness of the γ_N zone implies that during cooling, an additional thermally induced stress profile develops, such that thermal stress is largest for the highest nitrogen content. The presently established difference in thermal expansion coefficient for high- and low-nitrogen-containing expanded austenite corresponds to an additional compressive stress of approximately 500 MPa in high-nitrogen expanded austenite. This calculation assumes that values of Young's modulus and Poisson's ratio for AISI 316 austenitic stainless steel (Ledbetter, 1981) are comparable to those of expanded austenite. These values may, however, change with interstitial content (Tromas *et al.*, 2012; Balijepalli *et al.*, 2013).

6.1.3.2 Stacking fault probability

Warren's model for describing the effect of stacking faults on X-ray diffraction profiles can readily be implemented in the Rietveld refinements, in order to describe the systematic deviations in the positions of diffraction peaks for expanded austenite (Figure 6.3*b*). The inadequacies of the model should not be ignored, but even a rigorous treatment of the effects of stacking faults is insufficient to completely describe the structure, e.g. the different metallic environments observed with EXAFS (Oddershede *et al.*, 2008b, 2010). The stacking fault probability obtained with Rietveld refinement of each of the X-ray diffractograms for the high-nitrogen sample is shown in Figure 6.7 and remains approximately unaltered for temperatures up to 680 K. The presently obtained values for the stacking fault probability ($\alpha_{sf} \simeq 0.03$) are in accordance with those previously obtained for homogeneous expanded austenite samples (Christiansen & Somers, 2004). A sudden decline of the stacking fault probability was observed above 680 K, resulting in no observable induced peak shift above 750 K, where CrN development was first noticeable.

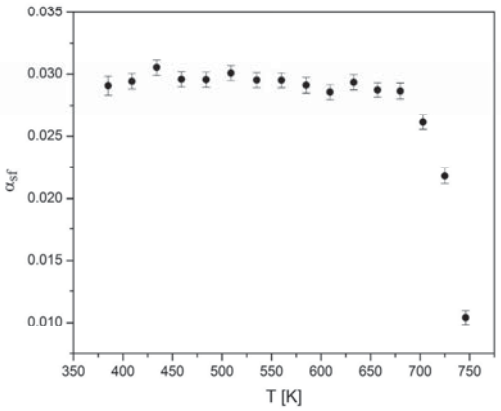

Figure 6.7: Refined stacking fault probability for expanded austenite versus temperature for the high-nitrogen sample. For the low-nitrogen sample the stacking fault probability is zero.

Several hypotheses can be put forward to explain the observed decrease of the stacking fault probability. Firstly, a decrease of the nitrogen content in solid solution by N_2 formation could induce a reduction of the stacking fault density. Secondly, the segregation of N atoms (or CrN development) onto stacking faults, leading to clusters, causes the stacking faults to lose their identity. For the two investigated samples it seems that the stacking fault probability is related to the nitrogen content in solid solution. The stacking fault probability decreases with decreasing interstitial content for the high-nitrogen sample. For the low-nitrogen sample, with substantially lower interstitial content, no stacking-fault-induced peak shifts were observed in the diffractograms. The stacking fault probability is thus negligible for very low nitrogen contents.

6.2 Transitional phase and intermediate nitrogen content

There are two possible interpretations on the nature of the observed transitional phase, γ_T, on thermal decomposition of nitrogen expanded austenite. One is chromium depletion of the stainless steel matrix due to precipitation of CrN. This causes iron (and nickel) rich regions, which results in the formation of $(Fe,Ni)_4N$, analogous to γ'-Fe_4N. Since the compositional range of expanded austenite includes the occupation of one quarter of octahedral sites, another possibility is that the composition M_4N (M = Fe, Cr, Ni) is particularly stable. If that is the case, formation of the transitional phase does not necessarily involve precipitation of CrN and for a composition $y_N = 0.25$, expanded austenite should be stable at higher temperatures compared to fully nitrided samples. To elucidate on this subject two additional samples of nitrogen expanded austenite were produced from thin stainless steel foils. The foils were fully austenitized in order to avoid the presence of ferrite or martensite.

6.2.1 Experimental

Thin foils of AISI 316 stainless steel of nominal composition (by mass) 18% Cr, 10% Ni and 3% Mo (Goodfellow Cambridge Ltd.) with thickness 12.5 μm were used for nitriding. Prior to treatment, recrystallization and austenitization was achieved by heating to 1323 K in pure H_2 followed by immediate cooling to room temperature. Gaseous nitriding of the foil pieces was performed in a LAC PKRC55/09 furnace retrofitted for nitriding with ammonia and hydrogen gasses of 99.999% purity.

A fully nitrided sample was synthesized in an atmosphere of 100 vol.% NH_3 (infinite nitriding potential) at 693 K for 48 hours with a NH_3 flow rate of 1 L/min. A sample with intermediate nitrogen content was produced from the fully nitrided sample by denitriding at 693 K for 6 hours in a gas consisting of 80 vol.% H_2 and 20 vol.% NH_3 with a total flow of 2.5 L/min. This gas composition corresponds to a nitriding potential, $K_N = 0.280$ atm$^{-1/2}$. The nitrided foils were powdered with ultra-sound while submerged in ethanol and dried in air. As internal standard, W powder (99.95% purity, Goodfellow Cambridge Ltd.) was added.

Details for *in situ* synchrotron X-ray diffraction and Rietveld refinements correspond to those given in Section 6.1.1, unless otherwise stated. Temperature calibration and determination of the applied wavelength (λ = 0.99471(2) Å) were performed using the internal W standard.

The fully nitrided sample was immediately heated to 921 K and kept at this temperature. For the sample of intermediate nitrogen content, 28 diffractograms were measured in the temperature range 341 – 890 K. Data were collected in a 2θ range of 4 – 100° (corresponding to a q range from 0.4 to 9.7 A^{-1}) with a fixed step size of 0.005° in 2θ and

an exposure time of 240 seconds at each temperature step. After exposure, the temperature was immediately ramped to the next set point, and the average time for reaching and stabilizing at each set point temperature, prior to exposure, was 233 seconds.

Due to the presence of additional peaks from the furnace setup (not from the sample), some regions were excluded in the Rietveld refinements (see Figure 6.9*a*). For all Rietveld refinements, residual values of $R_p \leq 1.11\%$ and goodness-of-fit values $\chi^2 \leq 2.37$ were obtained.

6.2.2 Isothermal annealing

The nitrogen content of the fully nitrided sample corresponds to $y_N = 0.42$, as calculated from the lattice parameter (Christiansen & Somers, 2006a). This content is below that of the high-nitrogen sample synthesized from powder, indicating that the high available surface area of the powder increases the nitriding rate. On heating to 921 K, immediate decomposition of expanded austenite is observed accompanied by formation of both the transitional phase and CrN (Figure 6.8).

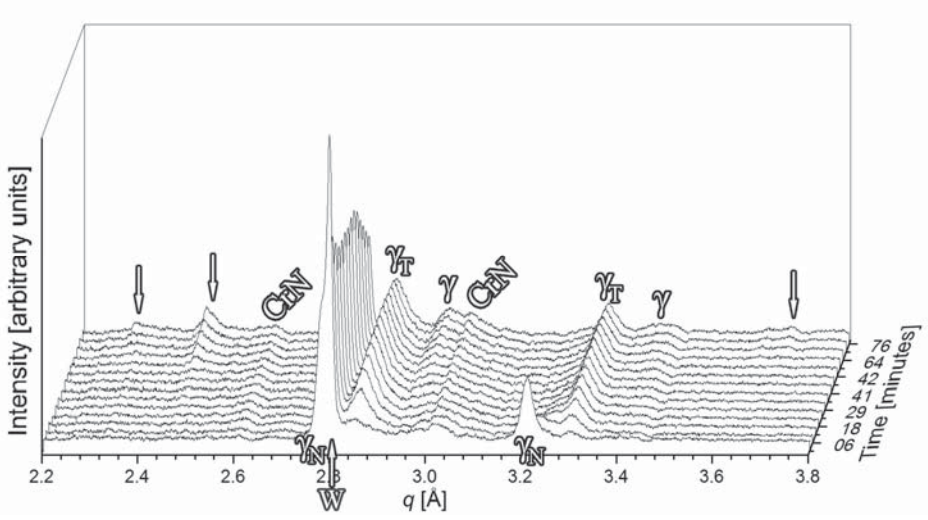

Figure 6.8: Diffractograms of isothermal annealing at 921 K of nitrogen expanded austenite with W internal standard. Arrows mark emerging oxide (primarily hematite) peaks.

The simultaneous formation of both CrN and the transitional phase seems to favor the description involving chromium depletion of the stainless steel matrix with the resulting transitional phase being $(Fe,Ni)_4N$. At 921 K both phases are observed already in the first time-step. Therefore the potential formation of the transitional phase at lower temperatures, without precipitation of CrN, cannot be dismissed conclusively. Due to leaks in the capillary, additional peaks from metal oxides, primarily hematite (Fe_2O_3), appear beyond approximately 40 minutes.

6.2.3 Intermediate nitrogen content

The sample synthesized with intermediate content contains nitrogen corresponding to occupation of one third of the octahedral interstitial positions (y_N = 0.33). This is in good agreement with the reported relation between nitriding potential (nitrogen activity) and interstitial content (Christiansen & Somers, 2006a) and is not far above that corresponding to the composition M_4N (y_N = 0.25). Recorded diffraction profiles for the temperature series and phase transformation map is given in Figure 6.9. In contrast to the high-nitrogen sample synthesized from powder, thermal decomposition proceeds without formation of a transitional phase and produces only nitrogen lean austenite and CrN.

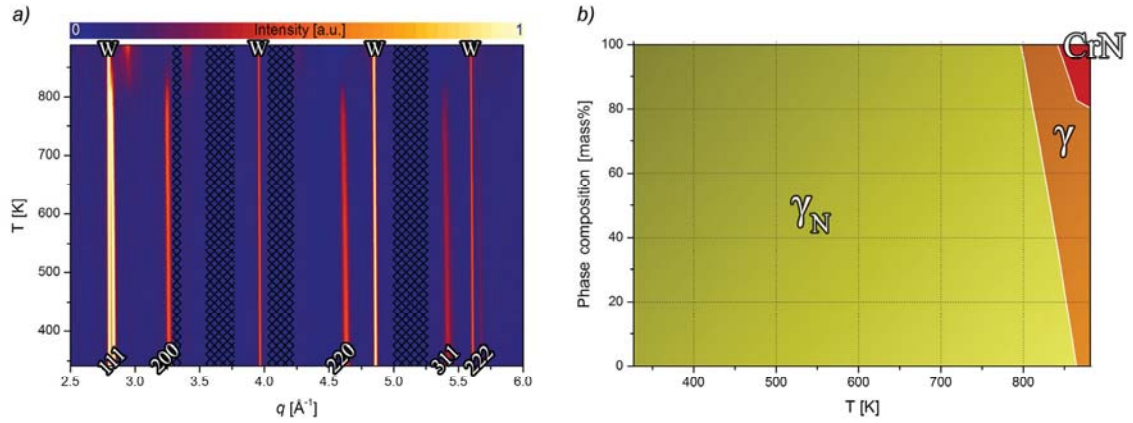

Figure 6.9: Expanded austenite with W internal standard; *a*) contour plots of recorded diffraction profiles versus temperature up to q = 6.0 Å^{-1} (indexed peaks are expanded austenite) and *b*) phase transformation map (W fraction excluded). Estimated standard deviations from refinements are ≤ 1.0 mass%. Regions excluded in the refinement due to peaks not originating from the sample are marked as hatched in *a*) and a conservative background removal has been applied to eliminate the diffuse scattering from the capillary at low q.

The lattice parameter is initially above that corresponding to M_4N ($a \simeq 3.8$ Å) and increases further with temperature due to thermal expansion (Figure 6.10*a*). For the composition y_N = 0.33, expanded austenite is stable up to around 800 K similar to the low-nitrogen sample synthesized from powder, thus exceeding the stability range for high nitrogen contents. Above this temperature, the lattice parameter decreases due to decreasing nitrogen content and an austenite phase with considerably lower lattice parameter (interstitial content) is formed. The stacking fault probability is $\alpha_{sf} \simeq 0.04$ and declines drastically above 700 K (Figure 6.10*b*). In the final stages of decomposition, expanded austenite is characterized by broad low-intensity peaks coinciding with peaks from the internal standard. This necessitated manual fitting of the lattice parameter and stacking fault probability for the data at 841 K. Hence no estimated standard deviation is given for the stacking fault probability at this temperature.

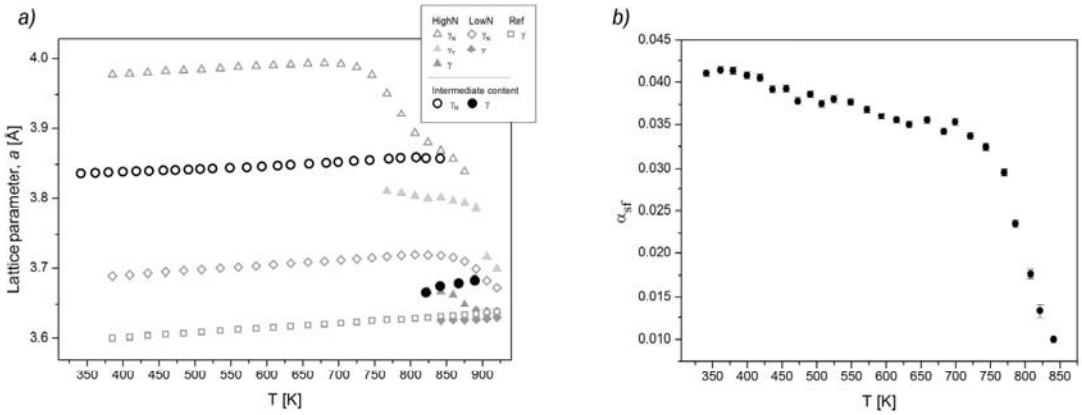

Figure 6.10: *a*) Lattice parameters for expanded austenite of intermediate nitrogen content compared to the values obtained for samples synthesized from powder (faded), cf. Figure 6.6. The symbols in the legend are grouped by sample designation. Estimated standard deviations are ≤ 10^{-3} Å. *b*) Refined stacking fault probability versus temperature.

In contrast to the other samples, the thermal expansion is not linear in the entire investigated temperature range. The expansion coefficient could be fitted including a temperature-dependence but seems to be well described by two distinct linear regions (Figure 6.11). The values of the fitted expansion coefficients are given in Table 6.3. In the low-temperature range, 341 – 549 K, the expansion coefficient is much lower than for other nitrogen contents and for the parent austenitic stainless steel, and consequently closer to that of γ′-Fe_4N, cf. Table 6.2. In the high temperature range the expansion is similar to, but slightly higher, than what is observed for high nitrogen contents.

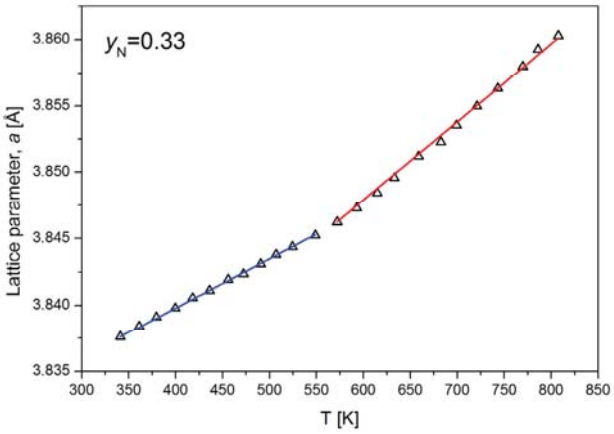

Figure 6.11: Lattice parameters versus temperature for expanded austenite (y_N = 0.33) and corresponding fits of the two distinct linear regions.

Table 6.3: Fitted coefficients of volumetric (V) and linear (a) thermal expansion for the two distinct linear regions of expanded austenite with intermediate nitrogen content as defined by equation (4.1).

Phase	T range [K]	α_{exp} [$\times 10^{-5}$ K^{-1}]	
γ_N (y_N = 0.33)	341 – 549	V	2.90 (1)
		a	0.966 (4)
γ_N (y_N = 0.33)	572 – 808	V	4.61 (4)
		a	1.53 (1)

6.2.4 Discussion

The low expansion coefficient for nitrogen expanded austenite on approaching the composition M_4N, suggests similarities to the structure of γ'-Fe_4N. For a nitrogen content corresponding to $y_N = 0.25$ it is conceivable that an even lower expansion coefficient would be obtained. Long range order may thus exist between nitrogen atoms in expanded austenite, at least for certain compositions. If the similarities between expanded austenite and γ'-Fe_4N include magnetic properties, the observed change in thermal expansion can be explained by a ferromagnetic to paramagnetic transition. The observed transition temperature of around 550 K is, however, substantially lower than the Curie temperature of γ'-Fe_4N, $T_C \simeq 767$ K, and no such transition was observed for the high nitrogen sample. Results of the investigation of magnetic properties of expanded austenite are given in Section 6.4.

The stacking fault probability of $\alpha_{sf} \simeq 0.04$ for intermediate nitrogen content is higher than what was observed for the high-nitrogen sample. Thus, when expanded austenite is formed, the stacking fault probability does not necessarily depend on the nitrogen content. During thermal decomposition, however, the stacking fault probability does decrease with interstitial content and is accompanied by precipitation of CrN. The slight decline in refined stacking fault probability already above 400 K is not readily explained and may instead indicate a problem in the structural model. The description of peak shifts caused solely by stacking faults as described by Warren is indeed problematic and this subject is extensively treated in Chapter 7.

It can be argued that the difference in stability range, thermal expansion and decomposition between the sample with $y_N = 0.33$ and samples with high and low nitrogen content could be affected by the presence of ferrite in the latter two, which were not annealed prior to nitriding. Such an effect must, however, be limited as compared to the variation caused by the difference in nitrogen content, as large differences were observed for both samples containing ferrite.

6.3 Carbon expanded austenite

For the investigation of carbon expanded austenite, γ_C, three samples were produced from the 5 μm AISI 316 grade stainless steel powder described in Section 6.1 with one sample containing both nitrogen and carbon.

6.3.1 Experimental

Gaseous treatments were performed in a Netzsch STA 449 C Jupiter thermal analyzer with samples in ceramic crucibles. Ammonia, nitrogen and hydrogen gasses of 99.999%, propene of 99.5% and acetylene of 99.6% purity were applied. For all treatments a flow of nitrogen was led through the measurement compartment of the thermobalance to protect this part from reaction with the other gases.

The sample containing both nitrogen and carbon was synthesized at 693 K by nitriding in an atmosphere of 95 vol.% NH_3 and 5 vol.% N_2 (infinite nitriding potential) followed by denitriding in 91 vol.% H_2 and 9 vol.% N_2 (nitriding potential of zero) and carburizing in a gas consisting of 84 vol.% H_2 , 8 vol.% C_3H_6 and 8 vol.% N_2. The final gas composition corresponds to a carburizing potential, K_C = 0.519 $atm^{-2/3}$ (equation 2.9). The initial treatment is thus similar to that of the low-nitrogen sample described in Section 6.1 followed by carburizing until a stationary weight was reached (Figure 6.12).

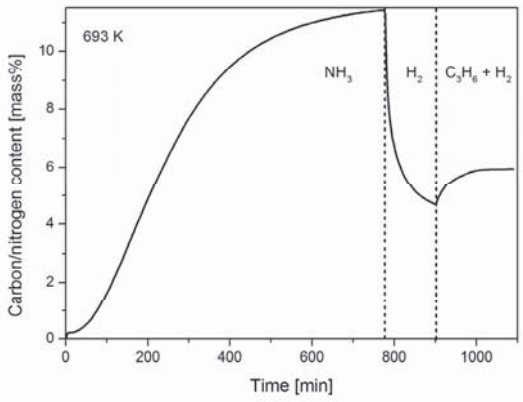

Figure 6.12: Thermogravimetric curve for expanded austenite containing both nitrogen and carbon synthesized at 693 K in three steps; nitriding, denitriding and carburizing. The gas constituents are listed in the figure (excluding for the constant protective flow of nitrogen).

The two samples containing only carbon were synthesized in an atmosphere of 88 vol.% H_2, 3 vol.% C_2H_2 and 9 vol.% N_2 corresponding to a carburizing potential of K_C = 0.182. The first sample (Figure 6.13*a*) was treated at 713 K for 3 hours while the temperature program for the second sample (Figure 6.13*b*) consisted of two steps; 693 K for 4 hours followed by 653 K

for 16 hours, resulting in a higher carbon content. Note that, unlike nitriding in ammonia/hydrogen gas mixtures, the use of unsaturated hydrocarbon gas and hydrogen at elevated temperatures removes or transforms the passive oxide layer. This enables direct carburizing without dedicated surface activation (Christiansen *et al.*, 2011).

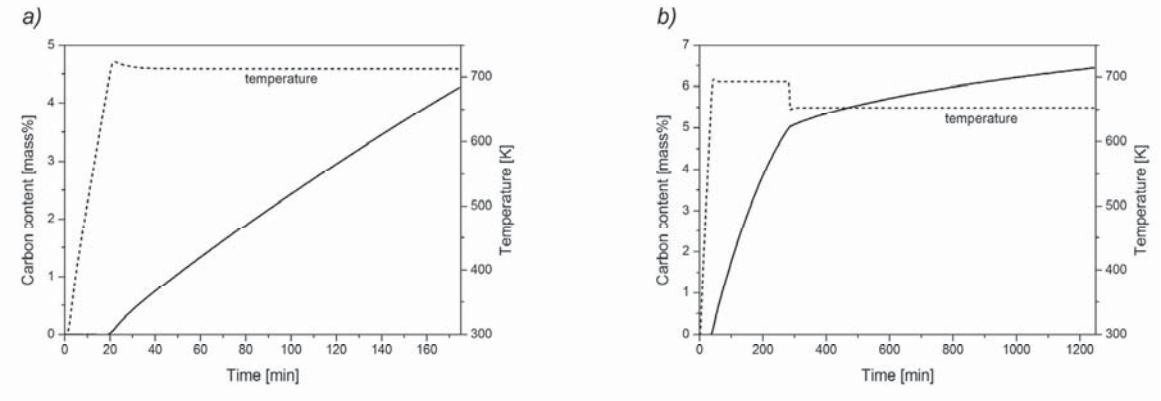

Figure 6.13: Thermogravimetric curves for *a*) expanded austenite with low carbon content synthesized at 713 K and *b*) high carbon content synthesized with a two-step temperature program; 693 K followed by 653 K. The carburizing potential was $K_C = 0.182$ for both samples but with a much longer treatment time for the high-carbon sample (and slightly different carbon activity due to the lower temperature).

Details for *in situ* synchrotron X-ray diffraction and Rietveld refinements correspond to those given in Section 6.1.1, unless otherwise stated. Data were collected in a 2θ range of 4 – 100° with a fixed step size of 0.005° in 2θ and a wavelength of $\lambda = 1.001952(5)$ Å for the low-carbon sample and $\lambda = 1.07051(2)$ Å for the high-carbon sample and the sample containing both nitrogen and carbon (corresponding to q ranges of 0.4 to 9.6 A^{-1} and 0.4 to 9.0 A^{-1}, respectively).

For the low-carbon sample, 21 diffractograms were measured in the temperature range 413 – 890 K with an exposure time of 240 seconds at each temperature step. After exposure, the temperature was immediately ramped to the next set point, and the average time for reaching and stabilizing at each set point temperature prior to exposure was 177 seconds. For the sample containing both nitrogen and carbon and the high-carbon sample, 26 diffractograms were measured in the temperature range 385 – 920 K with stabilization times of 242 and 205 seconds, respectively. For all Rietveld refinements residual values of $R_p \leq 1.85\%$ and goodness-of-fit values $\chi^2 \leq 1.44$ were obtained.

6.3.2 Results and interpretation

The sample containing both carbon and nitrogen was obtained by nitriding and denitriding followed by carburizing of AISI 316 powder until a stationary weight gain was reached. The combined nitrogen and carbon content amounted to 5.9 mass%, but carbon may have partially replaced nitrogen during carburizing. It is therefore not possible to quantify the individual contributions from the thermogravimetric curve (Figure 6.12). The main constituent in the resulting powder is expanded austenite as seen in the diffractogram on Figure 6.14(*a*). Similar to the nitrided samples, ferrite is present as well as an additional broad peak between the 111 and 200 reflections of expanded austenite, which is attributed to the presence of h.c.p. based ε-(carbo)nitride. Compared to the low-nitrogen sample (Figure 6.3*c*), diffraction peaks for γ_{CN} are shifted to lower q due to additional interstitial occupancy by carbon, which expands the lattice. For the expanded austenite phase the combined nitrogen and carbon content is estimated from the relation between lattice parameter and the nitrogen occupancy, y_N, (Christiansen & Somers, 2006a) and the carbon occupancy, y_C, (Hummelshøj *et al.*, 2010), which yields and average value of y_{CN} = 0.24. Diffraction peaks for expanded austenite are broadened compared to the reference sample (Figure 6.3*a*), but no stacking fault induced peak shifts are observed. During heating a number of oxide peaks emerge beyond 660 K caused by a leaked capillary (Figure 6.15*a*).

Rietveld refinement of diffraction data for the low-carbon sample necessitated exclusion of a region containing an additional peak originating from misaligned Soller slits (Figure 6.14*b*). The powder consists of ferrite, austenite, carbon expanded austenite (y_C = 0.18) and Hägg carbide, χ-M_5C_2. The asymmetric broad peaks of austenite and expanded austenite are caused by an inhomogeneous distribution of carbon, i.e. a concentration gradient. The gradient is fitted as two separate phases, γ_{I1} and γ_{I2}, with intermediate lattice parameters (carbon content). Although this is not a physically valid representation it allows a sufficient description of the observed diffraction profile. The inhomogeneous carbon distribution is expected from the thermogravimetric curve in Figure 6.13(*a*) since carburizing was not continued until a stationary weight was reached. Longer treatment time may further promote the formation of carbides. This is indeed the case for the high-carbon sample, for which the carburizing treatment was continued for 20 hours. In addition to ferrite and carbon expanded austenite (y_C = 0.22), this sample contains a substantial amount of Hägg carbide, χ-M_5C_2 (Figure 6.14*c*). In correspondence with the longer treatment time and the significantly less steep thermogravimetric curve in Figure 6.13(*b*) the distinct asymmetry of the low-carbon sample is not observed. Austenite is, however, still present as broadened peaks with a slight shift to lower q. For both samples of carbon expanded austenite no stacking fault induced peak shifts were observed.

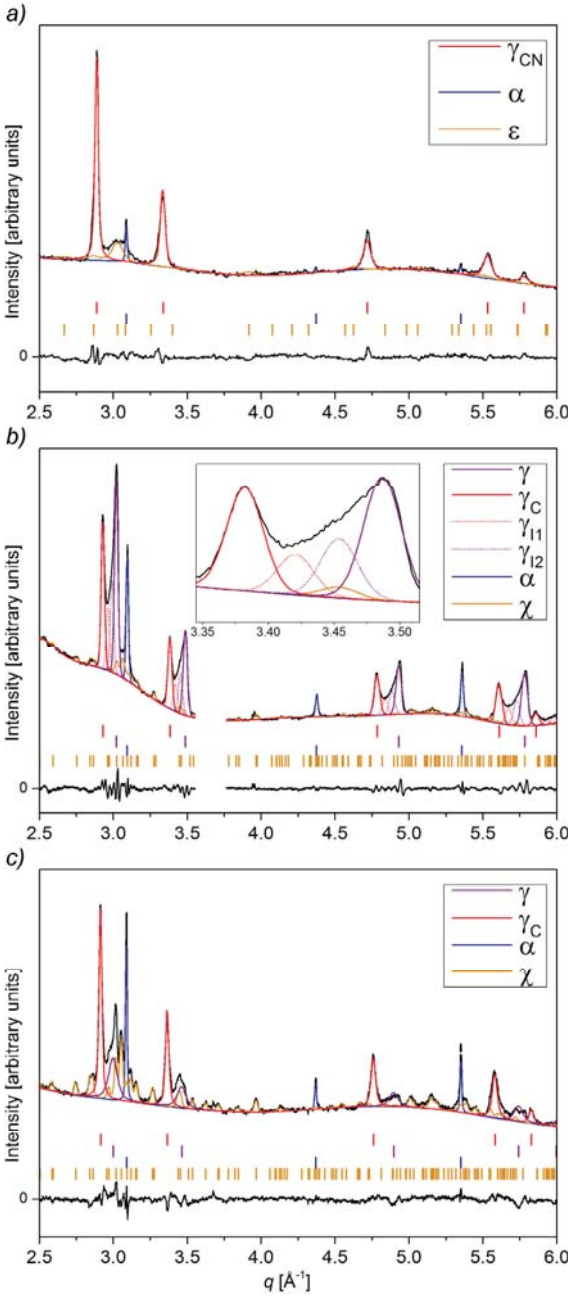

Figure 6.14: X-ray diffractogram, refined Rietveld profile and difference curve up to q = 6.0 Å^{-1} for *a*) the sample containing both carbon and nitrogen, *b*) the low-carbon sample with excluded region due to a peak from misaligned Soller slits and *c*) the high-carbon sample. Vertical lines mark Bragg positions.

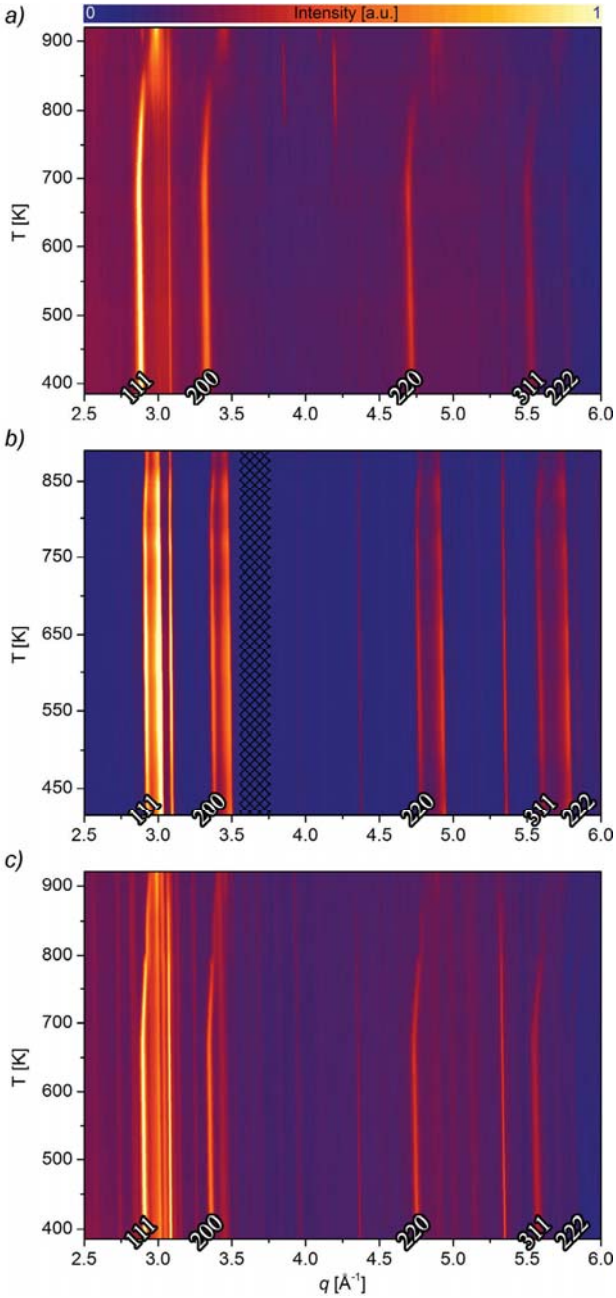

Figure 6.15: Contour plots of recorded diffraction profiles up to q = 6.0 Å^{-1} versus temperature for *a*) the C/N sample, *b*) the low-C sample and *c*) the high-C sample. Indexed peaks are expanded austenite. Peaks emerging beyond 660 K in *a*) correspond to oxides (cf. Figure 6.16*a*). In *b*) a conservative background removal has been applied to eliminate the diffuse scattering from the capillary at low q and the excluded region is marked as hatched. Intensities have been rescaled to account for beam decay in *c*).

6.3.2.1 Phase transformations and thermal expansion

Phase transformation maps showing the refined mass fractions versus temperature are given in Figure 6.16(*a-c*). The initial amount of ε-phase in the sample containing both nitrogen and carbon exceeds that of the nitrided samples (Figure 6.5), which suggests that the addition of carbon further stabilizes the ε-nitride. During heating the only evident change up to 660 K is thermal expansion.

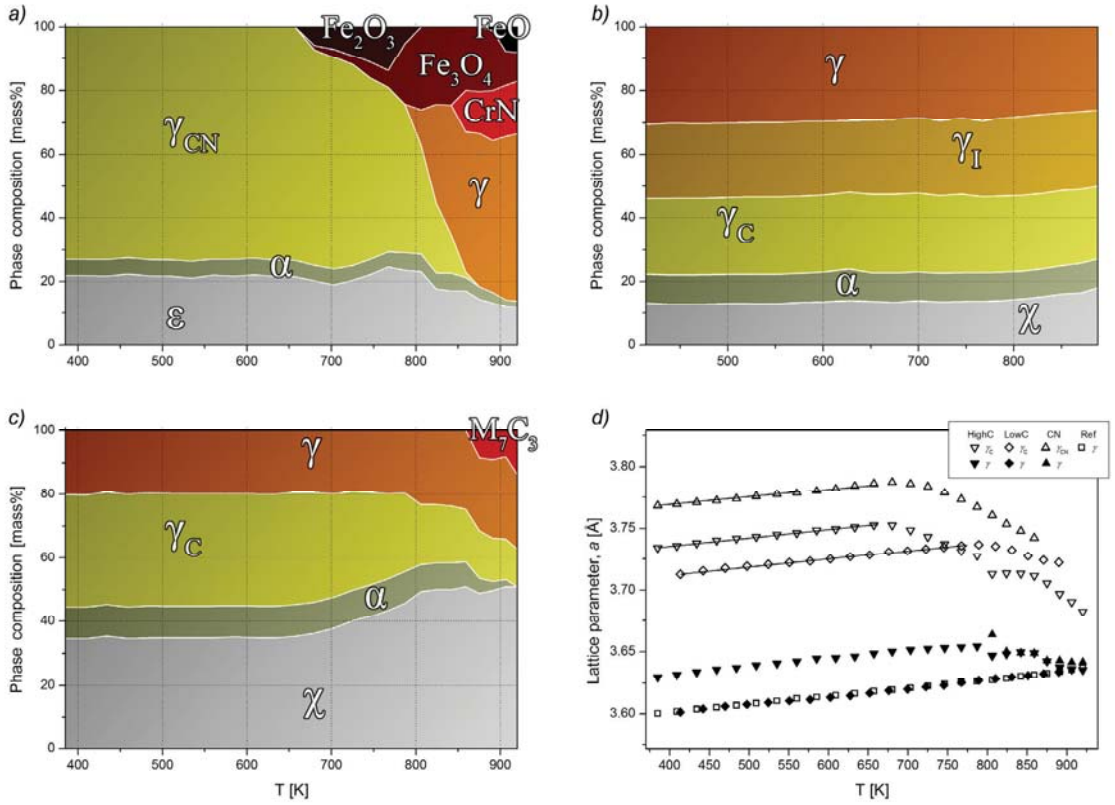

Figure 6.16: Phase transformation map for *a*) the sample containing nitrogen and carbon, *b*) the low-carbon sample, *c*) the high-carbon sample and *d*) lattice parameters for (expanded) austenite phases in all carburized samples plus the untreated AISI 316 powder (Section 6.1). Lines in *d*) correspond to fitted expressions for thermal expansion (equation 4.1) and symbols in the legend are grouped by sample designation. Estimated standard deviations from refinements are ≤ 1.5 mass% for phase fractions and ≤ 10^{-3} Å for lattice parameters.

The initial decomposition of expanded austenite coincides with the unintentional oxidation of the sample, resulting in formation of the iron-based oxides hematite (Fe_2O_3), magnetite (Fe_3O_4) and, beyond 890 K, wüstite (FeO). Similar to the ε-nitride and χ-carbide, iron may have been partially replaced by other metallic elements in the steel (Cr, Ni, Mo). The final decomposition products are austenite and CrN.

The combined mass fraction of the two separate phases with intermediate lattice parameters included to describe the concentration gradient for the low-carbon sample is denoted γ_I in Figure 6.16(*b*). Initial decomposition of carbon expanded austenite, as indicated by a decreasing lattice parameter, occurs above 770 K and is accompanied by additional formation of χ-M_5C_2. No other changes are observed in the investigated temperature range (the experiment was ended prematurely due to loss of beam intensity). For the high-carbon sample (Figure 6.16*c*), expanded austenite decomposes above 660 K and additional Hägg carbide is formed. M_7C_3 carbide is formed above 875 K and ferrite peaks disappear at 920 K.

The lattice parameters obtained with Rietveld refinement for the (expanded) austenite phases in all samples versus temperature are presented in Figure 6.16(*d*). The lattice of austenite in the reference AISI 316 powder and in the low-carbon sample expands monotonically in the entire investigated temperature range. Austenite in the high-carbon sample exhibits a slightly expanded lattice, but beyond 800 K the lattice parameter approaches that of the untreated reference sample. This is also the case for austenite formed in the sample containing both nitrogen and carbon. For the high-carbon sample the apparent discontinuity at 800 K is caused by a power failure resulting in cooling of the sample with subsequent reheating to continue the experiment. The fitted coefficients of thermal expansion (equation 4.1) are presented in Table 6.4.

Table 6.4: Fitted coefficients of volumetric (*V*) and linear (*a*) thermal expansion for (expanded) austenite phases as defined by equation (4.1).

Phase	*T* range [K]	α_{exp} [$\times 10^{-5}$ K^{-1}]		
γ_C (high)	385 – 657	*V*	5.53	(7)
		a	1.84	(2)
γ_C (low)	413 – 767	*V*	5.48	(6)
		a	1.82	(2)
γ_{CN}	385 – 657	*V*	5.05	(9)
		a	1.68	(3)

For both samples of carbon expanded austenite, the interstitial content (y_C = 0.18 and 0.22) and coefficients of thermal expansion are similar in value and both slightly lower than the reference and low-nitrogen sample (Table 6.2). In agreement with the observed compositional dependence of the expansion coefficients for nitrided samples, expanded austenite containing both nitrogen and carbon with a higher interstitial content (y_{CN} = 0.24) exhibits lower thermal expansion.

6.3.3 Discussion

Prolonged carburizing has previously been shown to cause formation of both χ-M_5C_2 and M_7C_3 carbides in an expanded austenite zone with high carbon content (e.g. y_C = 0.14 or higher) while for a relatively low carbon content (y_C = 0.056) the main carbide that develops is $M_{23}C_6$ (Ernst *et al.*, 2004; Christiansen & Somers, 2009). For the present samples only χ-M_5C_2 (Hägg carbide) was observed, but M_7C_3 carbide develops above 875 K in the high-carbon sample. The formation of M_7C_3 is in agreement with Thermo-Calc predictions of the stable carbides at high temperature and carbon content (Christiansen & Somers, 2009). To verify this result, part of the high-carbon sample was rapidly heated to 875 K causing a full transformation of the original expanded austenite, ferrite and Hägg carbide to austenite and M_7C_3 (Figure 6.17).

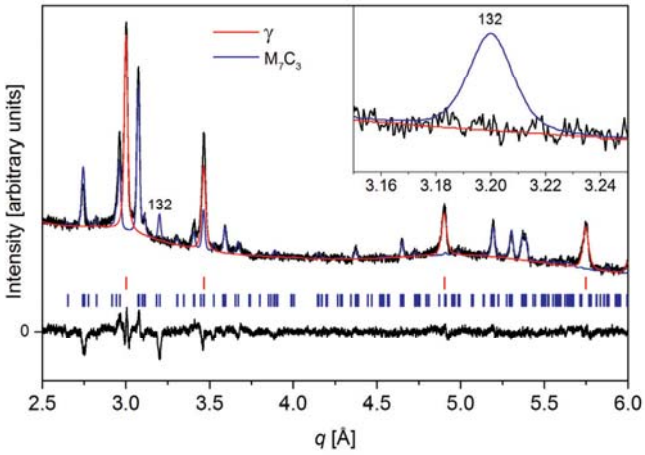

Figure 6.17: X-ray diffractogram, refined Rietveld profile and difference curve up to q = 6.0 Å^{-1} for thermally decomposed carbon expanded austenite, γ_C, at 875 K; constituents are austenite, γ, and M_7C_3 carbide. Vertical lines mark Bragg positions and the inset shows the position of the extinct 132 reflection for M_7C_3.

For the M_7C_3 carbide, the structural description reported by Fruchart & Rouault (1969) was adopted; orthorhombic in space group *Pnma*. The 132 peak predicted for this structure is, however, not observed in the diffractogram (Figure 6.17), which may be explained by a partially disordered structure. The correct orthorhombic crystal structure is obtained at high temperature, but M_7C_3 carbides prepared below 1473 K exhibit crystal imperfections due to formation of twins and stacking faults, resulting in broadening and disappearance of certain diffraction peaks (Rouault *et al.*, 1970). This includes the 132 peak (or 321 for the *Pmcn* setting used in the cited paper) and results in a "poorly crystallized" low-temperature structure indexed according to a hexagonal lattice. For the present data neither the hexagonal description in space group $P6_3mc$ (Herbstein & Snyman, 1964) nor the trigonal

description in space group *P31c* (Westgren, 1935) improved the fit since these predict additional peaks that were not observed. Consequently, the orthorhombic description was maintained and no indications of additional carbides are observed. The stable carbide at sufficiently high carbon content and temperature is thus M_7C_3. The fact that full transformation is obtained at 875 K in contrast to the controlled heating experiment can be explained by thermal oscillations at the beginning of the experiment.

Expanded austenite containing both nitrogen and carbon (y_{CN} = 0.24) is stable up to 657 K, but this temperature coincides with the unintentional oxidation of the sample, which may have affected the stability range. CrN develops during thermal decomposition of the expanded austenite. Since no carbides (or crystalline graphite) were detected, carbon presumably produces amorphous graphite or is simply removed due to oxidation. The stability range for expanded austenite with high carbon content (y_C = 0.22) extends to 657 K while a higher temperature of 767 K was observed for slightly lower content (y_C = 0.18). This is similar to the stability ranges of nitrided samples with high and low interstitial contents. High carbon contents apparently increase the driving force for carbide formation and thus accelerate decomposition. The onset of decomposition of carbon expanded austenite to χ-M_5C_2 may be promoted by the initial presence of this carbide. No stacking fault induced peak shifts are present for the three carburized samples, which indicate a generally diminished stacking fault probability for low interstitial contents, although there is no universally valid relation between the two.

The expansion coefficient for expanded austenite in the low-carbon sample is lower than for the untreated steel. The relatively low discrepancy may be attributed to experimental uncertainty, but can also be interpreted as a consequence of the distinct inhomogeneous carbon distribution. Concentration gradients may be avoided by annealing in an inert (e.g. argon) atmosphere at 773 K after carburizing of sufficiently thin samples (Hummelshøj *et al.*, 2010). As discussed in Section 6.2.4, the unusual compositional dependence of the expansion coefficient of expanded austenite is likely caused by long range order between interstitials, magnetic properties or a combination thereof, which is the subject of the following section.

6.4 Mössbauer spectroscopy and magnetic properties

The f.c.c. structure of iron (austenite, γ-Fe) has been predicted to exhibit either nonmagnetic (paramagnetic), antiferromagnetic or ferromagnetic behavior, depending on the separation of iron atoms (Wang *et al.*, 1985; Moruzzi *et al.*, 1986). The ferromagnetic state is stabilized by larger interatomic distances and has been observed experimentally for epitaxial γ-Fe films grown on Cu and Cu_3Au (Willis *et al.*, 1988; Keune *et al.*, 1989). Room temperature ferromagnetism has been reported for expanded austenite (Öztürk & Williamson, 1995; Fewell *et al.*, 2000; Menéndez *et al.*, 2013) and is mainly attributed to the lattice expansion caused by incorporation of large amounts of nitrogen atoms, possible areas enriched in Fe and Ni and the similarity to the structure of γ'-Fe_4N, which is ferromagnetic at room temperature (Shirane *et al.*, 1962). Ferromagnetic carbon expanded austenite has not been reported, which is in agreement with a limited lattice expansion compared to nitrogen expanded austenite (Hummelshøj *et al.*, 2010). The current investigation aims to explore the relation between interstitial content and magnetic properties of homogeneous samples of nitrogen expanded austenite, which has not been attempted before.

6.4.1 Experimental

Thin foils of AISI 316 stainless steel of nominal composition (by mass) 18% Cr, 10% Ni and 3% Mo (Goodfellow Cambridge Ltd.) with thickness 12.5 μm were used for nitriding. Prior to treatment, recrystallization and austenitization was achieved by heating to 1323 K in pure H_2 followed by immediate cooling to room temperature. In order to obtain a homogeneous distribution of nitrogen in the foils, an alternative activation procedure was applied. The reasons for this change are discussed in Appendix B.1. The procedure involves chemical stripping of the passive film, followed by electrochemical deposition of Ni in a Wood's nickel bath ($NiCl_2$ + $NiSO_4$ + H_2SO_4) with the deposited nickel contributing to less than 0.5 percent of the total mass of the foils as described by Christiansen & Somers (2006a). The thin electrodeposited nickel layer prevents repassivation of the stainless steel and catalyzes the dissociation of ammonia at the surface. Gaseous nitriding of the foil pieces was performed in a Netzsch STA 449 F3 Jupiter thermal analyzer with samples in ceramic crucibles using ammonia, hydrogen and nitrogen gasses of 99.999% purity. Total flow rates of 155 – 255 mL/min were used with a constant N_2 flow of 5 mL/min for protection of electronics in the measurement compartment.

A fully nitrided sample was synthesized in an atmosphere of 97 vol.% NH_3 and 3 vol.% N_2 (infinite nitriding potential) at 693 K for 13 hours. Three additional samples were synthesized with nitriding potentials, K_N, adjusted to 2.40, 0.07 and 0 ($atm^{-1/2}$) after full saturation was achieved, analogous to the low-nitrogen sample in Section 6.1. The nitrided foils were powdered with ultra-sound while submerged in ethanol and dried in air. As

reference, a sample of γ′-Fe_4N was prepared by nitriding iron powder (99.0+% purity, Goodfellow Cambridge Ltd.) with a mean particle size of 6 – 8 μm.

For determination of the lattice parameter, diffraction patterns were recorded with an Agilent SuperNova diffractometer with an Atlas S2 CCD detector using Mo K_α radiation and calibrated with a LaB_6 standard, with samples mounted on adhesive tape (see Appendix B.1, Figure B.9). The nitrogen content as determined from the lattice parameter is given in Table 6.5. Similar to the low-nitrogen sample in Section 6.1, the obtained lattice parameter for zero nitrogen potential is below the minimum value in the reported relation between lattice parameter and interstitial nitrogen occupancy, y_N (Christiansen & Somers, 2006a). Consequently, the relation valid for low interstitial contents, as reported for carbon-expanded austenite (Hummelshøj *et al.*, 2010), was used for this sample, yielding a value in approximate agreement with thermogravimetric results.

Table 6.5: Nitriding potential (K_N), interstitial occupancy of nitrogen (y_N) and stacking fault probability (α_{sf}) of synthesized samples of nitrogen expanded austenite.

K_N [atm$^{-1/2}$]	y_N	α_{sf}
∞	0.55	0.03
2.40	0.38	0.01
0.07	0.29	0.02
0	0.13	0.01

Vibrating sample magnetometry was performed with a Lake Shore Cryotronics 7400 Series Vibrating Sample Magnetometer (VSM) equipped with either a single-stage variable temperature option (model 74035) or a low-temperature variable temperature cryostat (model 74018). The ^{57}Fe Mössbauer spectra were recorded using conventional constant acceleration spectrometers with sources of ^{57}Co in Rh on samples mixed with boron nitride powder. Spectra obtained at low temperatures were recorded in a closed cycle helium refrigerator (APD Cryogenics) and isomer shifts are given with respect to α-Fe at room temperature. Mössbauer spectra were fitted with Lorentzian doublets constrained to equal width and intensity of the two lines and sextets were fitted with Voigt line profiles constrained to an intensity ratio of 3:2:1:1:2:3, with the Gaussian component describing a distribution in hyperfine fields. Isomer shifts were fitted separately for each component and quadrupole shifts fixed to zero.

6.4.2 Results and interpretation

Magnetic hysteresis curves measured at room temperature are presented in Figure 6.18(*a*). Similarly to γ′-Fe_4N, expanded austenite of intermediate nitrogen contents (y_N = 0.29 and

0.38) display only very limited hysteresis and can thus be classified as soft ferromagnets. The specific saturation magnetization for the two compositions is equal within experimental accuracy but significantly lower than for γ′-Fe_4N (Table 6.6). Note that the situation is reversed at low external fields, with expanded austenite exhibiting the highest magnetization.

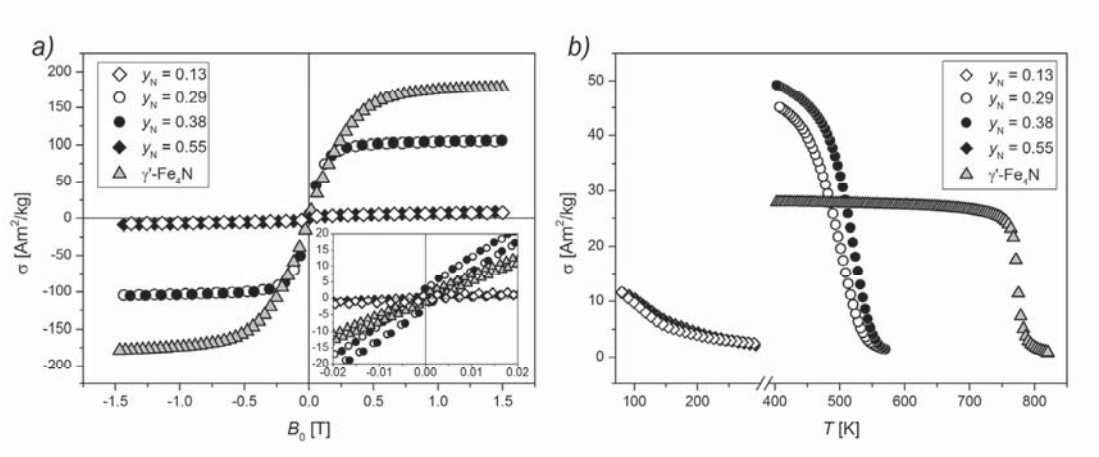

Figure 6.18: *a*) Magnetic hysteresis curves for expanded austenite and γ′-Fe_4N at room temperature and *b*) specific magnetization versus temperature at B_0 = 0.05 T measured at a cooling rate of 1.5 K/min. For clarity only every 30th measurement point or less is shown except for the inset in *a*). Note the break in the temperature scale in *b*).

For both low and high nitrogen contents (y_N = 0.13 and 0.55), only a small ferromagnetic contribution is apparent from the hysteresis curves. This is due to the presence of ferrite impurities, which was verified by X-ray diffraction for y_N = 0.13 (not shown). Ferrite impurities are likely present in all samples, but for higher nitrogen contents Bragg reflections are overlapped with the broadened and shifted reflections from expanded austenite. For low and high nitrogen contents expanded austenite is thus paramagnetic at room temperature. No distinct magnetic transition was observed from magnetization curves measured down to 80 K (Figure 6.18*b*).

Table 6.6: Curie temperature (T_C) and specific saturation magnetization (σ_s) at RT in an applied field of B_0 = 1.5 T determined for nitrogen expanded austenite and γ′-Fe_4N. Values in parentheses denote the maximum measured magnetization for paramagnetic samples, primarily caused by ferrite impurities.

Sample	y_N = 0.13	y_N = 0.29	y_N = 0.38	y_N = 0.55	γ'-Fe_4N
σ_s [Am²/kg]	(8)	105	106	(9)	178
T_C [K]	-	501	520	< 80	774

Curie temperatures, T_C, were determined as the zero-point of the second derivative of magnetization versus temperature curves (Fabian *et al.*, 2013). For γ′-Fe_4N the obtained value, T_C = 774 K, is in agreement with literature, T_C = 767 ± 10 K (Shirane *et al.*, 1962).

Similarly to the saturation magnetization, Curie temperatures for the ferromagnetic compositions of expanded austenite are lower than for γ′-Fe_4N (Table 6.6).

The absence of magnetically split components in Mössbauer spectra for y_N = 0.13 and 0.55 (Figure 6.19) support the results from magnetization measurements, i.e. for both low and high nitrogen contents expanded austenite is paramagnetic at room temperature. This is also the case for the untreated austenitic stainless steel. The volume fraction of the ferrite impurity is sufficiently low to be indistinguishable from the background.

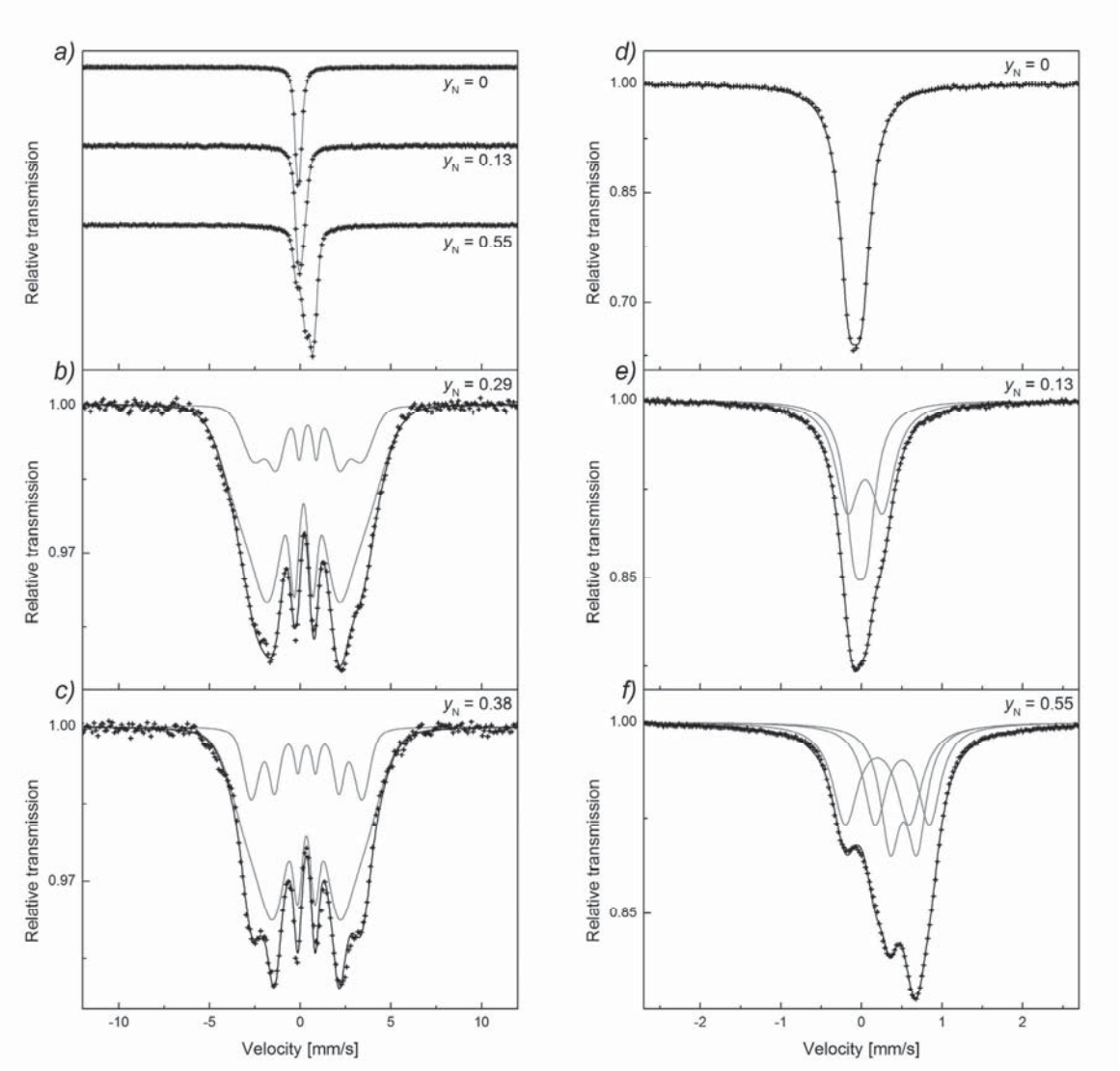

Figure 6.19: Mössbauer spectra recorded at room temperature. *a*) Comparison of AISI 316 austenitic stainless steel (y_N = 0) and expanded austenite with low (y_N = 0.13) and high (y_N = 0.55) nitrogen content. *b+c*) Spectra and fits for intermediate nitrogen contents (y_N = 0.29 and 0.38). *e-f*) Fits of spectra recorded at a reduced velocity range for AISI 316, low and high nitrogen contents. Fits are presented as black lines and the individual sextet and doublet components as grey lines.

In Mössbauer spectra of γ-Fe a singlet should be the only observed component, but additional alloying elements result in quadrupole split doublets due to local variations in symmetry. Nearest and second nearest neighbor configurations of both substitutional and interstitial elements affect the magnitude of the quadrupole splitting (Cook, 1987). The spectrum of the untreated steel can be reasonably described by a single doublet (γ^0) averaging these effects (Figure 6.19*d*).

Table 6.7: Isomer shift (δ), quadrupole splitting (ΔE_Q) and relative contribution (f_i) of doublets designated γ^0, γ^I, γ^{II}, $\gamma^{IV\alpha}$ and $\gamma^{IV\beta}$ fitted to Mössbauer spectra of AISI 316 austenitic stainless steel ($y_N = 0$) and expanded austenite with low ($y_N = 0.13$) and high ($y_N = 0.55$) nitrogen content at RT.

	Sample	$y_N = 0$	$y_N = 0.13$	$y_N = 0.55$
γ^0	δ [mm/s]	-0.079	-0.014	-
	ΔE_Q [mm/s]	0.16	0.15	-
	f [%]	100	47.3	-
γ^I	δ [mm/s]	-	0.044	-
	ΔE_Q [mm/s]	-	0.44	-
	f [%]	-	52.7	-
γ^{II}	δ [mm/s]	-	-	0.20
	ΔE_Q [mm/s]	-	-	0.79
	f [%]	-	-	36.0
$\gamma^{IV\alpha}$	δ [mm/s]	-	-	0.51
	ΔE_Q [mm/s]	-	-	0.67
	f [%]	-	-	31.6
$\gamma^{IV\beta}$	δ [mm/s]	-	-	0.52
	ΔE_Q [mm/s]	-	-	0.33
	f [%]	-	-	32.4

Fitting the Mössbauer spectrum for expanded austenite with $y_N = 0.13$ requires (at least) one additional component (Figure 6.19*e*). This doublet (γ^I) can be attributed to iron atoms with one nitrogen nearest neighbor (Oda *et al.*, 1990). The relative contributions of the two doublet components corresponding to zero and one N neighbor yields an average coordination number of $c_N = 0.53$ for Fe. Since the total interstitial content is $y_N = 0.13$ the coordination number is lower than expected for a random distribution of nitrogen ($c_N = 0.78$). The value does, however, agree favorably with previous EXAFS results, which showed that nitrogen preferentially coordinates to chromium (Oddershede *et al.*, 2010). The short range ordering between N and Cr effectively reduces the coordination number of Fe.

For high nitrogen contents the Mössbauer spectrum is fitted with three doublets (Figure 6.19*f*). The corresponding Fe environments can be interpreted in terms of a point charge approximation (Oda *et al.*, 1990): The first component (γ^{II}) corresponds to Fe with two N

neighbors at opposite octahedral sites, i.e. separated by 180°. The two additional doublets have quadrupole splittings in a 2:1 ratio and similar isomer shifts, which are larger than for any of the previous doublets (Table 6.7). These observations are consistent with Fe having four N nearest neighbors. The nitrogen atoms may either be arranged in a planar configuration where the two remaining empty sites are separated by 180°, on opposite sides of Fe ($\gamma^{IV\alpha}$), or with two adjacent empty sites, separated by 90° ($\gamma^{IV\beta}$). The coordination number calculated from the relative contributions of the doublet components is c_N = 3.3, which is the expected value for a total nitrogen content y_N = 0.55. This suggests that short range order between Cr and N is not dominant in the interstitial ordering for high nitrogen contents.

For the samples of intermediate nitrogen content (y_N = 0.29 and 38) the magnetically split spectra could not be fitted with a reasonable number of individual sextets. Therefore two components were used, each with a Gaussian distribution in hyperfine fields, shown in Figure 6.19(*b*+*c*). The two components do not have any physical meaning but were necessary in order to obtain reasonable approximate fits. The average isomer shifts are between those of expanded austenite with low and high nitrogen contents. The average hyperfine fields (Table 6.8) are somewhat lower than typically found for Fe with two N nearest neighbors in γ'-Fe_4N, which is between 21.4 and 22.0 T (Blancá *et al.*, 2009). Compared to the ordered iron nitride, the lack of well-defined sextets for expanded austenite indicates a more complicated (disordered) structure.

Table 6.8: Hyperfine field (B_{hf}) and isomer shift (δ) of sextets fitted to Mössbauer spectra at 15 K of AISI 316 austenitic stainless steel (y_N = 0) and expanded austenite with y_N = 0.13. For y_N = 0.29, 0.38 and 0.55 two components with Gaussian distribution of hyperfine fields were applied and average values are given. Corresponding room temperature values are marked by (*).

Sample	y_N = 0	y_N = 0.13	y_N = 0.29	y_N = 0.38	y_N = 0.55
B_{hf} [T]	1.80	2.51	24.9 (8)	23.7 (10)	19.4 (4)
			19.0 (10)*	18.1 (9)*	
δ [mm/s]	0.01	0.11	0.37 (2)	0.49 (2)	0.62 (2)
			0.23 (2)*	0.33 (2)*	

Compared to the room temperature Mössbauer spectrum, broadening is observed for the untreated steel at 15 K (Figure 6.20*a*). The broadening is due to a transition from a paramagnetic to an antiferromagnetic state below about 23 K (Flansburg & Hershkowitz, 1970). Broadening is also observed for expanded austenite with y_N = 0.13, presumably caused by an antiferromagnetic transition. Both spectra are fitted with one sextet, but a larger hyperfine field is observed for expanded austenite. The only evident change for intermediate nitrogen contents is an increase of average isomer shifts and hyperfine fields

compared to room temperature values. Unlike expanded austenite with a low nitrogen content, the sample with y_N = 0.55 displays distinct magnetic splitting at 15 K. The resemblance of the spectrum to those of y_N = 0.29 and 38 suggests ferromagnetic ordering but with a lower average hyperfine field. Since no distinct transition was observed in magnetization measurements, the Curie temperature must be between 15 and 80 K.

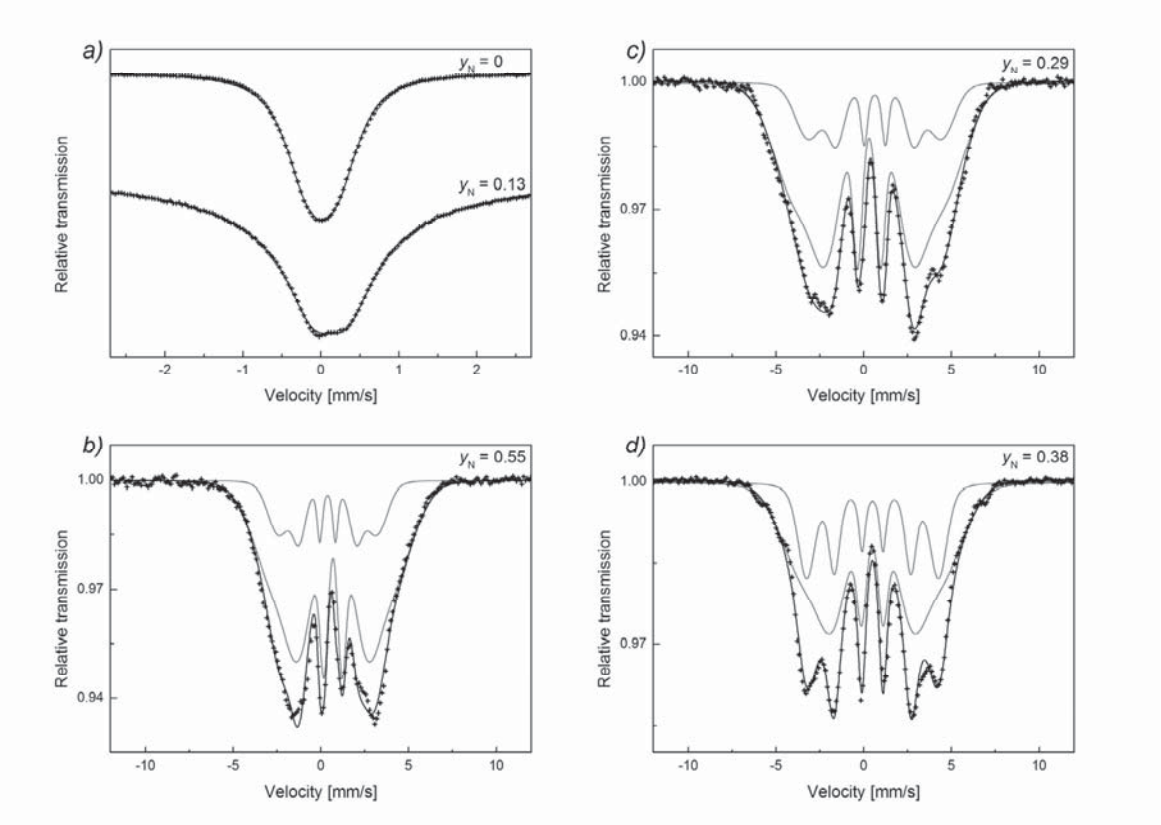

Figure 6.20: Mössbauer spectra recorded at 15 K. *a*) Comparison of AISI 316 austenitic stainless steel (y_N = 0) and expanded austenite with low (y_N = 0.13) nitrogen content fitted with a single sextet. *b-d*) Spectra and fits for high and intermediate nitrogen contents (y_N = 0.55, 0.29 and 0.38). Fits are presented as black lines and the individual sextet components as grey lines.

6.4.3 Discussion

Since Mössbauer spectra for paramagnetic expanded austenite are not well-resolved, other interpretations involving additional components than the currently applied doublets are possible. Exact interpretations are complicated by the fact that the quadrupole splitting is not only affected by the number and configuration of neighboring nitrogen atoms (Oda *et al.*, 1990), but also interstitial second nearest neighbors (Fall & Génin, 1991) and surrounding substitutional elements (Cook, 1987). Overall changes in symmetry of the octahedral coordination environment should also be taken into account, since an apparent deviation from cubic symmetry, as evidenced by X-ray diffraction, is one of the primary features of expanded austenite. These effects could explain why the quadrupole splittings

of component γ^{II} and $\gamma^{IV\alpha}$ are not equal as expected from a point charge approximation. It should, however, be noted that this approximation is not completely valid even in the absence of substitutional elements (Oda *et al.*, 1990).

The lack of a component attributed to iron surrounded by three nitrogen atoms for y_N = 0.55 signifies a clear deviation from a random distribution of nitrogen. Interstitial ordering is expected to cause additional reflections (systematically extinct for f.c.c. structures) in diffraction patterns, as is the case for the primitive cubic structure of γ'-Fe_4N. For expanded austenite these reflections have consistently not been observed with X-ray diffraction but have been reported from selected-area electron diffraction (Jiang & Meletis, 2000). A close inspection of the X-ray diffractogram for y_N = 0.55 does reveal the presence of 110 and 112 reflections (Figure 6.21). The slight discrepancy in ideal and actually observed peak positions is a common feature for expanded austenite.

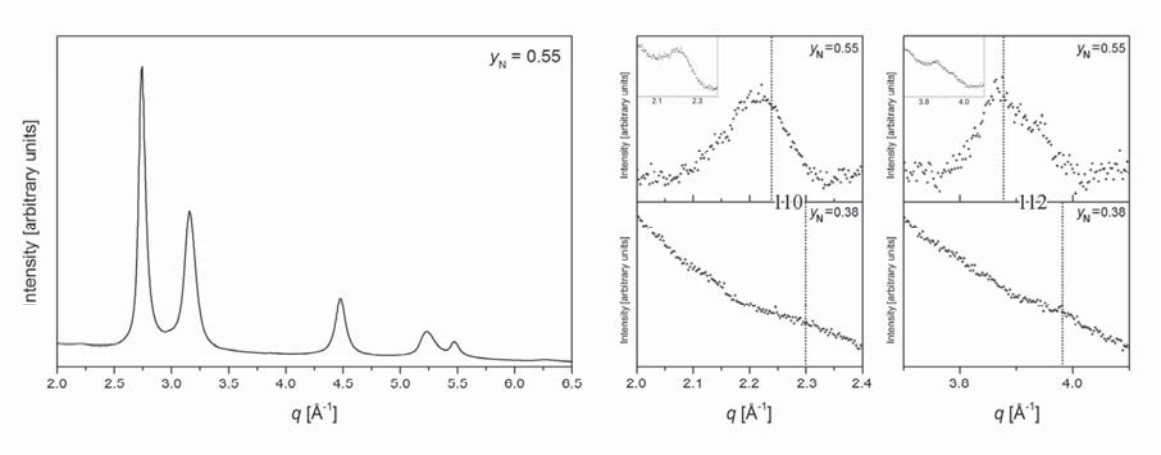

Figure 6.21: X-ray diffractogram of expanded austenite with y_N = 0.55 (left) and ideal positions of 110 and 112 reflections, marked as vertical lines for y_N = 0.55 and y_N = 0.38 (right). Diffraction peaks at these positions are only observed for y_N = 0.55 (background is subtracted but shown in the insets). Note that, although diffractograms contain both $K_{\alpha 1}$ and $K_{\alpha 2}$ components, the conversion to q-space is done with a single intensity-averaged wavelength, λ = 0.7107 Å.

The structure of γ'-Fe_4N, in which Fe has either zero or two N neighbors, can be considered as an f.c.c. arrangement of Fe with N in the body-centered octahedral site. A structure composed of metal atoms with only two or four nitrogen neighbors (components γ^{II} and $\gamma^{IV\alpha}$) can be realized with additional N in octahedral sites on one set of parallel cube edges. Additional reflections indicating a larger unit cell, which is required for an ordered structure incorporation also component $\gamma^{IV\beta}$, were not observed. This arrangement must therefore be realized by short range ordering.

Isomer shifts of the fitted components increase both as a result of lattice expansion, which reduces the *s*-electron density at the iron nuclei, and with increased number of nitrogen neighbors. The increase caused by nitrogen nearest neighbors may be explained from an increased screening effect from *d*-electrons due to hybridization of nitrogen 2*p* states with the iron 3*d* band as in γ′-Fe_4N (Sifkovits *et al.*, 1999).

The Curie temperatures determined for y_N = 0.29 and 0.38 (501 and 520 K, respectively) are lower than the temperature around 560 K, at which a change in thermal expansion coefficients was observed for y_N = 0.33 (Section 6.2.3). As seen from Figure 6.18(*b*), the magnetic transition is not sharply defined and a fully paramagnetic state is only achieved above 550 K. This indicates that the change in expansion coefficient is indeed caused by variations in magnetic properties.

The coefficients of (linear) thermal expansion for all (expanded) austenite phases are presented in Figure 6.22 versus lattice parameter, *a*, at room temperature. The lattice parameter is related to the interstitial content, but different relations exist for interstitial occupancy of nitrogen (Christiansen & Somers, 2006a) and carbon (Hummelshøj *et al.*, 2010), with a systematically larger lattice parameter for γ_N. For the two samples of carbon expanded austenite, the estimated interstitial content (y_C = 0.18 and 0.22) exceeds the reported validity range of the linear relation and that of the low-nitrogen sample (y_N = 0.14) is below the minimum value in the reported relation. For the sample containing both nitrogen and carbon, an average value of the two relations (y_{CN} = 0.24) was used, which is an approximation at best (the respective values of the two relations are y_{CN} = 0.21 and 0.28). Therefore, the representation versus lattice parameter, which is directly related to experimental results obtained in this work, without approximate conversions, is preferred.

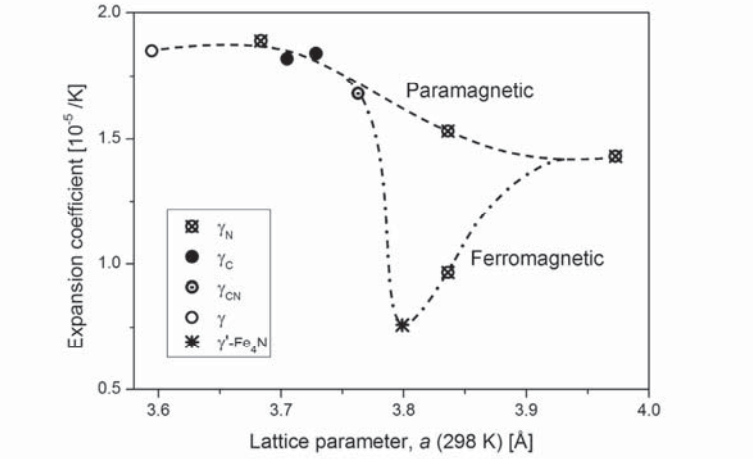

Figure 6.22: Coefficients of linear thermal expansion versus lattice parameter at room temperature (linearly related to the interstitial content) for expanded austenite compared to the value of γ′-Fe_4N (Somers *et al.*, 1989b). Dashed lines are added to guide the eye.

The relatively low expansion coefficient for intermediate nitrogen content is the result of spontaneous volume magnetostriction in the ferromagnetic state. This is similar to the effect responsible for the low coefficient of thermal expansion for Invar alloys (Pepperhoff & Acet, 2001), although to a lesser extent for expanded austenite.

Spontaneous volume magnetostriction may also explain why the reported relation between lattice parameter and interstitial content for nitrogen expanded austenite (Christiansen & Somers, 2006a) does not include the value for the untreated steel at $y_N = 0$. The ferromagnetic transition is induced by lattice expansion. No such transition has been reported for carbon expanded austenite, which is consistent with a lower solubility of carbon compared to nitrogen (Hummelshøj *et al.*, 2010), resulting in insufficient expansion of the lattice. Evaluating the difference between lattice parameter for nitrogen and carbon expanded austenite at $y_{N/C} = 0.17$ yields a spontaneous volume magnetostriction of 3.5% at room temperature, which is higher than for traditional Fe-Ni Invar alloys (Hayase *et al.*, 1973). Extrapolating the difference between paramagnetic and ferromagnetic coefficients of thermal expansion for $y_N = 0.33$ (Section 6.2.3) to room temperature yields a lower spontaneous volume magnetostriction of 1.5%, consistent with a decreasing magnetic contribution with increasing nitrogen content.

Dashed lines in Figure 6.22 correspond to possible relations between interstitial content (initial lattice parameter) and expansion coefficients for paramagnetic and ferromagnetic states. The value for γ'-Fe_4N (Somers *et al.*, 1989b) is included since the lattice parameter at room temperature coincide with that of expanded austenite with comparable nitrogen content, $y_N = 0.25$ (Christiansen & Somers, 2006a). Since the magnetic properties of samples with $y_N = 0.29$ and 38 are very similar, the trends for intermediate nitrogen contents are not completely clear. The higher Curie temperature observed for $y_N = 0.38$ compared to $y_N = 0.29$ indicates that the minimum in expansion coefficients, or even possible multiple local minima, may correspond to different compositions than $y_N = 0.25$.

The indicated decreasing trend for paramagnetic samples with increasing interstitial content may intuitively be explained from the considerations mentioned in Section 6.1.3.1: For an already substantially expanded lattice, additional thermal contributions could be expected to have a relatively lower effect. A complete description requires a detailed understanding of the crystal structure and the anisotropic vibrations in the crystal lattice, which is currently not available.

6.5 Conclusions

The *in situ* synchrotron X-ray diffraction investigation of the thermal decomposition of expanded austenite with high (y_N = 0.56) and low (y_N = 0.14) nitrogen content shows that the development of CrN is promoted by a high nitrogen content. For y_N = 0.56 the formation of CrN is accompanied by the development of a transitional phase with a nitrogen content corresponding to M_4N (y_N = 0.25), consistent with (discontinuous) precipitation. For low nitrogen contents CrN forms along with ferrite, indicating a eutectoid transformation. Thermal decomposition of carbon expanded austenite leads to initial formation of Hägg carbide followed by M_7C_3.

Interpretation of diffractograms of nitrogen expanded austenite with Rietveld refinement necessitated the implementation of Warren's approximation for the effect of stacking faults on *hkl*-dependent shifts of Bragg reflections. Although the contributions to peak broadening were not specifically taken into account, this simplified model allows for a consistent interpretation of diffraction data. Deficiencies in the stacking fault model are explored in detail in the following chapter.

For both low and high nitrogen contents, expanded austenite is paramagnetic at room temperature while ferromagnetism is observed for intermediate contents. The anomalous variation in thermal expansion coefficients with interstitial content is a consequence of spontaneous volume magnetostriction in the ferromagnetic state. In the paramagnetic state, the decrease in thermal expansion coefficient with increasing nitrogen content is attributed to the additional expansion of the lattice due to interstitial atoms. Accordingly, the contribution of thermal vibrations to the expansion of the lattice becomes less pronounced.

Variations in thermal expansion coefficients have practical implications for surface layers of expanded austenite. In addition to compositional stresses, a thermally induced stress profile may develop during cooling from the treatment temperature. For all currently investigated compositions, expanded austenite is paramagnetic at the applied nitriding temperature. The Curie temperature, and hence the onset of spontaneous volume magnetostriction, depends on nitrogen content. The resulting change in thermal expansion coefficient adds additional complexity to the stress profile.

Chapter 7

The structure of expanded austenite

There is currently no consistent structural description of expanded austenite that accounts for the *hkl*-dependent shifts and broadening observed in diffraction experiments. The best available description, first proposed by Sun *et al.* (1999), and valid for the 111, 200 and 220 peaks of homogeneous samples (Christiansen & Somers, 2004), is an f.c.c. lattice with stacking faults contributing to systematic deviations of diffraction peaks as described by Warren (1969). The most prominent complicating features of diffractograms of expanded austenite is the anomalous position of the 200 peak, which is shifted to lower diffraction angles compared to an ideal f.c.c. lattice, and the anisotropic broadening, which is least pronounced for the 111 peak.

Fewell & Priest (2008) reviewed ten plausible candidate structures on the basis of synchrotron X-ray diffraction on samples of an expanded austenite zone grown into an austenite substrate. For such samples, the resulting compositional inhomogeneity and induced macrostress gradient over the expanded austenite zone complicates the analysis, since these two effects also cause peak shifts and broadening. Higher order reflections, up to 622, were available due to the use of synchrotron radiation. The evaluated structural models included proposed tetragonal (Angelini *et al.*, 1988) and triclinic (Fewell *et al.*, 2000) lattices amongst others, since observed broadening may be caused by deformation-induced splitting of diffraction peaks. It should be noted that the analysis by Fewell & Priest neglects negative values of Miller indices. They claim, for example, that the 111 reflection is not split on deforming an f.c.c. structure to monoclinic, equal-sided triclinic or rhombohedral

lattices. It is, however, quite straightforward to show that in general $(111) \neq (11\bar{1}) \neq (1\bar{1}1) \neq (\bar{1}11)$ in the triclinic case and that both monoclinic and rhombohedral deformation also leads to split reflections. For the structural model designated 'Monoclinic A' with lattice parameters a = 3.7593 Å, b = 3.7094 Å, c = 3.8358 Å and β = 91.54° the interplanar spacings are $d_{11\bar{1}} = d_{\bar{1}11}$ = 2.1939 Å and $d_{111} = d_{1\bar{1}1}$ = 2.1555 Å and are thus clearly not equal. This of course has implications for the other considered reflections as well but only serves to further decrease the validity of these models and does therefore not impact the overall conclusion: No simple structural model seems sufficient to describe expanded austenite.

The shifts observed for higher order diffraction peaks cannot be accounted for by stacking faults alone. It should be noted that the basis for the stacking fault model, Warren's theory, has been demonstrated to be insufficiently accurate (Velterop *et al.*, 2000) due to unrealistic simplifying assumptions, for example averaging the shift of all components of a given reflection. The various profile components comprising a diffraction peak are not equally affected, or may be entirely unaffected by stacking faults. It was convincingly shown by Velterop *et al.* that a weighted summation should be used. The affected component of the 111 peak, for example, is increasingly shifted with increasing stacking fault probability but is also broadened. This leads to a decreasing shift of the maximum intensity for the overall peak profile above a certain stacking fault probability (see Figure 7.3). Peak positions given in this chapter refer to the peak maximum following the treatment of Warren since the experimental determination of the centroid is usually difficult and is affected by asymmetries, which may arise from e.g. twin faults.

The expression derived by Velterop *et al.* additionally introduces a size-dependence but is too complicated to be readily implemented in a Rietveld procedure. In an effort to obtain a simple (approximate) relation between stacking fault probability, peak shifts and broadening comparable to that of Warren, avoiding the erroneous simplifying assumptions, Debye simulations were used. Results are compared to synchrotron X-ray diffraction data previously obtained (Oddershede *et al.*, 2008a) for a homogeneous sample of nitrogen expanded austenite with interstitial occupancy, y_N = 0.61, with reported lattice parameter, a = 4.0022 Å and stacking fault probability, α_{sf} = 0.0362 (according to Warren).

7.1 Debye simulations

Without any assumptions regarding periodicity, the diffracted intensity, $I(q)$, of randomly oriented identical scattering objects can be calculated as a sum over all the interatomic distances, r_{ij}, according to the Debye (1915) scattering equation:

$$I(q) = \sum_{i,j}^{N} f_i(q) f_j(q) \sin(q \cdot r_{ij}) / (q \cdot r_{ij}) \tag{7.1}$$

where f_i and f_j are the atomic scattering factors, $q = 4\pi\sin\theta/\lambda$ is the magnitude of the scattering vector and N is the number of atoms. It is thus possible to calculate the diffracted intensity of any atomic array defined in terms of crystallographic parameters such as atomic composition, coordinates and thermal parameters and explore the effects of crystallographic defects like stacking faults.

A face-centered cubic crystal can be considered as a layered structure produced by the stacking of close-packed (111) planes denoted A, B and C with an unfaulted stacking sequence ABCABC (or CBACBA). This structure can contain three essentially different types of stacking faults (Read, 1953): Intrinsic, extrinsic and twin (growth) faults. Intrinsic faults correspond to the removal of a close-packed plane from the perfect crystal, extrinsic faults to the insertion of an extra close-packed plane and twin faults to reversal of the stacking sequence (Figure 7.1). Note that an extrinsic fault can be considered as two consecutive intrinsic faults and that additional intrinsic faults result in a twin.

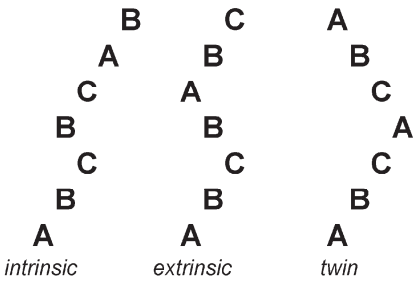

Figure 7.1: Stacking sequences for intrinsic, extrinsic and twin faults.

Simulations were carried out with a modified version of the Debye program developed by Oddershede *et al.* (2008a). The simulated crystal structures consist of N layers of $N \times N$ primitive hexagonal unit cells shifted to A, B or C positions. The symmetry of the atomic array is exploited to speed up the calculation of all the Fe—Fe interatomic distances, e.g. equal distances between layers and between atoms within each layer regardless of the layer position. Nitrogen atoms in octahedral interstitial positions alter the relative intensities of the diffraction peaks but has no impact on the peak widths (Oddershede *et al.*, 2008a) and is not expected to contribute significantly to the change in peak positions on the introduction of stacking faults. Nitrogen atoms were therefore omitted and all metal atoms on the f.c.c. lattice were modelled as Fe with a thermal parameter set to $B = 1$ Å^2, which is reasonable at room temperature. For comparison with the experimental data, instrumental peak broadening of the pseudo-Voigt type (Caglioti *et al.*, 1958; Wertheim *et al.*, 1974) as determined from a Si standard (Oddershede *et al.*, 2008a) was added as well as correction for the intensity profile related to the Guinier tangent angle (Sas & de Wolff, 1966).

The atomic array is constructed by successive generation of close-packed (111) layers. Each time a new layer is added, a random number between 0 and 1 is generated. If the number is below the input stacking fault probability, a stacking fault is introduced. The final stacking fault probability, α_{sf}, is defined as the number of faults in the atomic array divided by the total number of layers such that the average number of layers between faults is $1/\alpha_{sf}$. Crystallites of 100^3, 250^3, 400^3, 550^3 and 700^3 atoms with stacking fault probabilities of zero, 0.03, 0.06 and 0.09 were simulated with the maximum size limited by required computation time. In order to obtain a more realistic model than given by a single stacking sequence, 50 diffractograms were simulated for each crystallite size, i.e. a total of 250 for each value of α_{sf}. These were averaged with weights according to a Weibull size distribution with parameters fitted to two NIST Standard Reference Materials (660a) Lanthanum Hexaboride and (640c) Silicon (Oddershede, 2007). This corresponds to a mean crystallite diameter of around 830 Å for the simulations carried out with an f.c.c. lattice parameter of 4.00 Å. Diffractograms were simulated with a wavelength of λ = 1.00 Å in a 2θ range of 15 – 100° (corresponding to a q range from 1.6 to 9.6 A^{-1}) with a fixed step size of 0.005° in 2θ.

7.1.1 Peak shifts

Simulated diffractograms for an unfaulted f.c.c. lattice and stacking sequences of (111) layers including intrinsic, extrinsic and twin fault, with a stacking fault probability of 0.03, are given in Figure 7.2. Intensities are scaled relative to the maximum intensity of the 111 peak in order to emphasize relative changes and the shift of the 111 peak (on an absolute scale, the introduction of stacking faults decreases the maximum intensity due to peak broadening, since the integrated intensity is preserved). It can be seen that twin faults alone do not contribute to any significant peak displacement but cause considerable broadening. For intrinsic and extrinsic stacking faults, peaks are both broadened and shifted. The *hkl*-dependent peak shift is similar in magnitude but of opposite sign. According to Warren (1969), the peak maximum shift caused by intrinsic stacking faults is given by:

$$\Delta 2\theta\ (^\circ) = \frac{90\sqrt{3}\tan\theta_0}{\pi^2} \cdot \alpha_{sf} \cdot G_{hkl} \tag{7.2}$$

where $2\theta_0$ is the diffracting angle of the peak maximum for the unfaulted lattice and the stacking fault parameter G_{hkl} is given according to Table 7.1. For extrinsic stacking faults the stacking fault parameter for a given *hkl* reflection is equal in magnitude but opposite in sign (Warren, 1963). Since the angular shifts are small, the peak maximum shift can be given on a q scale by using a small angle approximation and substituting $\Delta 2\theta(^\circ)/\tan\theta_0 = (360/\pi)[(\sin\theta - \sin\theta_0)/\sin\theta_0] = (360/\pi)[(q - q_0)/q_0]$ in equation (7.2), yielding:

$$\frac{q - q_0}{q_0} = \frac{\sqrt{3}}{4\pi} \cdot \alpha_{sf} \cdot G_{hkl} \tag{7.3}$$

where q_0 refers to the unfaulted lattice and q to the shifted position. The shifts of four selected reflections obtained from simulations are compared to the results of Warren (1969) and Velterop *et al.* (2000) in Figure 7.3. In Warren's model, a small stacking fault probability and infinitely large crystallites were assumed, while the expression derived by Velterop *et al.* introduces a size-dependence and shows a distinct non-linearity in the peak shifts for increasing stacking fault probabilities. In addition, it shows for certain reflections, e.g. 311, that the shift is in the opposite direction compared to that predicted by Warren. The shifts obtained from Debye simulations are within those corresponding to the number of layers N = 100 and N = 1000 according to Velterop *et al.* for the 111 and 311 reflections. This is in agreement with the applied size distribution being within these two values. It is also noted that the correct sign (according to Velterop *et al.*) of the 311 peak shift is obtained from the current simulations.

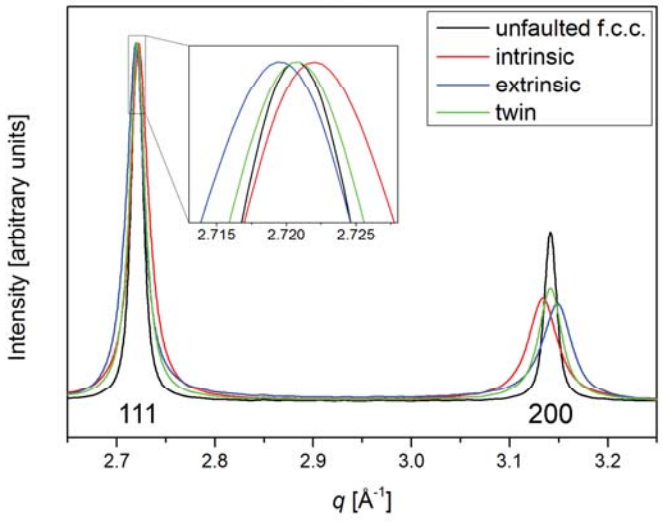

Figure 7.2: Section of simulated diffractograms for a perfect f.c.c. lattice and stacking sequences including intrinsic, extrinsic and twin faults with a stacking fault probability of 0.03. Intensities are normalized with respect to the maximum intensity of the 111 peak.

To account for the varying peak shifts with increasing fault probability, the stacking fault parameter, G_{hkl}, was fitted as two separate regions; a constant up to the first simulated point, α_{sf} = 0.03 and beyond this value a linear relation, $G_{hkl} = a \cdot \alpha_{sf} + b$, was chosen as an approximation. The fits allow a satisfactory description of the (admittedly, low number of) simulated points and obtained values are given in Table 7.1. Due to the full overlap of

511/333 and 600/442 reflections, a combined value is obtained for these from simulated diffractograms.

When comparing with experimental data it is important to note that the applied size distribution may not correspond to the actual size of coherently diffracting domains in expanded austenite. The maximum simulated size is limited by required computation time. According to Velterop *et al.* increasing size effectively eliminates the shift of 111 and 311 reflections while 331 and 200, of which the latter accounts for the largest observed peak shift for expanded austenite, does not display any size dependence (at least up to $N = 1000$).

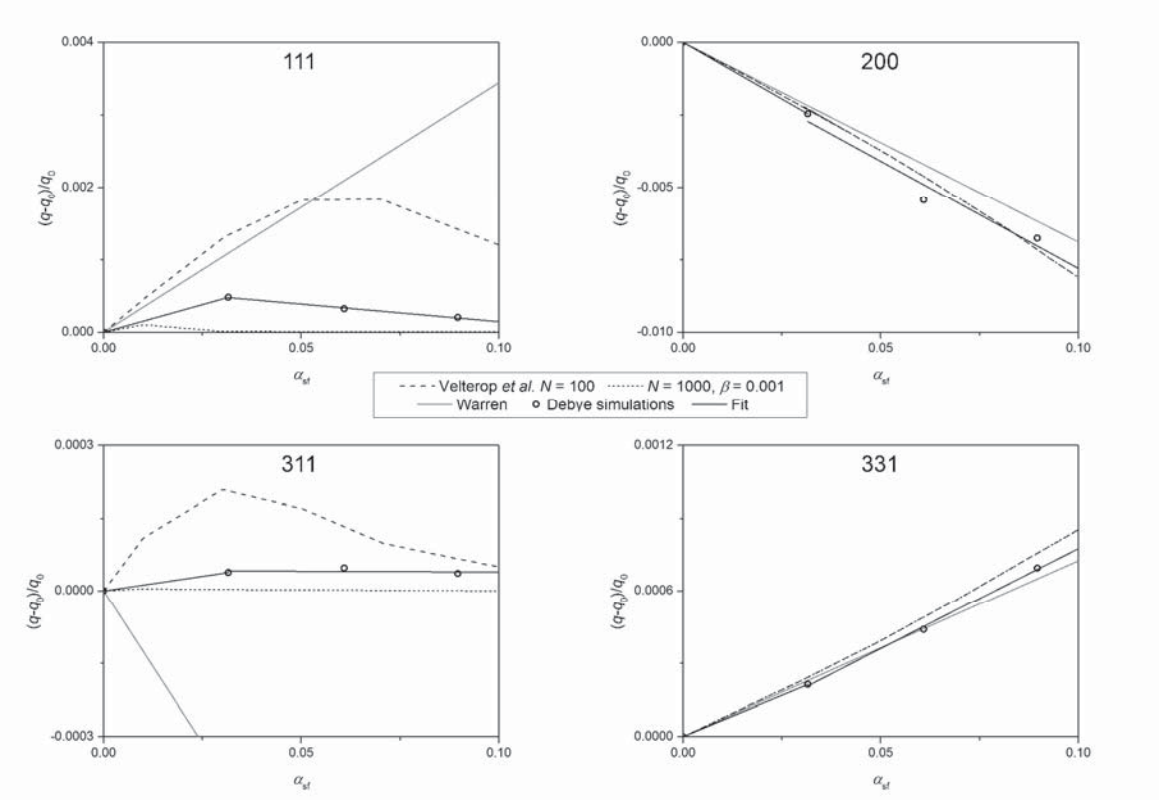

Figure 7.3: Peak maximum shift as a function of intrinsic stacking fault probability for the 111, 200, 311 and 331 reflections compared to the values obtained by Warren (1969) and Velterop *et al.* (2000), where N denotes the number of layers and β the twin fault probability. Values obtained from fits are given in Table 7.1.

Both previous models and the Debye simulations rely on two, not necessarily realistic, assumptions; (*i*) faults occur in only one crystallographic orientation per crystallite, e.g. only on (111) of the {111} planes and (*ii*) stacking faults span the entire crystal. For real crystals, stacking faults may, however, end inside the crystal and be bordered by partial dislocations (Read, 1953). This may cause deviations from the predicted peak shifts and

broadening. In any case, the currently obtained values should be considered as an improvement compared to those obtained by Warren and are deemed sufficient to verify the validity of the stacking fault model for expanded austenite.

Table 7.1: Stacking fault parameter according to Warren (1969) and from fits of Debye simulations (constant up to α_{sf} = 0.03 and linear, $G_{hkl} = a\ \alpha_{sf} + b$ above this value). The stacking fault parameter for extrinsic faults according to Warren (1963) is equal in magnitude but opposite in sign.

		Intrinsic			Extrinsic		
	G_{hkl}, Warren	G_{hkl}	a	b	G_{hkl}	a	b
111	1/4	0.1106	-0.0349	0.0046	-0.1044	0.0386	-0.0044
200	-1/2	-0.5639	-0.5388	-0.0027	0.5359	0.8191	-0.0110
220	1/4	0.0134	-0.0059	0.0006	-0.0107	0.0053	-0.0005
311	-1/11	0.0088	-0.0002	0.0003	-0.0082	0.0005	-0.0003
222	-1/8	-0.0587	0.0168	-0.0024	0.0487	-0.0189	0.0020
400	1/4	0.2721	0.3000	0.0000	-0.2755	-0.3281	0.0011
331	1/19	0.0490	0.0602	-0.0004	-0.0432	-0.0652	0.0007
420	1/20	-0.0222	0.0053	0.0053	0.0185	-0.0060	0.0008
422	0	0.0215	-0.0076	-0.0076	-0.0212	0.0084	-0.0009
511	-1/36	-0.0087	0.0032	0.0032	0.0084	-0.0035	0.0003
333	0						
440	-1/8	-0.0098	0.0041	0.0041	0.0072	-0.0035	0.0003
531	9/245	0.0109	-0.0007	-0.0007	-0.0097	0.0009	-0.0003
600	0	-0.0144	0.0001	-0.0005	0.0108	-0.0009	0.0004
442	1/24						

The peak shifts, or lack thereof, caused by extrinsic and twin faults can immediately be seen not to correspond to experimental observations for expanded austenite since only intrinsic faults predict a shift of the 200 reflection to lower q values. Since q_0 is not known a priori, a lattice parameter corresponding to the unfaulted lattice, a_0, and the intrinsic stacking fault probability was fitted to match the experimental 111 and 200 peak positions for nitrogen expanded austenite (obtained values are a_0 = 3.9961 Å and α_{sf} = 0.06). In the case where the stacking fault model is applicable the peak shift of additional reflections are expected to approximately align with the predicted values, which is clearly seen from Figure 7.4 not to be the case (which is why a simultaneous fit of all reflections is meaningless). It is, however, also evident that deceptively reasonable fits can easily be obtained considering only the first three reflections; 111, 200 and 220. Observations of only these peaks would thus naturally lead to the conclusion that the stacking fault model is valid.

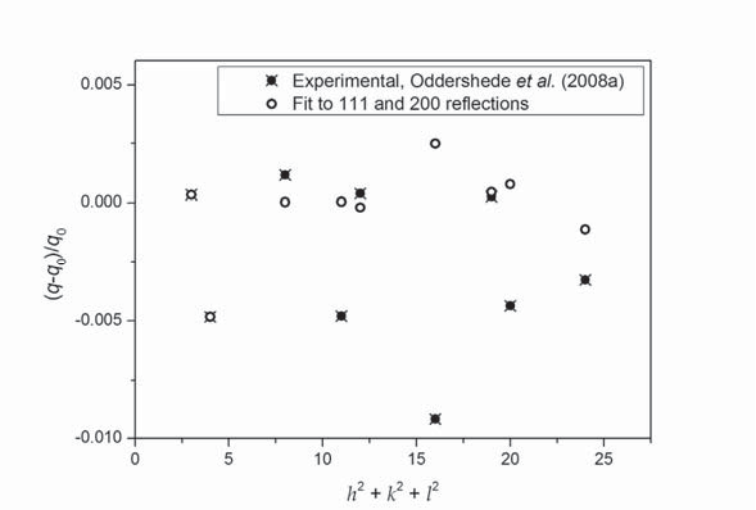

Figure 7.4: Peak shift caused by intrinsic stacking faults according to Table 7.1 fitted to match the 111 and 200 peak of experimental data for nitrogen expanded austenite (Oddershede *et al.*, 2008a).

Based on the results obtained from Debye simulations it can be concluded that stacking faults alone cannot account for the peak shifts observed for expanded austenite. It can be argued that a combination of intrinsic and extrinsic faults, with a majority of intrinsic faults, also lead to negative shifts of the 200 reflection. A simple linear combination is, however, not applicable since predicted shifts for both fault types are low for reflections with increasing *hkl*, while this is not the case for experimental data.

7.1.2 Peak broadening

The peak broadening caused by the three types of stacking faults is shown in Figure 7.5 and compared to the experimental data. The Full Width at Half Maximum (FWHM) of the diffraction peaks is denoted Δq, and all widths include the same instrumental contribution. It is seen that all fault types primarily cause broadening of the 200 and 400 peaks while most other peaks are relatively unaffected. The experimental data is compared to peak widths obtained for a stacking fault probability $\alpha_{sf} = 0.06$. Neither fault type can account for the experimental broadening, which shows a general increasing trend for increasing *hkl*, except for 222 and 422 reflections. Both observed peak shifts and broadening thus seem decisively against the stacking fault model for expanded austenite when considering more than the three first reflections. Since the lattice of expanded austenite is expanded due to the presence of interstitial atoms, the variations in octahedral interstitial positions caused by an altered stacking sequence should, however, also be explored.

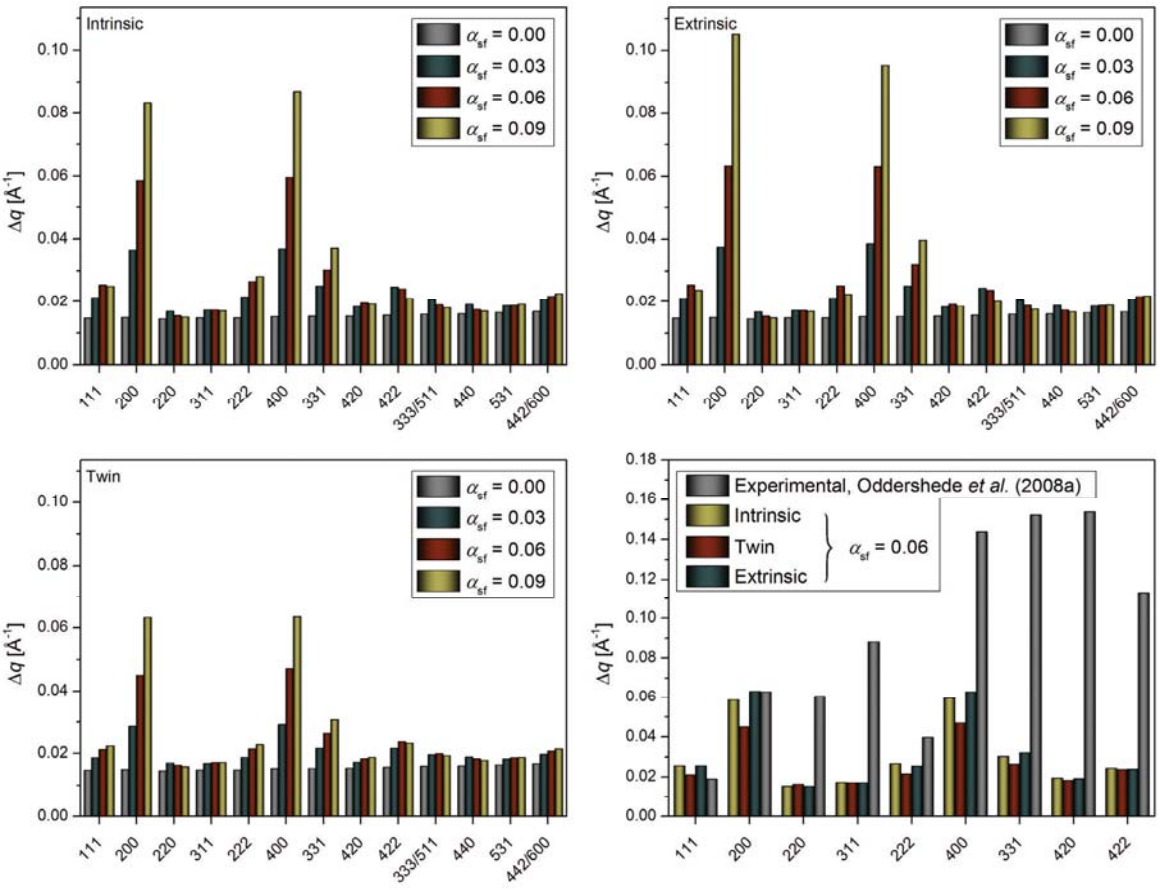

Figure 7.5: Peak widths, Δq, (including instrumental broadening) for simulated diffractograms of intrinsic, extrinsic and twin faults and comparison of stacking fault probability α_{sf} = 0.06 for the three types of faults with experimental data for expanded austenite (Oddershede *et al.*, 2008a).

7.1.3 The effect of stacking faults on octahedral interstitial positions

Stacking faults in a close-packed metallic structure do not change the distance between close-packed layers, but the relative positions of interstitial octahedra do change. For f.c.c. lattices, the introduction of an intrinsic stacking fault, for example, creates a local h.c.p. sequence cf. Figure 7.1. In f.c.c. structures octahedra only share edges while an h.c.p. stacking results in both edge- and face-sharing octahedra (Figure 7.6). The decreased separation of interstitial positions in face-sharing octahedra is unfavorable and induces strong repulsive interactions in the case of simultaneous occupation of two such sites, which partly explains the interstitial ordering in the h.c.p. based ε-iron nitride (see Section 2.2.1). It is therefore possible that the sites neighboring stacking faults are less likely to be occupied, causing a local contraction of the layers. Comparing the separation of {111} layers in the simulated structure (a_0 = 4.00 Å) with the corresponding planar spacing in the ε-nitride (Somers *et al.*, 1997) extrapolated to the maximum achievable occupancy where face-sharing octahedra are avoided (half of the interstitial positions filled), suggests a layer

contraction of 4%. Note that, at this composition, a rearrangement of nitrogen occurs in the ε-nitride resulting in the orthorhombically distorted structure ζ-Fe_2N (Jack, 1948a), but with a minimal change in layer separation.

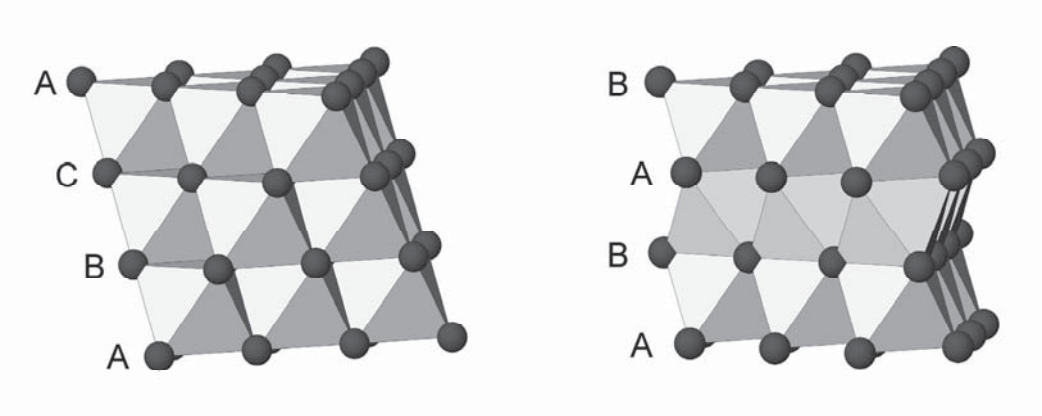

Figure 7.6: Octahedral positions in close-packed structures; edge-sharing in f.c.c. (left) and both edge- and face-sharing in h.c.p. (right). The stacking sequence is indicated.

Simulations were performed for α_{sf} = 0.03 with a contraction of 4% for the three affected interplanar distances on the introduction of an intrinsic stacking fault. Since the distances between layers are no longer equal, the simulations were reconfigured to calculate all interatomic distances without exploiting the symmetry of the atomic array. This drastically increases the computation time and only 100^3 atoms were therefore simulated.

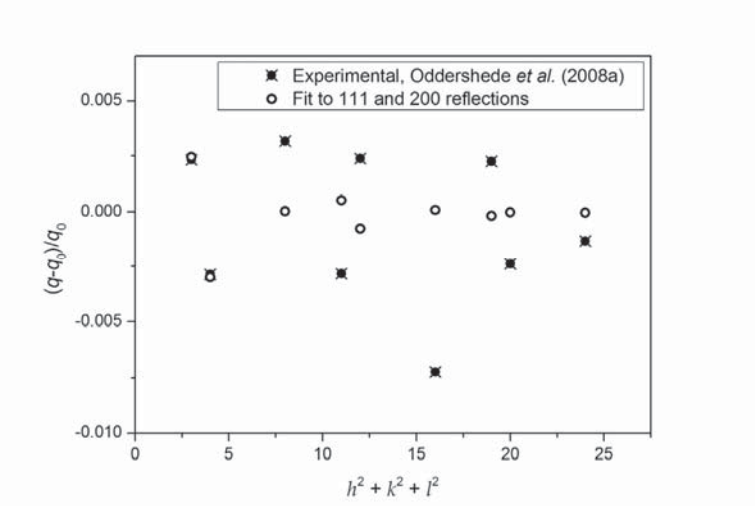

Figure 7.7: Peak shifts caused by intrinsic stacking faults (α_{sf} = 0.03) with a layer contraction of 4%. The unfaulted lattice parameter for the experimental peak shifts (Oddershede *et al.*, 2008a) was fitted to obtain the best match for the 111 and 200 peak positions.

Results are shown in Figure 7.7. Since only a single value of the stacking fault probability was used for simulations, only the unfaulted lattice parameter can be fitted (a_0 = 4.0040 Å). Comparing with Figure 7.4 it is seen that including layer contraction improves the

predicted positions for certain peaks (e.g. 400) while the disagreement is increased for others (e.g. 331). Peak positions are thus affected by changing interplanar distances on the introduction of stacking faults but cannot explain the experimentally observed peak shifts of expanded austenite. This was also verified for simulations of arbitrarily chosen 10% layer contraction and expansion (not shown).

7.2 Elastic anisotropy and dislocations

Based on Debye simulations, a high density of screw dislocations was proposed to explain the observed broadening of diffraction peaks for expanded austenite (Oddershede *et al.*, 2008a), which cannot be accounted for by stacking faults alone. The anisotropic strain broadening caused by dislocations can, in many cases, be described by taking into account the so-called contrast factors of dislocations, C_{hkl} (Ungár & Borbély, 1996). For randomly populated slip systems or untextured polycrystals, the contrast factors can be averaged and the FWHM of diffraction peaks, Δq, can be expressed by the modified Williamson-Hall plot as (Ungár & Borbély, 1996; Ungár *et al.*, 2001):

$$\Delta q = A + B\left(q\overline{C}^{1/2}\right)^2 + O\left(q\overline{C}^{1/2}\right)^4 \tag{7.4}$$

where $\overline{C}$ is the average contrast factor for dislocations, A is a parameter depending on the apparent size of crystallites or coherently diffracting domains, B depends on the average dislocation density, the magnitude of the Burgers vector and the effective outer cut-off radius of dislocations and O denotes non-interpreted higher order terms, which are disregarded. For the most common slip systems in f.c.c. crystals, the average contrast factors for pure screw and pure edge dislocations can be calculated from the elastic constants (Ungár *et al.*, 1999).

The elastic properties of metallic f.c.c. structures are typically anisotropic with the highest elastic modulus in <111> directions while <100> directions are the most compliant. The elastic constants for expanded austenite are not known, but the elastic modulus depends on interstitial content and exhibits a maximum in <100> directions (Tromas *et al.*, 2012), although this may be the result of unresolved orientation-dependent differences in nitrogen concentration. The anisotropy of expanded austenite is thus reversed similar to the elastic properties of γ'-Fe_4N (Gressmann *et al.*, 2007; Takahashi *et al.*, 2012). The average contrast factors were calculated for pure screw and pure edge dislocations and a combination of half screw and half edge dislocations according to Ungár *et al.* (1999) using the elastic constants of AISI 304 austenitic stainless steel (Ledbetter, 1984) and γ'-Fe_4N (Gressmann *et al.*, 2007) as approximations. Corrections for instrumental broadening for the

experimental data was applied assuming the contributions add up in a Gaussian manner; $\Delta q^2_{total} = \Delta q^2_{sample} + \Delta q^2_{instrument}$. In any case, the instrumental contribution is negligible compared to the broadening of expanded austenite.

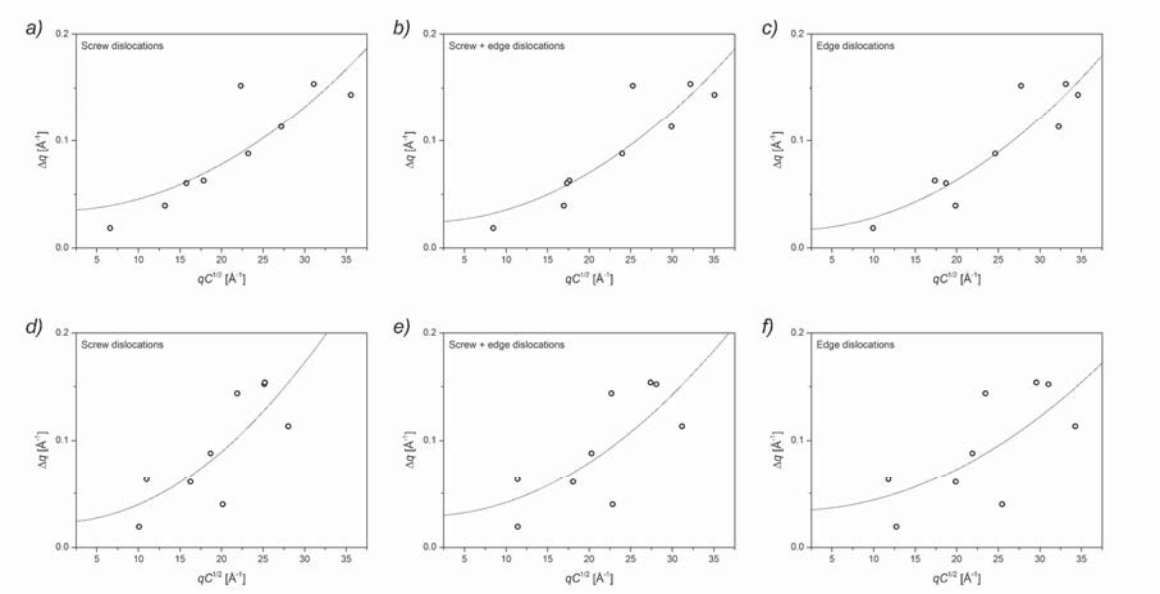

Figure 7.8: Modified Williamson-Hall plots of nitrogen expanded austenite for pure screw, pure edge and half screw and half edge dislocations with average contrast factors calculated using the elastic constants of AISI 304 austenitic stainless steel (*a-c*) and γ′-Fe_4N (*d-f*).

A smooth quadratic function is predicted for the peak widths by the modified Williamson-Hall plots (Figure 7.8), but significant deviations are observed. The best fit is obtained for pure edge dislocations using the elastic constants of austenitic stainless steel. The modified Williamson-Hall approach can be corrected for the contributions to peak broadening from stacking faults (Ungár *et al.*, 1998), but an appreciable improvement of the plots was not obtained in the present case. The deviations from a smooth quadratic curve suggest that additional factors beyond dislocations and stacking faults contribute to the broadening of diffraction peaks for expanded austenite. In addition, no tenable explanation has so far been obtained for the observed *hkl*-dependent peak shifts.

7.2.1 Misfit, internal strain and mosaicity

Although a satisfactory structural model has yet to be found, there are definite systematic trends in the directions of the *hkl*-dependent peak shifts (see e.g. Figure 7.7). This can be clearly shown by calculating an effective cubic lattice parameter for each peak position and comparing it to the average obtained value (Figure 7.9), which reveals the nature of the apparent anisotropic expansion.

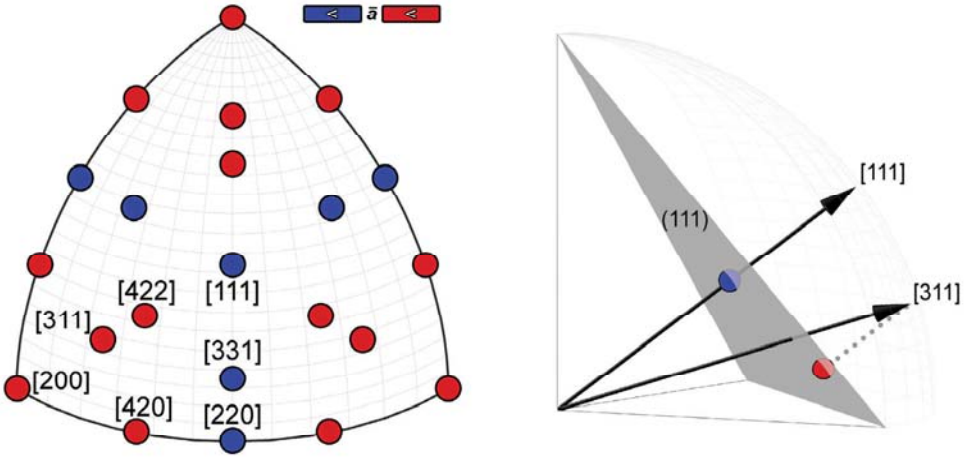

Figure 7.9: Projection of unit vectors of crystallographic directions down [111] on the (111) plane with the corresponding effective cubic lattice parameters below (blue) and above (red) the average value (left) and schematic depiction of the projection (right). The points denoted [111] and [200] refer to the pairs of reflections 111/222 and 200/400, respectively, for which the effective lattice parameters are both either below or above average (but not necessarily by an equal amount cf. Figure 7.7).

Diagonal directions like <111> and <110> are seemingly expanded less than <100> and related directions, which strongly suggests that the *hkl*-dependent peak shifts are related to elastic anisotropy of the f.c.c. structure. In addition, it is noted that 111 and 222 reflections are broadened to a lesser extent than other diffraction peaks (Figure 7.5). Anisotropic peak shifts are expected from compressive stresses arising for an expanded austenite zone constrained by an underlying austenitic stainless steel matrix (Christiansen *et al.*, 2010). The present fully nitrided sample is, however, not subject to such a constraint and residual stresses should thus be absent.

It is conceivable that internal stresses build up during formation of expanded austenite when a concentration gradient is present. These may be accommodated elastically or cause plastic deformations. Increased mosaicity, i.e. misorientation due to slip and associated rotation, has been reported for expanded austenite formed on single crystals (Rivière *et al.*, 2007). This could explain the observed apparent reduction in size of coherently diffracting domains on formation of expanded austenite (see Figure B.2, Appendix B.1) and the mosaic blocks are likely rotated to accommodate the anisotropic strains. This would explain why a simple reduction in symmetry, from proposed tetragonal to triclinic lattices has failed in describing obtained diffractograms.

Alternative, or perhaps complimentary, considerations involve misfit strains from precipitate platelets, which can cause displacement of diffraction peak positions (Bor *et al.*, 1997, 2002). Guinier-Preston (GP)-zone disc-shaped precipitates in a Cu-based alloy have

been found to cause broadening and shifts of diffraction peak components qualitatively similar to what is observed for expanded austenite, i.e. a large effect on 200 and 400 peaks while 111 and 222 peaks are relatively unaffected (Kužel *et al.*, 1997). Planar clusters of MN (M = Cr, Fe) precipitates have been observed for expanded austenite produced by low temperature plasma nitriding (Martinavičius *et al.*, 2015), but the long treatment time (30 hours) also produced a small amount of CrN near the surface, detectable by XRD.

7.3 Conclusions

Although the presence of dislocations and stacking faults in the structure of expanded austenite have been observed with transmission electron microscopy (Jiang & Meletis, 2000; Riviére *et al.*, 2002) they cannot entirely explain the observed broadening and displacement of X-ray diffraction peaks. Even for homogeneous samples not constrained by an underlying austenitic stainless steel matrix, the *hkl*-dependent peak shifts are seemingly caused by the elastic anisotropy of the f.c.c. structure. The apparent anisotropic expansion caused by incorporation of large amounts of interstitial atoms results in strains deviating from cubic symmetry.

Previous results relying on the stacking fault model primarily fitted to the 111 and 200 diffraction peaks and the results obtained in Chapter 6 can still be considered valid with respect to the obtained cubic lattice parameters. The *hkl*-dependent peak shifts should, however, not be interpreted in terms of stacking faults. The obtained values of stacking fault probabilities should rather be considered as a measure of the anisotropic strains, which currently lacks an exact quantitative interpretation. Elastic strains cannot completely describe diffraction data for expanded austenite since the shifts of 200 and 400 reflections are not equal.

Possible anisotropic effects on the crystal structure due to variations in magnetic properties with interstitial content (Section 6.4) should also be considered. Peak shifts are generally evident to a lesser extent for low interstitial contents, for which expanded austenite is paramagnetic. Other effects than magnetic anisotropy must, however, be present since considerable peak shifts are observed for both intermediate (ferromagnetic) and high (paramagnetic) nitrogen contents.

In order to obtain a satisfactory structural model for expanded austenite, which describes both potential short and long range order of nitrogen and/or carbon as well as elastic properties, first principles models should be considered. Direct comparison with experimental data may, however, be difficult since these include the effects of the large number of crystallographic defects, which seem to be an integral part of the structure. Future experimental work should, if possible, focus on reciprocal space mapping of

homogeneous single crystals of expanded austenite avoiding the influences of concentration gradients and residual compressive stresses, which are present in current single crystal work (Rivière *et al.*, 2007).

Chapter 8

Conclusions and outlook

The present work was motivated by the currently incomplete available descriptions of nitriding and nitrocarburizing processes, both in terms of the governing kinetics and thermodynamics, as well as the resulting crystal structures and magnetic properties. Kinetic information was not evaluated but phase compositions developed in applied atmospheres of controlled nitriding and carburizing potentials (activities of nitrogen and carbon) were investigated. Thermal decomposition, i.e. phase stabilities at elevated temperatures, was examined in inert atmospheres. Coefficients of thermal expansion were evaluated since these are needed to correctly predict development of thermally induced residual stresses. The interplay between magnetic and structural properties was examined for certain structures.

A method for preparing homogeneous samples of iron carbides and (carbo)nitrides with controlled nitriding and carburizing potentials was presented. The process involves a pretreatment for preparing porous iron foils and allows construction of a phase stability diagram for the Fe-N-C system. Thermal decomposition sequences for iron carbides and carbonitrides were established. Different thermal expansion coefficients were found for the paramagnetic and ferromagnetic states of cementite, while no such dependence was evident for Hägg carbide.

Partial substitution of nitrogen by carbon in ε-iron nitride affects both magnetic and structural properties. Trends in magnetic properties include increasing Curie temperatures and specific magnetization. Changes in interstitial ordering were deduced from the

observed effects on lattice parameters and related to relatively favorable interactions between nitrogen and carbon. The effects of interstitial ordering were also apparent for the anisotropic thermal expansion. The low X-ray scattering power of nitrogen and carbon necessitated the use of neutron diffraction for correct assignment of the space group for the ε-carbonitrides. These are described in space group $P\bar{3}1m$ as opposed to $P6_322$ for the pure nitrides. Individual components identified in Mössbauer spectra, particularly those corresponding to iron atoms surrounded by three nitrogen or carbon atoms, should be interpreted as an approximation for the distribution in hyperfine fields caused by the configuration of interstitial atoms. Additional components were not observed on introduction of carbon in the ε-nitrides, i.e. iron atoms preferentially surrounded by either nitrogen or carbon, if present, could not be resolved. The substitution of nitrogen by carbon causes increased hyperfine fields and decreased isomer shifts compared to fitted components for the pure nitrides.

Thermal decomposition of expanded austenite with high nitrogen content leads to development of CrN and a transitional phase corresponding to the composition M_4N. For low nitrogen content, CrN forms along with ferrite, and decomposition of carbon expanded austenite leads to initial formation of Hägg carbide, M_5C_2, followed by M_7C_3. At room temperature, expanded austenite is paramagnetic for high and low nitrogen contents but ferromagnetic for intermediate contents. Spontaneous volume magnetostriction in the ferromagnetic state causes an anomalous variation in thermal expansion coefficients with interstitial content. The increased volume due to magnetic ordering explains why the previously reported relation between lattice parameter and interstitial content for homogeneous samples of nitrogen expanded austenite does not include the value for the untreated (paramagnetic) steel at $y_N = 0$. The reported relation for carbon expanded austenite does include this value, which is consistent with a lower solubility of carbon compared to nitrogen, resulting in insufficient expansion of the lattice to induce a ferromagnetic transition. The effects of stacking faults on *hkl*-dependent shifts of Bragg reflections were included in the evaluation of diffraction data. There are significant deficiencies in the simple stacking fault model but no entirely acceptable and implementable structural description is currently available.

Dislocations and stacking faults are present in the structure of expanded austenite but cannot entirely explain the observed broadening and displacement of X-ray diffraction peaks. This was verified by comparison of experimental data with Debye simulations of faulted crystal structures and with so-called modified Williamson-Hall plots. Peak shifts are seemingly caused by the elastic anisotropy of the f.c.c. structure and may also be affected by magnetic anisotropy. The apparent deviations from cubic symmetry currently lack an exact quantitative interpretation. In order to obtain a satisfactory structural description, first

principles models should be considered for future work. Debye simulations of structural models including crystallographic defects and anisotropic effects on lattice parameters, may also aid in the understanding of experimentally obtained diffraction data.

Future experimental efforts should focus on examining the trends in magnetic properties for additional compositions of expanded austenite than the four considered here. Compositions around the paramagnetic to ferromagnetic transition induced by lattice expansion are of particular interest. The variation in lattice parameter with temperature, i.e. coefficients of thermal expansion, for these compositions should be studied with *in situ* X-ray diffraction. Forced magnetostriction could additionally be studied with X-ray diffraction in applied magnetic fields. If possible, reciprocal space mapping of homogeneous single crystals should be considered for further clarifications on the crystal structure. Additionally, neutron diffraction can be used for determination of interstitial ordering if sufficient homogeneous material can be synthesized.

As a final note, plenty of research, both from modelling and experimental approaches, is still needed in order to fully understand, and thereby be able to optimize, nitriding and nitrocarburizing processes. The present work has provided relevant new insights, adding to the collective knowledge of interstitial solid solutions of nitrogen and carbon in iron-based lattices.

Bibliography

Angelini, A., Burdese, A., & DeBenedetti, B. (1988). *Met. Sci. Technol*. **6**, 33–39.

Babu, S. S., Specht, E. D., David, S. A., Karapetrova, E., Zschack, P., Peet, M., & Bhadeshia, H. K. D. H. (2005). *Metall. Mater. Trans. A*. **36**, 3281–3289.

Balijepalli, S. K., Donnini, R., Kaciulis, S., Montanari, R., & Varone, A. (2013). *Mater. Sci. Forum*. **762**, 183–188.

Basinski, Z. S., Hume-Rothery, W., & Sutton, A. L. (1955). *Proc. R. Soc. A*. **229**, 459–467.

Blancá, E. L. P. Y., Desimoni, J., Christensen, N. E., Emmerich, H., & Cottenier, S. (2009). *Phys. Status Solidi B*. **246**, 909–928.

Bor, T. C., Delhez, R., Mittemeijer, E. J., & Van der Giessen, E. (1997). *Mater. Sci. Eng. A*. **234-236**, 896–899.

Bor, T. C., Kempen, A. T. W., Tichelaar, F. D., Mittemeijer, E. J., & Van der Giessen, E. (2002). *Philos. Mag. A*. **82**, 971–1001.

Bouchard, R. J., Frederick, C. G., & Johnson, V. (1974). *J. Appl. Phys.* **45**, 4067–4070.

Bouchaud, J. P. & Fruchart, R. (1964). *C.R. Acad. Sci.* **259**, 160–161.

Bragg, W. L. (1913). *Proc. Cambridge Phil. Soc.* **17**, 43–57.

Bundy, F. P. (1965). *J. Appl. Phys.* **36**, 616–620.

Caglioti, G., Paoletti, A., & Ricci, F. P. (1958). *Nucl. Instrum.* **3**, 223–228.

Cerenius, Y., Ståhl, K., Svensson, L. A, Ursby, T., Oskarsson, a, Albertsson, J., & Liljas, a (2000). *J. Synchrotron Rad.* **7**, 203–208.

Chen, G. M., Jaggi, N. K., Butt, J. B., Yeh, E. B., & Schwartz, L. H. (1983). *J. Phys. Chem.* **87**, 5326–5332.

Christiansen, T. L., Hummelshøj, T. S., & Somers, M. A. J. (2010). *Surf. Eng.* **26**, 242–247.

Christiansen, T. L., Hummelshøj, T. S., & Somers, M. A. J. (2011). *Surf. Eng.* **27**, 602–608.

Christiansen, T. L. & Somers, M. A. J. (2009). *Int. J. Mater. Res.* **100**, 1361–1377.

Christiansen, T. & Somers, M. A. J. (2004). *Scr. Mater.* **50**, 35–37.

Christiansen, T. & Somers, M. A. J. (2005). *Surf. Eng.* **21**, 445–455.

Christiansen, T. & Somers, M. A. J. (2006a). *Metall. Mater. Trans. A*. **37**, 675–682.

Christiansen, T. & Somers, M. A. J. (2006b). *Z. Metallkd.* **97**, 79–88.

Cook, D. C. (1987). *Metall. Trans. A*. **18**, 201–210.

Debye, P. (1915). *Ann. Phys.* **46**, 809–823.

Dong, H. (2010). *Int. Mater. Rev.* **55**, 65–98.

Eckström, H. C. & Adcock, W. A. (1950). *J. Am. Chem. Soc.* **72**, 1042–1043.

Eickel, K. H. & Pitsch, W. (1970). *Phys. Status Solidi*. **39**, 121–129.

Ernst, F., Cao, Y., & Michal, G. M. (2004). *Acta Mater.* **52**, 1469–1477.

Fabian, K., Shcherbakov, V. P., & McEnroe, S. A. (2013). *Geochem. Geophy. Geosy.* **14**, 947–961.

Fall, I. & Génin, J. M. R. (1991). *Hyperfine Interact.* **69**, 513–516.

Fang, C. M., van Huis, M. A., & Zandbergen, H. W. (2009). *Phys. Rev. B*. **80**, 224108.

Fang, H. N., Zhang, R., Liu, B., Tao, Z. K., Xiao, M. W., Wang, X. F., Xie, Z. L., Xiu, X. Q., & Zheng, Y. D. (2013). *AIP Adv.* **3**, 072136.1–9.

Fasiska, E. J. & Jeffrey, G. A. (1965). *Acta Crystallogr.* **19**, 463–471.

Fei, Y. (1995). *AGU Reference Shelf 2: Mineral Physics and Crystallography*, pp. 29–44. Washington, DC: AGU.

Fewell, M. P., Mitchell, D. R. G., Priest, J. M., Short, K. T., & Collins, G. A. (2000). *Surf. Coatings Technol.* **131**, 300–306.

Fewell, M. P. & Priest, J. M. (2008). *Surf. Coatings Technol.* **202**, 1802–1815.

Firrao, D., DeBenedetti, B., & Rosso, M. (1979). *Met. Ital.* **71**, 373–381.

Flansburg, L. D. & Hershkowitz, N. (1970). *J. Appl. Phys.* **41**, 4082–4086.

Fossati, A., Borgioli, F., Galvanetto, E., & Bacci, T. (2006). *Corros. Sci.* **48**, 1513–1527.

Frandsen, R. B., Christiansen, T., & Somers, M. A. J. (2006). *Surf. Coatings Technol.* **200**, 5160–5169.

Fruchart, R. & Rouault, A. (1969). *Ann. Chim. (Paris)*. **4**, 143–145.

Fry, A. (1923). *Stahl Eisen*. **43**, 1271–1279.

García Molleja, J., Milanese, M., Piccoli, M., Moroso, R., Niedbalski, J., Nosei, L., Bürgi, J., Bemporad, E., & Feugeas, J. (2013). *Surf. Coatings Technol.* **218**, 142–151.

Grabke, H. J. (1968a). *Ber. Bunsenges. Phys. Chem.* **72**, 541–548.

Grabke, H. J. (1968b). *Ber. Bunsenges. Phys. Chem.* **72**, 533–541.

Gressmann, T., Wohlschlögel, M., Shang, S., Welzel, U., Leineweber, A., Mittemeijer, E. J., & Liu, Z. K. (2007). *Acta Mater.* **55**, 5833–5843.

Gütlich, P., Bill, E., & Trautwein, A. X. (2011). *Mössbauer Spectroscopy and Transition Metal Chemistry*, Berlin Heidelberg: Springer.

Hayase, M., Shiga, M., & Nakamura, Y. (1973). *J. Phys. Soc. Japan*. **34**, 925–933.

Herbstein, F. H. & Snyman, J. A. (1964). *Inorg. Chem.* **6**, 894–896.

Hillert, M. & Jarl, M. (1977). *Acta Metall.* **25**, 1–9.

Hofer, L. J. E. (1966). *U.S. Bureau of Mines Bulletin*. **631**, 1–60.

Howard, C. J. & Hill, R. J. (1986). *AAEC (now ANSTO) Rep. M112*. Lucas Heights Research Laboratory, Australia.

Huang, W. J., Sun, R., Tao, J., Menard, L. D., Nuzzo, R. G., & Zuo, J. M. (2008). *Nat. Mater.* **7**, 308–313.

Hummelshøj, T. S., Christiansen, T. L., & Somers, M. A. J. (2010). *Scr. Mater.* **63**, 761–763.

Jack, D. H. & Jack, K. H. (1973). *Mater. Sci. Eng.* **11**, 1–27.

Jack, K. H. (1948a). *Proc. R. Soc. A*. **195**, 34–40.

Jack, K. H. (1948b). *Proc. R. Soc. A*. **195**, 41–55.

Jack, K. H. (1951a). *Proc. R. Soc. A*. **208**, 200–215.

Jack, K. H. (1951b). *Proc. R. Soc. A*. **208**, 216–224.

Jack, K. H. (1952). *Acta Crystallogr.* **5**, 404–411.

Jiang, J. C. & Meletis, E. I. (2000). *J. Appl. Phys.* **88**, 4026–4031.

Kano, M., Nakagawa, T., Yamamoto, T. A., & Katsura, M. (2001). *J. Alloys Compd.* **327**, 43–46.

Keune, W., Ezawa, T., Macedo, W. A. A., Glos, U., Schletz, K. P., & Kirschbaum, U. (1989). *Phys. B Condens. Matter*. **161**, 269–275.

Kjeldsen, D. B. (2013). *M.Sc. Thesis.* Technical University of Denmark.

Kooi, B. J., Somers, M. A. J., & Mittenmeijer, E. J. (1994). *Metall. Mater. Trans. A*. **25**, 2797–2814.

Kowalski, M. (1985). *J. Appl. Cryst.* **18**, 430–435.

Kužel, R., He, B., & Houska, C. R. (1997). *J. Mater. Sci.* **32**, 2451–2467.

Ledbetter, H. M. (1981). *J. Appl. Phys.* **52**, 1587–1589.

Ledbetter, H. M. (1984). *Phys. Status Solidi A*. **85**, 89–96.

Lehrer, E. (1930). *Z. Elektrochem.* **36**, 383–392.

Leineweber, A. (2007). *Acta Mater.* **55**, 6651–6658.

Leineweber, A. & Jacobs, H. (2000). *J. Alloys Compd.* **308**, 178–188.

Leineweber, A., Jacobs, H., Hüning, F., Lueken, H., & Kockelmann, W. (2001). *J. Alloys Compd.* **316**, 21–38.

Leineweber, A., Jacobs, H., Hüning, F., Lueken, H., Schilder, H., & Kockelmann, W. (1999). *J. Alloys Compd.* **288**, 79–87.

Leineweber, A., Jacobs, H., Kockelmann, W., Hull, S., & Hinz-Hübner, D. (2004). *J. Alloys Compd.* **384**, 1–5.

Leineweber, A., Shang, S., Liu, Z.-K., Widenmeyer, M., & Niewa, R. (2012). *Z. Kristallogr.* **227**, 207–220.

Li, C. X. & Bell, T. (2004). *Corros. Sci.* **46**, 1527–1547.

Li, X.-Y., Sun, Y., & Bell, T. (1999). *Z. Metallkd.* **90**, 901–907.

Liapina, T., Leineweber, A., Mittemeijer, E. J., & Kockelmann, W. (2004). *Acta Mater.* **52**, 173–180.

Liu, Z. Q., Leineweber, A., Mittemeijer, E. J., Mitsuishi, K., & Furuya, K. (2006). *J. Mater. Res.* **21**, 2572–2581.

Machlet, A. (1913). U.S. Patent 1,065,379.

Martinavičius, A., Abrasonis, G., Scheinost, A. C., Danoix, R., Danoix, F., Stinville, J. C., Talut, G., Templier, C., Liedke, O., Gemming, S., & Möller, W. (2012). *Acta Mater.* **60**, 4065–4076.

Martinavičius, A., Danoix, R., Drouet, M., Templier, C., Hannoyer, B., & Danoix, F. (2015). *Mater. Lett.* **139**, 153–156.

Massalski, T. B. (1996). *Binary Alloy Phase Diagrams*, 2nd editon: ASM International.

Menéndez, E., Templier, C., Garcia-Ramirez, P., Santiso, J., Vantomme, A., Temst, K., & Nogués, J. (2013). *ACS Appl. Mater. Interfaces*. **5**, 10118–10126.

Mittemeijer, E. J. (2010). *Fundamentals of Materials Science*, pp. 404–409. Berlin Heidelberg: Springer.

Mittemeijer, E. J. (2013). *ASM Handbook, Volume 4A: Steel Heat Treating Fundamentals and Processes*, pp. 619–646. ASM International.

Mittemeijer, E. J. & Slycke, J. T. (1996). *Surf. Eng.* **12**, 152–162.

Moruzzi, V. L., Marcus, P. M., Schwarz, K., & Mohn, P. (1986). *Phys. Rev. B*. **34**, 1784–1791.

Mössbauer, R. L. (1958). *Z. Phys.* **151**, 124–143.

Mössbauer, R. L. (1959). *Z. Naturforsch.* **14**, 211–216.

Naumann, F. K. & Langenscheid, G. L. (1965a). *Arch. Eisenhüttenwes.* **36**, 583–590.

Naumann, F. K. & Langenscheid, G. L. (1965b). *Arch. Eisenhüttenwes.* **36**, 677–682.

Nozik, A. J., Wood, J. C., & Haacke, G. (1969). *Solid State Commun.* **7**, 1677–1679.

Oda, K., Umezus, K., & Ino, H. (1990). *J. Phys. Condens. Matter*. **2**, 10147–10158.

Oddershede, J. (2007). *PhD Thesis.* Technical University of Denmark.

Oddershede, J., Christiansen, T. L., & Ståhl, K. (2008a). *J. Appl. Cryst.* **41**, 537–543.

Oddershede, J., Christiansen, T. L., Ståhl, K., & Somers, M. A. J. (2008b). *J. Mater. Sci.* **43**, 5358–5367.

Oddershede, J., Christiansen, T. L., Ståhl, K., & Somers, M. A. J. (2010). *Scr. Mater.* **62**, 290–293.

Parthé, E. & Yvon, K. (1970). *Acta Crystallogr. B*. **26**, 153–163.

Pedersen, H., Christiansen, T. L., & Somers, M. A. J. (2011). *HTM J. Heat Treatm. Mat.* **66**, 76–81.

Pekelharing, M. I., Böttger, A., Somers, M. A. J., Steenvoorden, M. P., van der Kraan, A. M., & Mittemeijer, E. J. (1999). *Mater. Sci. Forum*. **318-320**, 115–120.

Pepperhoff, W. & Acet, M. (2001). *Constitution and Magnetism of Iron and Its Alloys*, pp. 104–115. Berlin Heidelberg: Springer.

du Plessis, H. E., de Villiers, J. P. R., & Kruger, G. J. (2007). *Z. Kristallogr.* **222**, 211–217.

Price, S. W. T., Zonias, N., Skylaris, C.-K., Hyde, T. I., Ravel, B., & Russell, A. E. (2012). *Phys. Rev. B*. **85**, 075439.

Read, W. T. (1953). *Dislocations in Crystals*, pp. 92–113. New York: McGraw-Hill.

Rietveld, H. M. (1967). *Acta Crystallogr.* **22**, 151–152.

Rietveld, H. M. (1969). *J. Appl. Cryst.* **2**, 65–71.

Riviére, J. P., Meheust, P., Villain, J. P., Templier, C., Cahoreau, M., Abrasonis, G., & Pranevicius, L. (2002). *Surf. Coatings Technol.* **158-159**, 99–104.

Rivière, J. P., Templier, C., Declémy, A., Redjdal, O., Chumlyakov, Y., & Abrasonis, G. (2007). *Surf. Coatings Technol.* **201**, 8210–8214.

Robbins, M. & White, J. G. (1964). *J. Phys. Chem. Solids*. **25**, 717–720.

Rouault, A., Herpin, P., & Fruchart, R. (1970). *Ann. Chim. (Paris)*. **5**, 461–470.

Sas, W. H. & de Wolff, P. M. (1966). *Acta Crystallogr.* **21**, 826–827.

Schneider, A. & Inden, G. (2001). *Steel Res.* **72**, 503–507.

Sears, V. F. (1992). *Neutron News*. **3**, 26–37.

Shang, S., Böttger, A. J., Steenvoorden, M. P., & Crajé, M. W. J. (2006). *Acta Mater.* **54**, 2407–2417.

Shirane, G., Takei, W. J., & Ruby, S. L. (1962). *Phys. Rev.* **126**, 49–52.

Sifkovits, M., Smolinski, H., Hellwig, S., & Weber, W. (1999). *J. Magn. Magn. Mater.* **204**, 191–198.

Somers, M. A. J. (2014). *Comprehensive Materials Processing Vol. 12*, pp. 413–437. Elsevier Ltd.

Somers, M. A. J., Kooi, B. J., Maldzinski, L., Mittemeijer, E. J., van der Horst, A. A., van der Kraan, A. M., & van der Pers, N. M. (1997). *Acta Mater.* **45**, 2013–2025.

Somers, M. A. J., Lankreijer, R. M., & Mittemeijer, E. J. (1989a). *Philos. Mag. A*. **59**, 353–378.

Somers, M. A. J., van der Pers, N. M., Schalkoord, D., & Mittemeijer, E. J. (1989b). *Metall. Mater. Trans. A*. **20**, 1533–1539.

Stróz, D. & Psoda, M. (2010). *J. Microsc.* **237**, 227–231.

Sun, Y., Li, X. Y., & Bell, T. (1999). *J. Mater. Sci.* **34**, 4793–4802.

Takahashi, T., Burghaus, J., Music, D., Dronskowski, R., & Schneider, J. M. (2012). *Acta Mater.* **60**, 2054–2060.

Tromas, C., Stinville, J. C., Templier, C., & Villechaise, P. (2012). *Acta Mater.* **60**, 1965–1973.

Tsuzuki, A., Sago, S., Hirano, S., & Naka, S. (1984). *J. Mater. Sci.* **19**, 2513–2518.

Ungár, T. & Borbély, A. (1996). *Appl. Phys. Lett.* **69**, 3173–3175.

Ungár, T., Dragomir, I., Révész, Á., & Borbély, A. (1999). *J. Appl. Cryst.* **32**, 992–1002.

Ungár, T., Gubicza, J., Hanák, P., & Alexandrov, I. (2001). *Mater. Sci. Eng. A*. **319-321**, 274–278.

Ungár, T., Ott, S., Sanders, P. G., Borbély, A, & Weertman, J. R. (1998). *Acta Mater.* **46**, 3693–3699.

Velterop, L., Delhez, R., de Keijser, T. H., Mittemeijer, E. J., & Reefman, D. (2000). *J. Appl. Cryst.* **33**, 296–306.

Wang, C. S., Klein, B. M., & Krakauer, H. (1985). *Phys. Rev. Lett.* **54**, 1852–1855.

Warren, B. E. (1963). *J. Appl. Phys.* **34**, 1973–1975.

Warren, B. E. (1969). *X-Ray Diffraction*, pp. 275–298. Massachusetts: Addison-Wesley.

Wertheim, G. K., Butler, M. A., West, K. W., & Buchanan, D. N. E. (1974). *Rev. Sci. Intrum.* **45**, 1369–1371.

Westgren, A. (1935). *Jernkontorets Ann.* **118**, 231–240.

Willis, R. F., Bland, J. A. C., & Schwarzacher, W. (1988). *J. Appl. Phys.* **63**, 4051–4056.

Wimpory, R. C., Mikula, P., Šaroun, J., Poeste, T., Li, J., Hofmann, M., & Schneider, R. (2008). *Neutron News*. **19**, 16–19.

Wood, I. G., Vočadlo, L., Knight, K. S., Dobson, D. P., Marshall, W. G., Price, G. D., & Brodholt, J. (2004). *J. Appl. Cryst.* **37**, 82–90.

Xiaolei, X., Liang, W., Zhiwei, Y., & Zukun, H. (2005). *Surf. Coatings Technol.* **192**, 220–224.

Xu, X., Wang, L., Yu, Z., Qiang, J., & Hei, Z. (2000). *Metall. Mater. Trans. A*. **31**, 1193–1199.

Young, R. A. (1993). *The Rietveld Method*, Oxford: IUCr/Oxford University Press.

Öztürk, O. & Williamson, D. L. (1995). *J. Appl. Phys.* **77**, 3839–3850.

Öztürk, O. & Williamson, D. L. (2002). *Surf. Coatings Technol.* **158-159**, 288–294.

Appendices

Appendix A

Publications

A.1 Thermal expansion and phase transformations of nitrogen-expanded austenite studied with *in situ* synchrotron X-ray diffraction

Bastian Brink, Kenny Ståhl, Thomas L. Christiansen & Marcel A. J. Somers
J. Appl. Cryst. (2014). **47**, 819–826

Journal of
Applied Crystallography
ISSN 1600-5767

Received 2 October 2013
Accepted 6 March 2014

Thermal expansion and phase transformations of nitrogen-expanded austenite studied with *in situ* synchrotron X-ray diffraction

Bastian Brink,[a]* Kenny Ståhl,[b] Thomas L. Christiansen[a] and Marcel A. J. Somers[a]

[a]Department of Mechanical Engineering, Technical University of Denmark, Produktionstorvet B425, Kongens Lyngby, DK-2800, Denmark, and [b]Department of Chemistry, Technical University of Denmark, Kemitorvet B206, Kongens Lyngby, DK-2800, Denmark. Correspondence e-mail: basbr@mek.dtu.dk

Nitrogen-expanded austenite, γ_N, with high and low nitrogen contents was produced from AISI 316 grade stainless steel powder by gaseous nitriding in ammonia/hydrogen gas mixtures. *In situ* synchrotron X-ray diffraction was applied to investigate the thermal expansion and thermal stability of expanded austenite in the temperature range 385–920 K. Evaluation of the diffractograms of the sample with a high nitrogen content, corresponding to an occupancy of the interstitial lattice of 56%, with Rietveld refinement yielded a best convergence after including the stacking fault probability as a fitting parameter. The stacking fault density is constant for temperatures up to 680 K, whereafter it decreases to nil. Surprisingly, a transition phase with composition M_4N (M = Fe, Cr, Ni, Mo) appears for temperatures above 770 K. The linear coefficient of thermal expansion depends on the nitrogen content and is lowest for the sample with a high level of nitrogen.

1. Introduction

Low-temperature nitriding of austenitic stainless steel introduces nitrogen into the surface-adjacent region and improves wear and fatigue performance (Christiansen & Somers, 2009; Dong, 2010). The surface hardness can be increased by an order of magnitude (Christiansen & Somers, 2005), while corrosion resistance is retained and may even be improved by the process (Fossati *et al.*, 2006; Li & Bell, 2004). At temperatures below approximately 720 K, a solid solution of nitrogen forms in the nitrided zone containing 17–38 at.% N, corresponding to an occupancy of the interstitial f.c.c. (face-centred cubic) sublattice of 0.16–0.61 (Christiansen & Somers, 2006*a*). As the developing case is essentially a supersaturated solid solution of nitrogen atoms in austenite it is referred to as expanded austenite (γ_N). Extended X-ray absorption fine-structure (EXAFS) studies have shown that Fe, Cr and Ni exist in different local environments in expanded austenite (Oddershede *et al.*, 2008*a*, 2010). Short-range ordering of N and Cr occurs. The majority of Cr atoms have a first coordination shell with a bond length shorter than, but in the vicinity of, the chemical compound CrN, and the coordination number of Cr is maximally 5, while no X-ray diffraction (XRD) indications of CrN development were found (Oddershede *et al.*, 2010). Martinavičius *et al.* (2012) found a coordination number of 5.7 and using field ion microscopy they observed precipitates preferentially at grain boundaries ascribed to CrN, which were not detectable with XRD. The authors suggested for their samples, produced by plasma-assisted nitriding, that the expanded austenite structure consists of nanometric CrN precipitates embedded in an Fe_4N-like matrix. Whether these observations can be transferred to expanded austenite synthesized by other methods, *e.g.* gas nitriding, is still unclear. Additionally, it has been reported that peak-width anisotropies observed in diffraction profiles can be caused by screw dislocations in the structure and that the dislocation density increases with interstitial nitrogen occupancy (Oddershede *et al.*, 2008*b*).

In assessing the crystallography of γ_N, the majority of published investigations have focused on samples of an expanded austenite zone grown into an austenite substrate rather than on homogenous samples (see, for example, Fewell & Priest, 2008). The resulting depth variation of the composition has several implications for the observed X-ray diffractograms. The compositional inhomogeneity within the investigated depth range causes asymmetric broadening and the induced macrostress gradient over the expanded austenite zone causes *hkl*-dependent shifts of the diffraction peaks (Öztürk & Williamson, 1995; Xu *et al.*, 2000; Christiansen *et al.*, 2010). Asymmetric broadening is also anticipated from texture gradients (Rivière *et al.*, 2007). Additionally, faulting of the f.c.c. lattice causes both an *hkl*-dependent shift of diffraction peaks and asymmetric broadening. In order to avoid the influences of composition-induced stresses and asymmetric broadening, homogeneous samples should thus be used.

The current investigation presents results on the thermal behaviour of expanded austenite investigated using *in situ* synchrotron XRD and Rietveld refinement. For this purpose, powder samples of expanded austenite were synthesized with

high and low nitrogen contents. A structural description similar to that described by Christiansen & Somers (2004) was used: an f.c.c. lattice with stacking faults contributing to systematic deviations of XRD peaks as described by Warren (1990). It should be noted that Warren's theory has been demonstrated to be insufficiently accurate (Velterop *et al.*, 2000), but the deviations are relatively small for the strongest f.c.c. reflections 111, 200 and 220, particularly for modest stacking fault probabilities. Since there is no entirely acceptable and implementable structural description at this point, the Warren approach is deemed sufficient in order to describe the data obtained in the present work.

The thermal stability of nitrogen-expanded austenite was previously investigated with thermogravimetry and differential thermal analysis and it was demonstrated that under an inert atmosphere it is associated with the development of molecular nitrogen gas, chromium nitride, ferrite and nitrogen-depleted austenite (Christiansen & Somers, 2006*b*). For austenitic stainless steel containing molybdenum (AISI 316L), it was hypothesized, on the basis of scarce data, that decomposition occurred by discontinuous precipitation, while for molybdenum-free stainless steel (AISI 304L), a eutectoid transformation contributed to decomposition.

2. Experimental

2.1. Sample preparation

Gaseous nitriding of 5 µm AISI 316 grade stainless steel powder (Höganäs AB), with composition from chemical analysis given in Table 1, was performed in ceramic crucibles in a Netzsch STA449 C Jupiter thermal analyzer. For nitriding ammonia, nitrogen and hydrogen of 99.999% purity were applied. A sample with a high nitrogen content was synthesized in an atmosphere of 95 vol.% NH_3 and 5 vol.% N_2 in two temperature steps: initially at 693 K for 4 h followed by 673 K for 25 h. A sample with a low nitrogen content was produced by denitriding the high-nitrogen sample at 693 K for 2 h in a gas consisting of 91 vol.% H_2 and 9 vol.% N_2. The nitrogen content in the sample was calculated from the total nitrogen uptake/release during nitriding/denitriding.

2.2. Synchrotron X-ray diffraction

Diffractograms were collected at a wavelength of λ = 1.07051 (2) Å in transmission mode with a Huber G670 Guinier camera at MAX-lab beamline I711 (Cerenius *et al.*, 2000). In order to reduce the influence of fluorescence radiation, aluminium foils were positioned between the sample and the detector. Samples were mounted in 0.7 mm-diameter quartz capillaries filled with an inert argon atmosphere to avoid oxidation and heated in a Huber 670.3 furnace. Temperature calibration and determination of the applied wavelength were performed using an Si standard. The correction for diffraction angle (2θ) zero shift was determined from the untreated reference sample.

For each sample, 26 diffractograms were measured in the temperature interval 385–920 K. Data were collected in a 2θ range of 4–100° [corresponding to a q range from 0.4 to 9.0 Å^{-1}, $q = 4\pi\sin(\theta)/\lambda$] with a fixed step size of 0.005° in 2θ and an exposure time of 240 s at each temperature step. After exposure, the temperature was immediately ramped to the next set point, and the average time for reaching and stabilizing at each set point temperature prior to exposure was 226 s. Rietveld refinements of intensity *versus* scattering angle (2θ) were carried out using the program *WINPOW*, a local variation of *LHMP* (Howard & Hill, 1986), in order to fit lattice parameters and mass fractions of the constituent phases. Pseudo-Voigt profile functions were applied together with Chebyshev background polynomials. In order to incorporate the effect of stacking faults on the peak positions of expanded austenite reflections, the equation derived by Warren (1990) was included in the Rietveld refinement. Typically, residual values of $R_p \leq 1.29$ and goodness-of-fit values $\chi^2 \leq 1.43$ were obtained.

Table 1
Chemical composition of untreated AISI 316 powder in mass%.

Fe	Cr	Ni	Mo	Mn	C	N	S
Balance	16.2	13.3	2.3	<0.2	<0.05	<0.05	<0.005

3. Results and interpretation

3.1. Nitriding

The morphology of the powder is shown on the scanning electron microscopy (SEM) micrograph in Fig. 1, which confirms a mean particle size of 5 µm. X-ray diffractograms (Fig. 2*a*) show that the untreated powder contains two phases: austenite (γ) and a significant amount of a ferritic b.c.c. (body-centred cubic) phase (α). The thermodynamic equilibrium of AISI 316 is a mixture of austenite and ferrite (Kjeldsen, 2013), but chromium-rich δ-ferrite could also have formed during solidification of the powder. The phase composition determined by Rietveld refinement (Fig. 2) is 13.7 (1) mass% α and

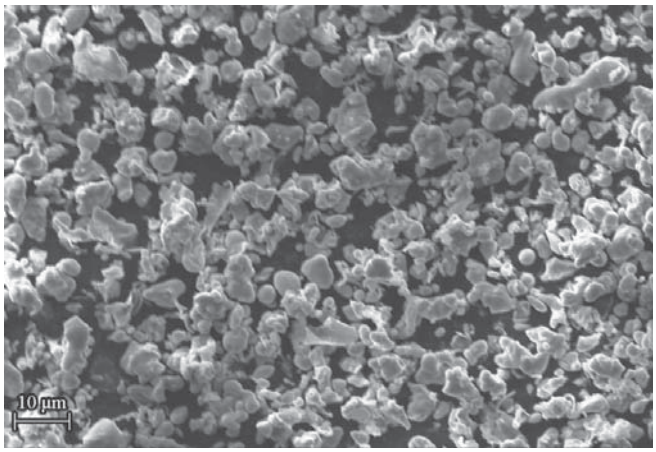

Figure 1
SEM secondary electron image showing the morphology of the AISI 316 powder; the mean particle size is 5 µm.

86.3 (1) mass% γ. In order to avoid sintering of the fine powder, it was not fully austenitized before nitriding and the presence of ferrite thus had to be tolerated.

The high-nitrogen sample was obtained by nitriding of the AISI 316 powder until a stationary weight gain was reached, suggesting an imposed equilibrium between nitrogen in the gas phase and in the stainless steel. After 29 h treatment time, all austenite was transformed and the nitrided sample consisted mainly of expanded austenite (Fig. 2*b*). Previous investigations on precipitation hardening stainless steel have shown that nitriding of b.c.c. phases leads to a tetragonal distortion followed by transformation to γ_N for sufficiently high nitrogen activities owing to the austenite-stabilizing effects of N (Frandsen *et al.*, 2006). This effect is not immediately apparent from the present data since the ferritic phase is partially retained in the nitrided sample, although a slight broadening of ferrite peaks was observed. An additional broad peak is present between the 111 and 200 reflections of expanded austenite ($q = 2.99$ Å^{-1}), which cannot be explained by the α or γ_N phases. This peak is attributed to the presence of the hexagonal nitride ε-M_2N_{1-z}, with M representing the metallic composition of the AISI 316 matrix. The nitride is based on an h.c.p. (hexagonal close packed) lattice of metal atoms and a composition corresponding to $z \simeq 0.1$ is estimated from comparison with the lattice parameters reported for ε-Fe_2N_{1-z} (Somers *et al.*, 1997). No higher-order reflections from this phase are discernible, but additional diffractograms recorded to verify the identity (not shown) did indicate the presence of a 112 peak of the ε phase. Initial experiments had shown that this phase could form on prolonged nitriding of fully austenitic foil pieces at 693 K. It is likely that the nucleation of the ε phase is promoted by the large surface area on nitriding a fine powder.

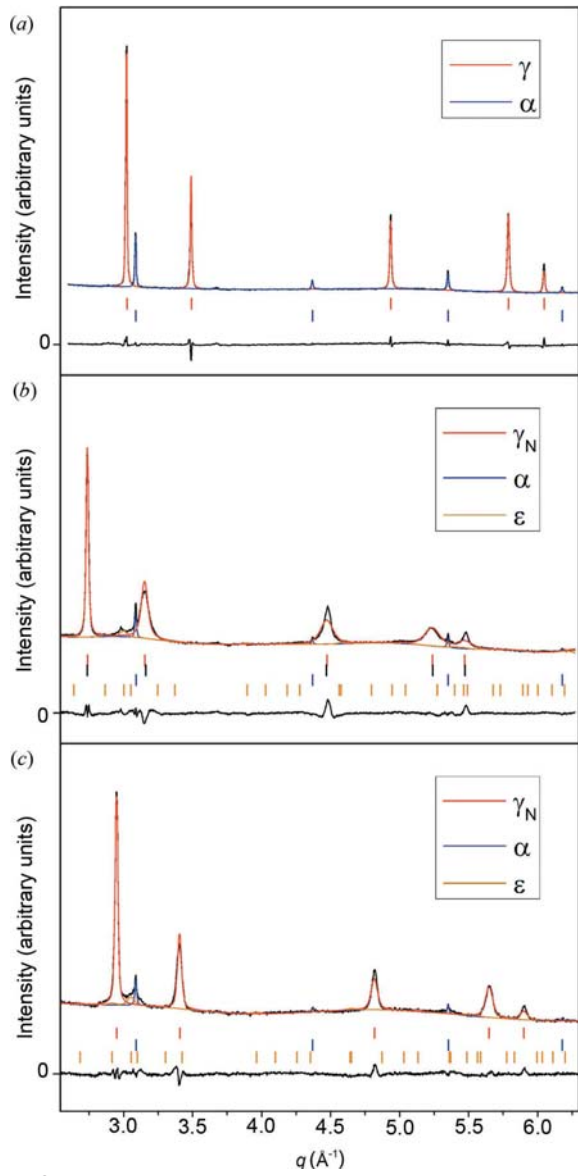

Figure 2
X-ray diffraction pattern, refined Rietveld profile and difference curve up to $q = 6.3$ Å^{-1} for (*a*) the AISI 316 reference sample, (*b*) the high-nitrogen sample and (*c*) the low-nitrogen sample. Vertical lines mark Bragg positions. Black markers in (*b*) indicate ideal unfaulted f.c.c. positions.

Two major differences are noticed between the untreated and nitrided sample: (i) diffraction peaks for expanded austenite are considerably broadened and shifted towards lower q, and (ii) the q shift is expected from the expansion of the crystal structure but the peaks do not fit ideal f.c.c. positions. The broadening may be (at least) partially explained by an inhomogeneous nitrogen distribution in the nitrided sample (Christiansen & Somers, 2005). This effect should, however, be limited as 5 µm powder was used and it is noted that no pronounced tailing of the line profiles towards high q is observed. This is in accordance with limited inhomogeneities in the nitrogen distribution, *i.e.* no concentration gradients. Therefore broadening is interpreted as a consequence of the faulted structure of expanded austenite, which is also the origin of the *hkl*-dependent displacement of the diffraction peaks from their ideal f.c.c. positions. The peak positions can be accurately described by including the stacking fault probability, α_{sf}, as a fit parameter. The systematic *hkl*-dependent deviations of XRD peaks from their ideal positions, as described by Warren (1990), were adopted for this purpose. The refinement profile does not entirely describe the observed broadening of γ_N diffraction peaks. Since these peaks are partly overlapping with peaks from α and ε phases and the contributions from screw dislocations and potential microstrain and size effects should also be taken into account, no further fitting of the broadening was attempted.

The low-nitrogen sample was denitrided in an H_2 atmosphere which retracts loosely bound interstitial nitrogen. Correspondingly, in Fig. 2(*c*) the shift of the diffraction peaks for expanded austenite to lower q is not as pronounced as in Fig. 2(*b*). The broad peak attributed to ε-M_2N_{1-z} is slightly shifted towards higher q. This further indicates that the phase has a broad homogeneity range, because the shift corresponds to a reduction in nitrogen content. The ferrite phase is still present.

The interstitial nitrogen content of γ_N can be estimated from the lattice parameter, a, of expanded austenite using the

reported relation between a and the interstitial nitrogen occupancy, y_N (Christiansen & Somers, 2006*a*). Since diffractograms were recorded starting from 385 K, it is necessary to use fitted coefficients of thermal expansion to obtain the values at room temperature. See §4.1 for a detailed discussion of how the lattice parameters evolve with temperature. For the high-nitrogen sample this yields an occupancy of $y_N = 0.56$, where y_N is the fraction of the interstitial sublattice occupied by nitrogen atoms, which, for f.c.c., is equivalent to the number of N atoms per metal atom. This corresponds to a nitrogen-to-chromium ratio (*cf.* Table 1) of 3.22, in excellent agreement with the previously reported maximum solubility in AISI 316 (Christiansen & Somers, 2006*a*).

The lattice parameter for the low-nitrogen sample is below the minimum value in the reported relation, and extrapolation is not feasible since the lattice parameter does not linearly approach that of the untreated steel. Another relation exists for low interstitial contents as reported for carbon-expanded austenite (Hummelshøj *et al.*, 2010). Using this as an approximation yields $y_N = 0.14$ which is indeed lower than the previously reported minimum solubility. This is not surprising since the Cr content in the presently applied steel is lower than the one used by Christiansen & Somers (2006*a*), and the retained nitrogen is interpreted as trapped by Cr, which has the highest affinity for N of the elements present in the sample. The nitrogen-to-chromium ratio obtained is, however, also lower than anticipated: N:Cr = 0.804 as compared to the expected minimum N:Cr = 0.891. It appears that the minimum obtainable solubility of N in homogeneous samples of expanded austenite depends on the Cr content, but is not constrained to a fixed ratio. Alternatively, the lower obtained ratio may be explained by an initial formation of δ-ferrite on solidification of the original powder. This lowers the concentration of Cr in the austenite phase, thereby limiting the nitrogen content, and leads to an underestimated calculated nitrogen-to-chromium ratio.

3.2. *In situ* diffraction

Recorded diffraction profiles as a function of temperature are given as contour plots in Fig. 3. Indexed peaks are those corresponding to (expanded) austenite (see Fig. 2 for α and ε peak positions). For the untreated sample (Fig. 3*a*), the ferrite phase transforms into austenite above 820 K, in good correspondence to Thermo-Calc results of ferrite and austenite stability in AISI 316 (Kjeldsen, 2013). At the highest investigated temperature, 920 K, the sample contains 97.1 (5) mass% austenite. As a consequence of thermal expansion of austenite and ferrite, a slight shift of the diffraction peaks towards lower q is observed with increasing temperature.

For the high-nitrogen sample the only evident change up to 700 K is thermal expansion. Above this temperature a deflation of the lattice parameter of expanded austenite, as manifested by an increase in q for γ_N reflections, is caused by a decrease in interstitial content. Above 840 K, formation of an austenite phase with lattice parameters comparable to those of the untreated sample is visible. The release of nitrogen from expanded austenite causes a gradual decrease in the lattice parameters, but the transformation of γ_N to the final austenite phase, γ, is accompanied by a discontinuity. A transitional phase, γ_T, with an intermediate lattice parameter was

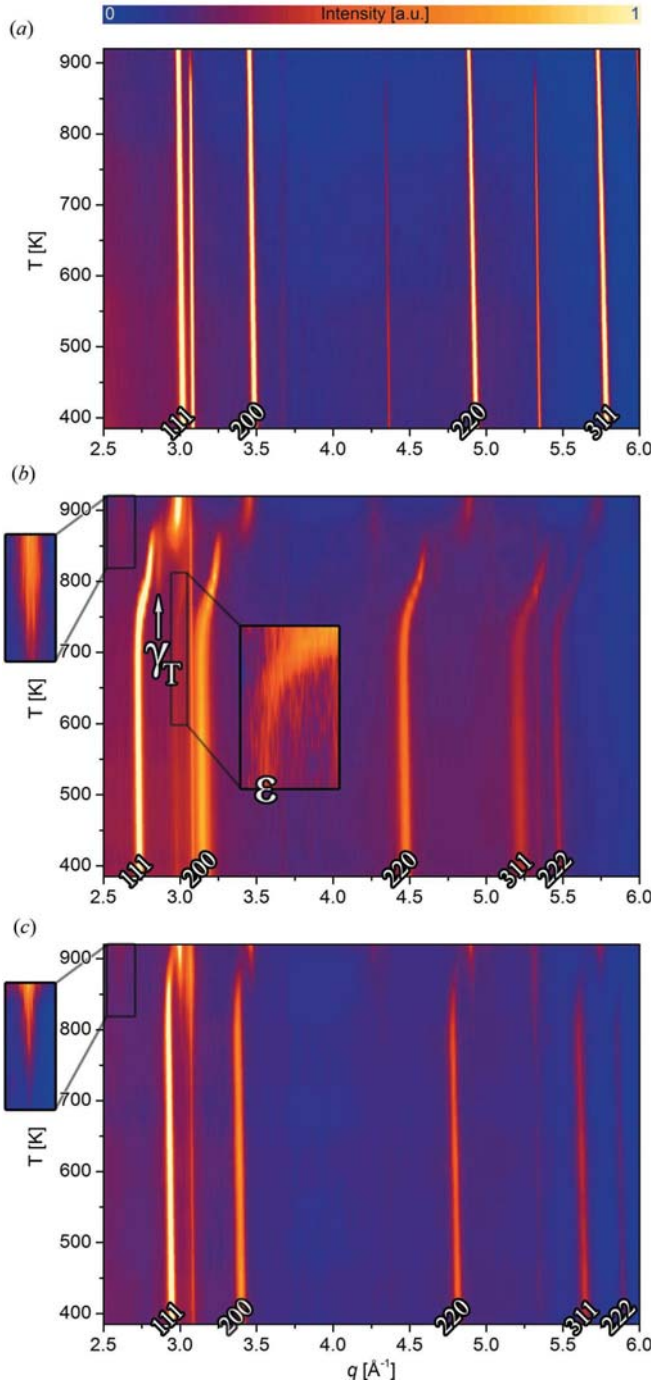

Figure 3
Contour plot of all recorded diffraction profiles up to $q = 6.0$ Å^{-1} *versus* temperature for (*a*) the AISI 316 reference sample, (*b*) the high-nitrogen sample and (*c*) the low-nitrogen sample. Indexed peaks are (expanded) austenite and the 111 peak of the γ_T phase is indicated with an arrow. Higher-order reflections are faint but visible. Intensity-rescaled inserts are added to emphasize the emerging 111 peak of CrN and the q shift of the ε 111 peak.

observed, indicated by an arrow in Fig. 3(*b*). The 111 peak of ε-M_2N_{1-z} shifts towards higher q in the same temperature range as expanded austenite and disappears beyond 900 K, indicating a nitrogen depletion of the ε phase, in accordance with the broad homogeneity range of this nitride. Formation of CrN from the decomposition of expanded austenite was detected above 750 K.

The first change in phase composition for the low-nitrogen sample is an increase in intensity of the ferrite peaks above 750 K (Fig. 3*c*). Following this, the decomposition of expanded austenite becomes apparent from the decreasing lattice parameter. Note that, unlike the high-nitrogen sample, the change in composition of the γ_N phase is negligible up to almost 850 K. The 111 peak of ε-M_2N_{1-z} shifts slightly towards higher q beyond 750 K before disappearing at 840 K. The initial formation of CrN takes place at 800 K and γ peaks are observed at 840 K.

3.3. Phase transformations

Phase transformation maps showing the refined mass fractions are given in Fig. 4. Formation of CrN from the decomposition of expanded austenite starts at 750 K and increases up to a final mass fraction of 0.177 at 920 K. The amount of ε-M_2N_{1-z} remains almost constant up to 900 K. The transitional phase, γ_T, constitutes a maximum mass fraction of 0.173 at 860 K before the amount decreases at higher temperatures. The initial total nitrogen content in the sample obtained from thermogravimetry during nitriding was 12 mass%, while the final mass fraction of CrN accounts for a total nitrogen content of 3.8 mass%. A significant amount of the dissolved nitrogen content has thus been released as N_2, in accordance with previously reported observations on annealing expanded austenite in an inert (N_2) atmosphere (Christiansen & Somers, 2006*b*).

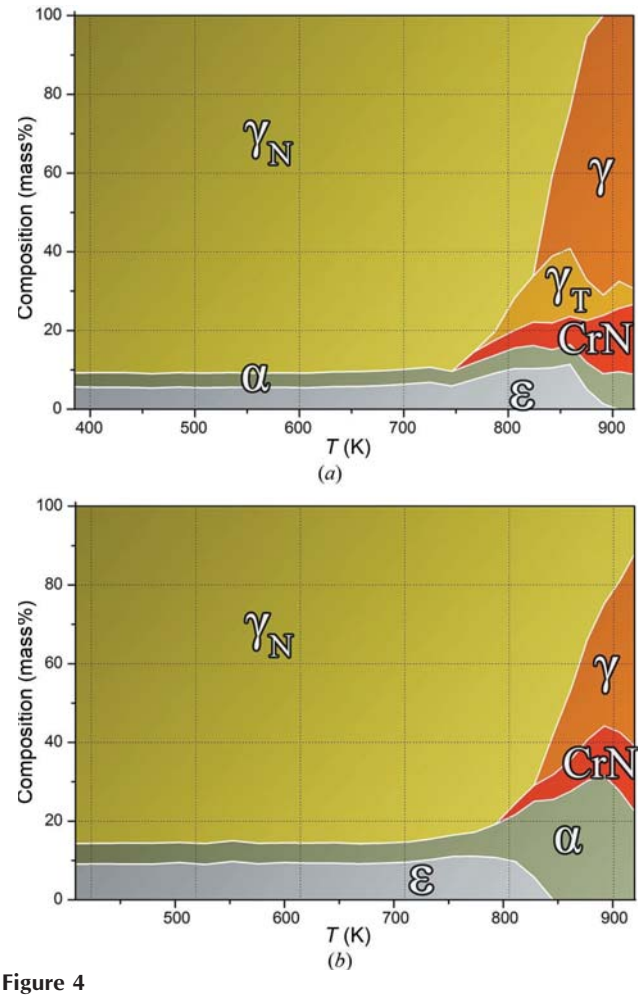

Figure 4
Phase transformation map for (*a*) the high-nitrogen sample and (*b*) the low-nitrogen sample. Estimated standard deviations from refinements are $\leq$1.8 mass%.

The first change in phase composition for the low-nitrogen sample (Fig. 4*b*) occurs at 750 K, where the amount of ferrite increases at the cost of expanded austenite. This is interpreted as the first indication of the decomposition of expanded austenite and is directly followed by development of CrN. The decrease of the lattice parameters of γ_N at 840 K coincides with decomposition of the ε phase and the formation of an austenite phase with lattice parameter comparable to that of the untreated sample. The formation of ferrite from decomposition of γ_N at temperatures below 900 K is in agreement with Thermo-Calc results of ferrite and austenite stability in AISI 316 containing nitrogen (Christiansen & Somers, 2006*b*). Above 900 K, ferrite is transformed into austenite and the final decomposition products for both samples are austenite and CrN, in good agreement with the Thermo-Calc calculations. Ferrite formation was not observed in the high-nitrogen sample, most likely as a consequence of the abundant presence of austenite-stabilizing N.

4. Discussion

4.1. Decomposition of expanded austenite

The lattice parameters obtained with Rietveld refinement for the (expanded) austenite phases in all samples as a function of temperature are presented in Fig. 5. The lattice of the reference sample expands monotonically in the entire temperature range investigated. For expanded austenite, the lattice parameters start to decrease above a certain temperature. The relatively low temperature where this is observed in the high-nitrogen sample is ascribed to N_2 formation. The release of nitrogen from expanded austenite as N_2 has been demonstrated before (Christiansen & Somers, 2006*b*) and is an immediate consequence of thermodynamically stable N_2 compared with N in solid solution (Grabke, 1968). For a high nitrogen content, the driving force for N_2 release is higher than for a low nitrogen content. For the low-nitrogen sample, the decreasing lattice parameter is caused only by CrN formation. The final mass fraction of CrN accounts for a total nitrogen content of 3.5 mass%, which is the amount that was retained after denitriding. Note that the observed stability range up to about 800 K for the low-nitrogen sample is only valid for the thermal history of the sample, *i.e.* approximately eight minutes in between measurements, and does not repre-

sent completed transformation at the various temperatures. For prolonged (isothermal) annealing, decomposition of nitrogen-expanded austenite has been reported for temperatures as low as 600 K (Li *et al.*, 1999; Öztürk & Williamson, 2002; García Molleja *et al.*, 2013).

The observation of a transitional f.c.c. phase with a value of $a \simeq 3.8$ Å in the range 770–860 K has not been reported before on the basis of X-ray diffraction. The lattice parameter value coincides with that of the ordered iron-based nitride γ'-Fe_4N with stoichiometric composition (Somers, Van Der Pers *et al.*, 1989), which matches the dependence of the lattice parameter of expanded austenite on nitrogen content (Christiansen & Somers, 2006*a*). The presence of a γ'-Fe_4N type structure has been reported on the basis of transmission electron microscopy observations of superlattice reflections, but with a reported lattice parameter larger than that of γ'-Fe_4N (Stróz & Psoda, 2010; Xiaolei *et al.*, 2005; Xu *et al.*, 2000). The present result suggests that the composition M_4N with $y_N = 0.25$ can indeed occur and may be thermodynamically favoured over expanded austenite with short-range order of the nitrogen atoms.

Initially, expanded austenite in the high-nitrogen sample has a significantly larger lattice parameter than that of the low-nitrogen sample. For both samples the lattice parameter of the developed γ phase approaches that of the reference sample after decomposition, implying that the austenite present in the samples at 900 K is essentially free of nitrogen in solid solution. Slightly lower lattice parameter values were obtained for the low-nitrogen sample as compared to the high-nitrogen sample. A slight reduction in lattice parameter is expected because of chromium depletion of the austenitic matrix (Babu *et al.*, 2005) due to formation of CrN. It is noted that the transition from expanded austenite to nitrogen-free austenite is not associated with a gradual continuous decrease of the lattice parameter (or nitrogen content), but that a temperature range exists where both high- and low-nitrogen-containing austenite are present in the same sample. This observation can be related to the mechanism of the transformation, which is consistent with discontinuous precipitation, as previously demonstrated (Christiansen & Somers, 2006*b*). For the low-nitrogen-containing sample, the decomposition at a lower temperature showed the development of ferrite (presumably) during a eutectoid transformation. Ferrite formation is observed before CrN can be detected, which may be explained by coherent diffraction of small CrN particles with ferrite. Nitrogen-lean austenite developed at a higher temperature. Apparently, at temperatures well below the stabilization temperature for austenite, ferrite can develop, most likely promoted by a favourable Baker–Nutting orientation relationship between CrN and ferrite (Somers *et al.*, 1989). Evidently, at higher temperatures, a favourable interfacial energy at the interface between CrN and the matrix is insufficient to promote ferrite formation and austenite develops instead. It is hypothesized that the transformation of ε-M_2N_{1-z} to ferrite is, in principle, also possible. At high pressures, b.c.c. iron transforms into h.c.p. ε-Fe (Bundy, 1965). The presence of a high amount of nitrogen in the metallic lattice and the formation of ε-M_2N_{1-z} could be conceived as consequence of a 'high internal pressure' associated with nitrogen dissolution. The removal of interstitial nitrogen ('internal pressure') from ε-M_2N_{1-z} might induce the formation of ferrite.

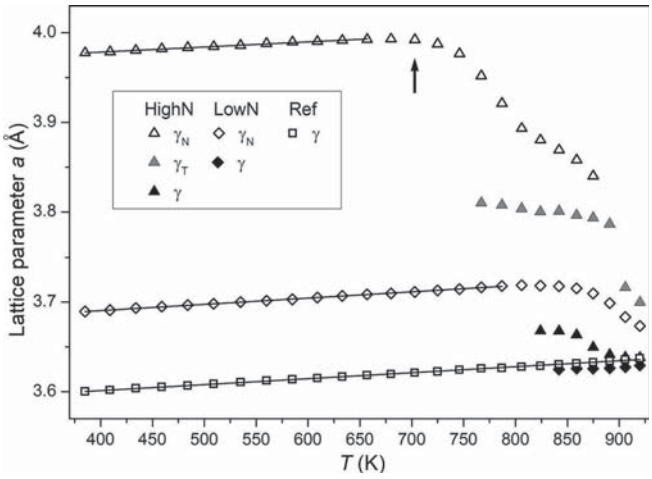

Figure 5
Lattice parameters for (expanded) austenite phases in all samples. Estimated standard deviations are $\leq 10^{-3}$ Å. The symbols in the legend are grouped by sample designation. Lines correspond to fitted expressions for thermal expansion. The start of N_2 formation is marked by an arrow.

4.2. Coefficient of thermal expansion

The coefficient of volumetric thermal expansion, α_{exp}, was determined in the form tabulated by Fei (1995) from fitting the following expression to the obtained data:

$$V(T) = V_{Tr} \exp\left[\int_{T_r}^{T} \alpha_{exp}(T)\,dT\right], \quad (1)$$

where V is the volume of the unit cell, V_{Tr} is the volume at a chosen reference temperature (T_r) and the thermal expansion coefficient is expressed in a polynomial form: $\alpha_{exp}(T) = a_0 + a_1T + a_2T^{-2}$. The number of data points did, however, only allow statistically reliable fits of a single parameter, a_0. The coefficients obtained are thus independent of temperature. In addition, the commonly used mean thermal expansion coefficient, α_{avg}, was fitted to the expression

$$V(T) = V_{Tr}[1 + \alpha_{avg}(T - T_r)], \quad (2)$$

which yielded similar values, implying that equation (1) can be truncated after the first term of the series expansion. The linear coefficient of thermal expansion was found by replacing the volume with the lattice parameter in the above expressions. The resulting fits of equation (1) are shown in Fig. 5 and all values obtained are presented in Table 2. The sample with low nitrogen content exhibits more thermal expansion than the untreated reference material, while the sample with the high nitrogen content has an expansion coefficient significantly lower than that of the other samples. This is explained by the underlying cause of the expansion, *i.e.* thermal vibra-

Table 2
Fitted coefficients of volumetric (V) and linear (a) thermal expansion for (expanded) austenite phases; α_{exp} and α_{avg} are defined by equations (1) and (2), respectively.

The value for γ'-Fe_4N (Somers, Van Der Pers *et al.*, 1989) is included for comparison.

Phase	T range (K)		α_{avg} ($\times 10^{-5}$ K^{-1})	α_{exp} ($\times 10^{-5}$ K^{-1})
γ_N (HighN)	385–657	V	4.32 (5)	4.30 (5)
		a	1.43 (2)	1.43 (2)
γ_N (LowN)	385–787	V	5.71 (2)	5.66 (2)
		a	1.891 (8)	1.886 (8)
γ (Reference)	385–920	V	5.60 (2)	5.53 (2)
		a	1.851 (7)	1.844 (7)
γ'-Fe_4N	293–773	–	–	–
		a	0.76 (8)	–

tions of composing atoms. The additional vibrations of the interstitial nitrogen atoms cause an added separation of the metal atoms with increasing thermal energy. The additional nitrogen vibrations are less significant for higher interstitial content where the average distance between the metal atoms is larger. In fact, the high-nitrogen sample exhibits the lowest thermal expansion owing to the large intermetallic distances, but the value is still almost twice that reported for γ'-Fe_4N (Somers, Van Der Pers *et al.*, 1989). No expansion coefficient could be determined for the M_4N phase that develops beyond 770 K. For reference, the linear expansion coefficient obtained for the ferrite phase, α_{avg}, is 1.131 (5) $\times$ 10^{-5} K^{-1}.

It is noted that the observation of a dependence of the thermal expansion coefficient on the nitrogen content has implications for the development of residual stress in expanded austenite zones developing on stainless steel. Residual stresses in expanded austenite are highly compressive and generally largely composition induced (Christiansen & Somers, 2009). A variation in thermal expansion coefficient over the thickness of the γ_N zone implies that during cooling an additional thermally induced stress profile develops, such that thermal stress is largest for the highest nitrogen content. The presently established difference in thermal expansion coefficient for high- and low-nitrogen-containing expanded austenite corresponds to an additional compressive stress of 500 MPa in high-nitrogen expanded austenite.

4.3. Stacking fault probability

Warren's model for describing the effect of stacking faults on X-ray diffraction results can readily be implemented in the Rietveld refinements in order to describe the systematic deviations in the positions of diffraction peaks for expanded austenite (Fig. 2*b*). The inadequacies of the model should not be ignored but even a rigorous treatment of the effects of stacking faults is insufficient to completely describe the structure, *e.g.* the different metallic environments observed with EXAFS (Oddershede *et al.*, 2008*a*, 2010).

The stacking fault probability obtained with Rietveld refinement of each of the X-ray diffractograms for the high-nitrogen sample is shown in Fig. 6 and remains approximately unaltered for temperatures up to 680 K. The presently

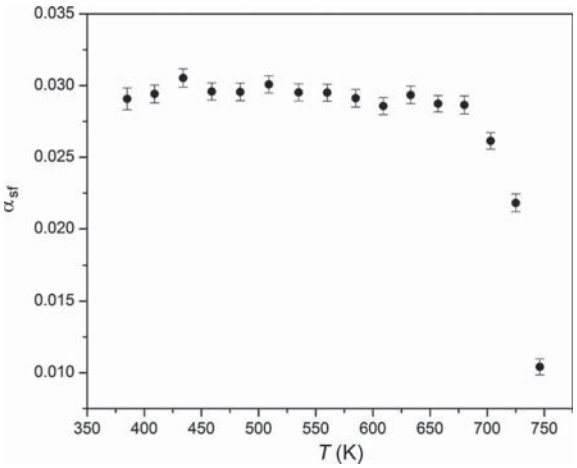

Figure 6
Refined stacking fault probability for expanded austenite *versus* temperature for the high-nitrogen sample. For the low-nitrogen sample the stacking fault probability is zero.

obtained values for the stacking fault probability ($\alpha_{sf} \simeq 0.03$) are in accordance with those previously obtained for homogeneous expanded austenite samples (Christiansen & Somers, 2004).

A sudden decline of the stacking fault probability was observed above 680 K, resulting in no observable induced peak shift above 750 K, where CrN development was first noticeable. Several hypotheses can be put forward to explain the observed decrease of the stacking fault probability. Firstly, a decrease of the nitrogen content in solid solution by N_2 formation could induce a reduction of the stacking fault density. Secondly, the segregation of N atoms (or CrN development) onto stacking faults, leading to clusters, causes the stacking faults to lose their identity. In any case it is clear that the stacking fault probability is related to the nitrogen content in solid solution, since it decreases with decreasing interstitial content for the high-nitrogen sample. The nitrogen content in the low-nitrogen sample is substantially lower, and no stacking-fault-induced peak shifts were observed in diffractograms for the low-nitrogen sample. The stacking fault probability is thus negligible for very low nitrogen contents.

5. Conclusions

Nitrogen-expanded austenite was produced from 5 µm AISI 316 powder. An *in situ* synchrotron X-ray diffraction investigation of the decomposition of expanded austenite with high ($y_N = 0.56$) and low nitrogen ($y_N = 0.14$) content shows that the development of CrN is promoted by a high nitrogen content. For a high nitrogen content, the formation of CrN is accompanied by the development of expanded austenite with a nitrogen content corresponding to M_4N ($y_N = 0.25$), consistent with (discontinuous) precipitation. For a low nitrogen content CrN forms along with ferrite, indicating a eutectoid transformation.

An interpretation of diffractograms of the high-nitrogen sample with Rietveld refinement necessitated the imple-

mentation of Warren's approximation for the effect of stacking faults on *hkl*-dependent shifts of Bragg reflections. The stacking fault density obtained through Rietveld refinement is constant up to 680 K; thereafter it reduces to nil, suggesting the effective disappearance of stacking faults. Although the contributions to peak broadening were not specifically taken into account, this simplified model allows for a consistent interpretation of diffraction data.

Linear thermal expansion coefficients for expanded austenite were obtained for the temperature range where expanded austenite is stable:

$y_N = 0.56$: $\alpha_{exp} = 14.3\ (2) \times 10^{-6}\ K^{-1}$, $385 < T < 657$ K,

$y_N = 0.14$: $\alpha_{exp} = 18.91\ (8) \times 10^{-6}\ K^{-1}$, $385 < T < 787$ K.

A decrease in thermal expansion coefficient with increasing nitrogen content is attributed to the additional expansion of the lattice as a consequence of the higher nitrogen content. Accordingly, the contribution of thermal vibrations to the expansion of the metal host lattice becomes less pronounced.

The authors are grateful to Danscatt for financing the measurement time at MAX-lab. The Danish Council for Independent Research (DFF) is gratefully acknowledged for financial support under grant No. 11-106293.

References

Babu, S. S., Specht, E. D., David, S. A., Karapetrova, E., Zschack, P., Peet, M. & Bhadeshia, H. K. D. H. (2005). *Metall. Mater. Trans. A*, **36**, 3281–3289.

Bundy, F. P. (1965). *J. Appl. Phys.* **36**, 616.

Cerenius, Y., Ståhl, K., Svensson, L. A., Ursby, T., Oskarsson, Å., Albertsson, J. & Liljas, A. (2000). *J. Synchrotron Rad.* **7**, 203–208.

Christiansen, T. L., Hummelshøj, T. S. & Somers, M. A. J. (2010). *Surf. Eng.* **26**, 242–247.

Christiansen, T. & Somers, M. A. J. (2004). *Scr. Mater.* **50**, 35–37.

Christiansen, T. & Somers, M. A. J. (2005). *Surf. Eng.* **21**, 445–455.

Christiansen, T. & Somers, M. A. J. (2006*a*). *Metall. Mater. Trans. A*, **37**, 675–682.

Christiansen, T. & Somers, M. A. J. (2006*b*). *Z. Metallkd.* **97**, 79–88.

Christiansen, T. L. & Somers, M. A. J. (2009). *Int. J. Mater. Res.* **100**, 1361–1377.

Dong, H. (2010). *Int. Mater. Rev.* **55**, 65–98.

Fei, Y. (1995). *AGU Reference Shelf 2: Mineral Physics and Crystallography*, pp. 29–44. Washington, DC: AGU.

Fewell, M. & Priest, J. (2008). *Surf. Coat. Technol.* **202**, 1802–1815.

Fossati, A., Borgioli, F., Galvanetto, E. & Bacci, T. (2006). *Corros. Sci.* **48**, 1513–1527.

Frandsen, R. B., Christiansen, T. & Somers, M. A. J. (2006). *Surf. Coat. Technol.* **200**, 5160–5169.

García Molleja, J., Milanese, M., Piccoli, M., Moroso, R., Niedbalski, J., Nosei, L., Bürgi, J., Bemporad, E. & Feugeas, J. (2013). *Surf. Coat. Technol.* **218**, 142–151.

Grabke, H. J. (1968). *Ber. Bunsenges. Phys. Chem.* **72**, 533–541.

Howard, C. J. & Hill, R. J. (1986). *AAEC Report M112* (now ANSTO), Lucas Heights Research Laboratory, Australia.

Hummelshøj, T. S., Christiansen, T. L. & Somers, M. A. J. (2010). *Scr. Mater.* **63**, 761–763.

Kjeldsen, D. B. (2013). MSc thesis, Technical University of Denmark.

Li, C. X. & Bell, T. (2004). *Corros. Sci.* **46**, 1527–1547.

Li, X., Sun, Y. & Bell, T. (1999). *Z. Metallkd.* **90**, 901–907.

Martinavičius, A., Abrasonis, G., Scheinost, A. C., Danoix, R., Danoix, F., Stinville, J. C., Talut, G., Templier, C., Liedke, O., Gemming, S. & Möller, W. (2012). *Acta Mater.* **60**, 4065–4076.

Oddershede, J., Christiansen, T. L. & Ståhl, K. (2008*b*). *J. Appl. Cryst.* **41**, 537–543.

Oddershede, J., Christiansen, T. L., Ståhl, K. & Somers, M. A. J. (2008*a*). *J. Mater. Sci.* **43**, 5358–5367.

Oddershede, J., Christiansen, T. L., Ståhl, K. & Somers, M. A. J. (2010). *Scr. Mater.* **62**, 290–293.

Öztürk, O. & Williamson, D. L. (2002). *Surf. Coat. Technol.* **158–159**, 288–294.

Öztürk, O. & Williamson, D. L. (1995). *J. Appl. Phys.* **77**, 3839.

Rivière, J. P., Templier, C., Declémy, A., Redjdal, O., Chumlyakov, Y. & Abrasonis, G. (2007). *Surf. Coat. Technol.* **201**, 8210–8214.

Somers, M. A. J., Kooi, B. J., Maldzinski, L., Mittemeijer, E. J., Van Der Horst, A. A., Van Der Kraan, A. M. & Van Der Pers, N. M. (1997). *Acta Mater.* **45**, 2013–2025.

Somers, M. A. J., Lankreijer, R. M. & Mittemeijer, E. J. (1989). *Philos. Mag. A*, **59**, 353–378.

Somers, M. A. J., Van Der Pers, N. M., Schalkoord, D. & Mittemeijer, E. J. (1989). *Metall. Trans. A*, **20**, 1533–1539.

Stróz, D. & Psoda, M. (2010). *J. Microsc.* **237**, 227–231.

Velterop, L., Delhez, R., de Keijser, Th. H., Mittemeijer, E. J. & Reefman, D. (2000). *J. Appl. Cryst.* **33**, 296–306.

Warren, B. E. (1990). *X-ray Diffraction*, §13.5. New York: Dover Publications Inc.

Xiaolei, X., Liang, W., Zhiwei, Y. & Zukun, H. (2005). *Surf. Coat. Technol.* **192**, 220–224.

Xu, X., Wang, L., Yu, Z., Qiang, J. & Hei, Z. (2000). *Metall. Mater. Trans. A*, **31**, 1193–1199.

Appendix B

Additional experimental details

B.1 Synthesis of expanded austenite: Annealing and activation

In order to avoid formation of chromium nitrides and carbides, which are detrimental to the corrosion resistance and may promote decomposition of expanded austenite, long processing times should be avoided. Figure B.1 shows the diffractogram of an expanded austenite sample synthesized from 12.5 μm AISI 316 foil. All diffraction data shown in this section was obtained with an Agilent SuperNova diffractometer with an Atlas S2 CCD detector using Mo K_α radiation and calibrated with a LaB_6 standard. Note that, although diffractograms contain both $K_{\alpha 1}$ and $K_{\alpha 2}$ components, the conversion to q-space is done with a single intensity-averaged wavelength, $\lambda = 0.7107$ Å.

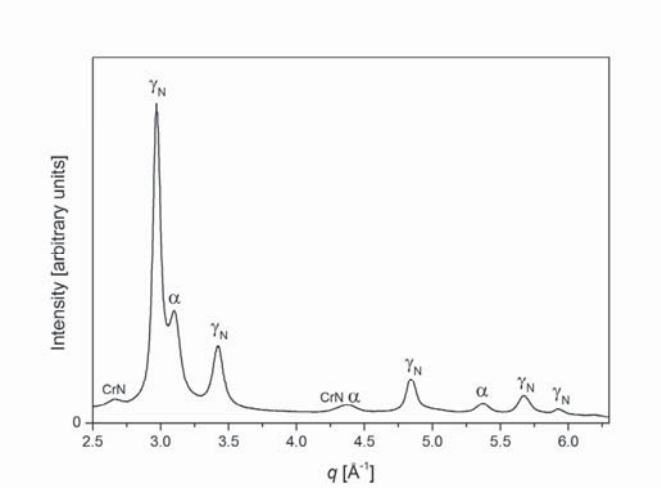

Figure B.1: Diffractogram of 12.5 μm AISI 316 foil nitrided at 693 K in NH_3 for 38 hours and denitrided in H_2 for 8 hours. Phase identifiers are included for the main peaks; nitrogen expanded austenite (γ_N), ferrite (α) and chromium nitride (CrN).

During gaseous nitriding in NH_3 at 693 K, a processing time of 38 hours was needed in order to saturate the sample and subsequently 8 γ_N hours in H_2 to retract all loosely bound nitrogen. It is clearly seen from Figure B.1 that, in addition to expanded austenite, ferrite and chromium nitride have developed, which is undesirable. Prior to nitriding, the foil was briefly annealed at 1323 K in flowing H_2 for recrystallization and transformation of deformation-induced martensite in order to obtain a completely austenitic material. The presence of deformation-induced martensite in the as-received cold-rolled foil can clearly be seen from the diffraction pattern in Figure B.2(*a*) (faint third and fifth ring from the center). In addition, texture is noticed from the non-uniform distribution of intensity.

After annealing (Figure B.2*b*) there is no martensite and individual diffraction spots are seen for austenite, signifying recrystallization and grain growth. During nitriding the average size of the coherently diffracting domains is apparently decreased, as assessed from the irregularity of diffraction rings in Figure B.2(*c*), which seem to be somewhere between perfect powder rings and individual spots.

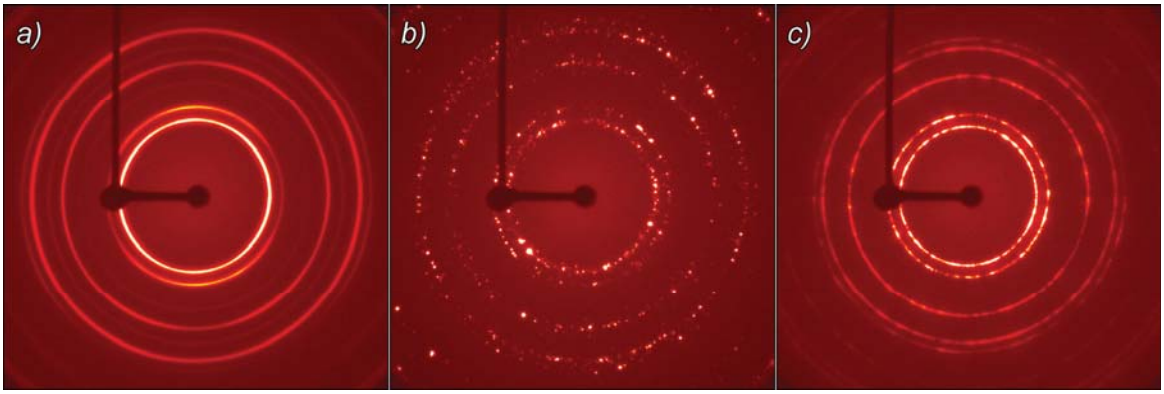

Figure B.2: Diffraction patterns for 12.5 μm AISI 316 foil *a*) as received showing textured diffraction rings of austenite and martensite, *b*) annealed in H_2 at 1323 K showing individual diffraction spots for austenite and *c*) nitriding at 693 K in NH_3 for 49 hours showing irregular diffraction rings.

Saturated thin foils of expanded austenite do tend to become brittle and fall apart, easily being reduced to powder. The apparent decrease in size of coherently diffracting domains is, however, evident even when it is present as a coherent foil like the one shown in Figure B.3.

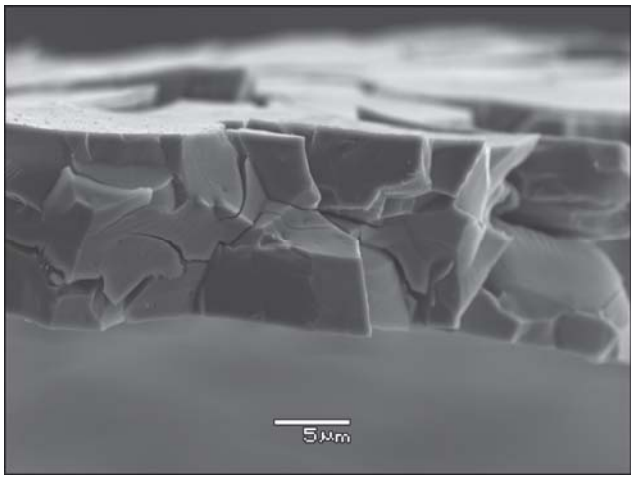

Figure B.3: SEM micrograph of nitrided 12.5 μm AISI 316 foil fracture surface. The brittle nature of the material is clearly seen from the cracks formed throughout the foil.

B.1.1 Annealing

Since there is a clear change in microstructure between annealed and nitrided states, the effects of lowered annealing temperature was investigated in order to repress grain growth while still obtaining full transformation of martensite to austenite. Samples were annealed using a Netzsch STA 449 F3 Jupiter thermal analyzer with a H_2 flow rate of 250 mL/min and a N_2 flow of 5 mL/min for protection of electronics in the measurement compartment. The heating rate was 30 K/min until reaching the desired temperature, immediately followed by cooling to room temperature at a rate of 50 K/min.

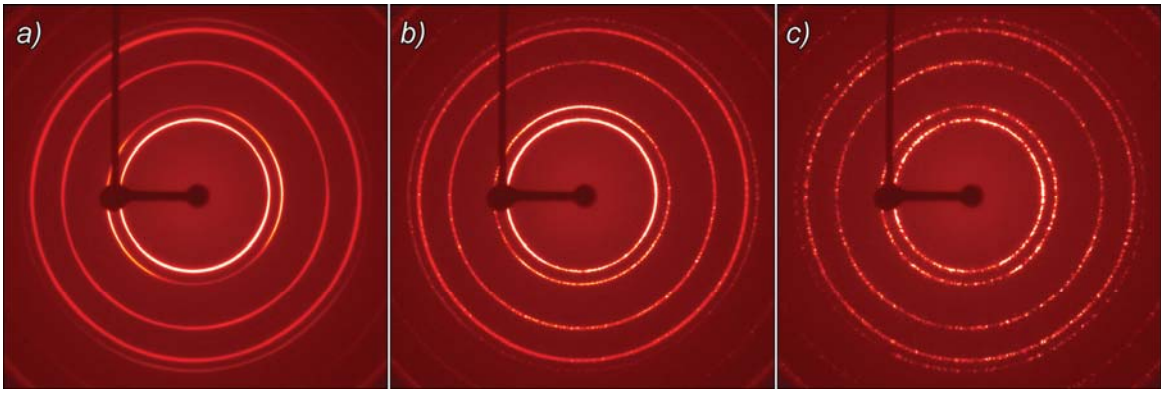

Figure B.4: Diffraction patterns for 12.5 μm AISI 316 foil annealed in H_2 at *a*) 973 K, *b*) 1073 K and *c*) at 1173 K showing increased recrystallization and grain growth with increasing temperature.

The change in texture as well as grain growth as individual diffraction spots become noticeable is evident from Figure B.4. Note that the differences in direction of increased (200) intensity between 973 K and 1073 K is caused simply from orientation of the foil when recording the diffraction pattern. The integrated diffractograms in Figure B.5(*a*) and (*b*) show the change in texture. Relative intensities approach that of an ideal powder for an annealing temperature of 1173 K. In addition, the widths of diffraction peaks decrease due to grain growth and the individual $K_{\alpha 1}$ and $K_{\alpha 2}$ components can be distinguished.

Traces of the deformation-induced martensite in the cold rolled foil is still present after annealing at 973 K but is effectively transformed to austenite at temperatures above 1073 K (Figure B.5*c-e*). Consequently, the nitriding behavior of a foil annealed at 1073 K was compared to conventional annealing at 1323 K. Following activation, both foils were nitrided in NH_3 at 693 K and the annealing temperature does in fact affect the nitriding rate (Figure B.6*a*). The diffusion rate of nitrogen into the material is highest for the large grains obtained for annealing at 1323 K. In addition to the lower reaction rate caused by annealing at 1073 K also the apparent saturation level is lower; ~12 mass% as compared to ~13 mass% for the sample annealed at higher temperature.

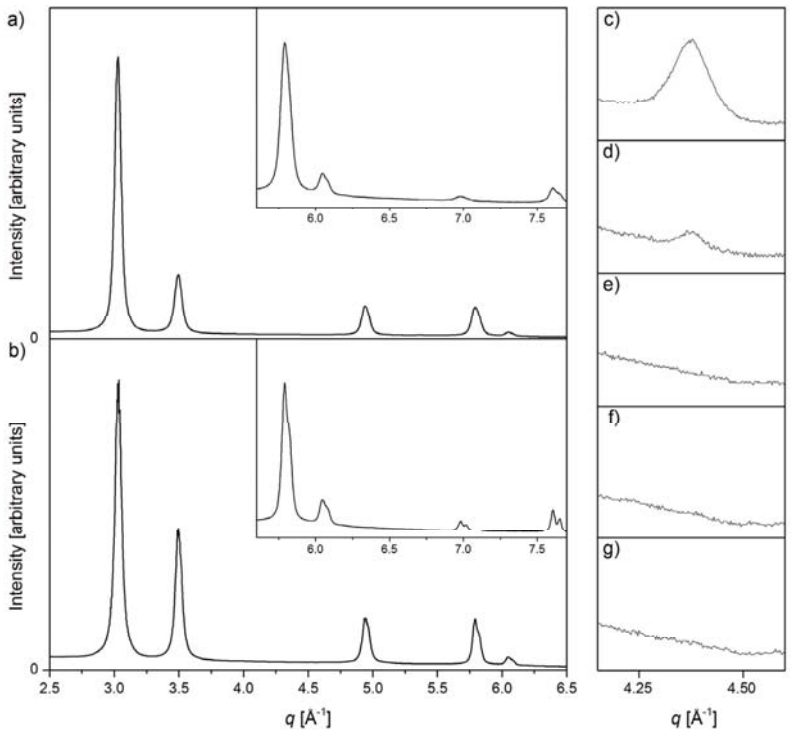

Figure B.5: Diffractograms of 12.5 μm AISI 316 foil annealed at *a*) 973 K and *b*) 1173 K; insets show the high q range and the position of the (200) martensite peak is shown for *c*) as received sample *d*) annealed at 973 K, *e*) 1073 K, *f*) 1173 K and *g*) 1323 K.

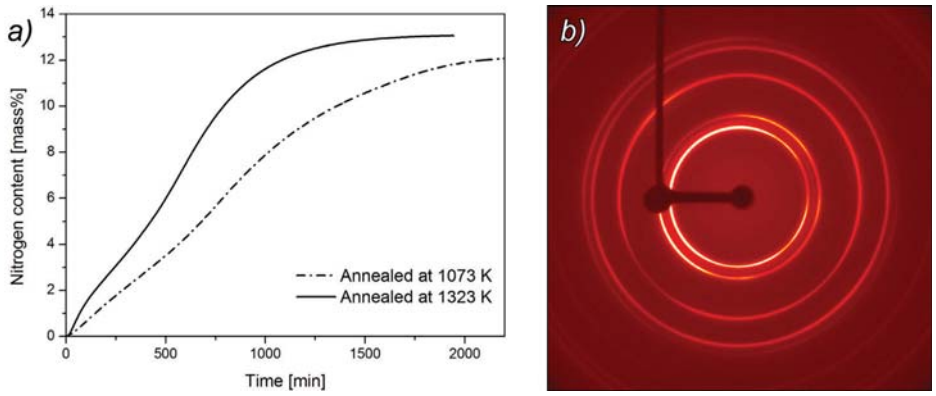

Figure B.6: *a*) Comparison of thermogravimetric curves for nitriding at 693 K of 12.5 μm AISI 316 foil annealed 1073 and 1323 K and *b*) diffraction pattern for sample annealed at 1073 K, then nitrided in NH_3.

Annealing at 1073 K, followed by nitriding, produces a microstructure quite similar to that of the annealed foil (Figure B.6*b*). This may, however, be caused by the lower nitrogen content, which makes the material less brittle and thus less likely to fragment into smaller crystallites. The microstructure of the steel surface clearly affects the nitriding behavior, but the long processing time to reach saturation causes formation of chromium nitrides and ferrite upon subsequent denitriding to reach the desired composition. Since lowering the annealing temperature actually increases the required nitriding time and lowers the maximum obtained nitrogen content, the effect of changing the applied activation process was investigated.

B.1.2 Activation

The success in nitriding the 5 μm powder samples described in Chapter 6 implies that diffusion distances in 12.5 μm AISI 316 foils are too long to obtain homogeneous saturated samples with this applied nitriding procedure. To verify this, 30 μm AISI 316 foils were chemically thinned in a solution of ethanol and concentrated nitric and hydrochloric acid to an average thickness < 10 μm assessed from mass loss. From visual inspection the thinnest parts were selected, annealed in H_2 at 1273 K and nitrided in NH_3 for 15 hours at 693 K.

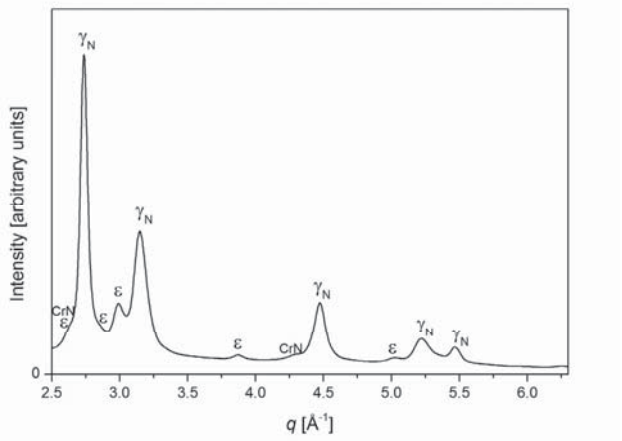

Figure B.7: Diffractogram of AISI 316 foil chemically thinned in $HNO_3/HCl/C_2H_5OH$ solution, annealed at 1273 K and nitrided in NH_3 for 15 hours at 693 K. Phase identifiers are included for the main peaks; nitrogen expanded austenite (γ_N), ε-nitride and chromium nitride (CrN).

The required processing time is greatly reduced, but ε-nitride and CrN are formed (Figure B.7), probably caused by the uneven thickness distribution produced by the chemical thinning of this trial experiment. Consequently, some parts will be saturated faster followed by formation of nitrides, while the nitrogen content in thicker parts is still increasing. Homogeneous foils were therefore synthesized by changing the activation procedure to that

described in Section 6.4, which involves chemical stripping of the passive film, followed by electrochemical deposition of Ni in a Wood's nickel bath ($NiCl_2$ + $NiSO_4$ + H_2SO_4). Prior to activation, foils were annealed at 1323 K in H_2.

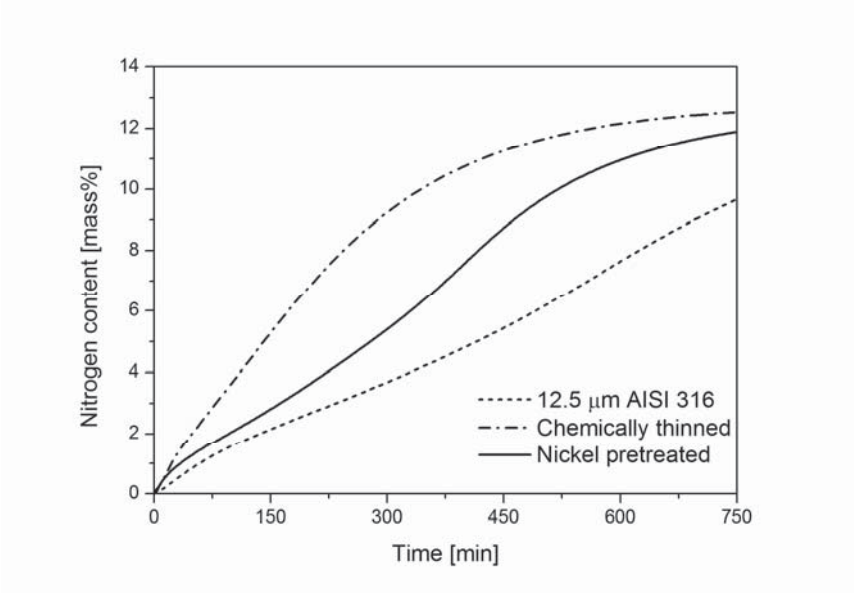

Figure B.8: Comparison of initial part of thermogravimetric curves for nitriding of AISI 316 foil at 693 K: 12.5 μm, chemically thinned and nickel pretreated foil.

The nitriding rate of the Ni-activated sample is between that of the 12.5 μm and the chemically thinned foil (Figure B.8). No trace of nitride formation was observed. In addition to the fully saturated sample, three samples were synthesized in NH_3/H_2 gas mixtures with nitriding potentials, K_N, adjusted to 2.40, 0.07 and 0 ($atm^{-1/2}$) after full saturation was achieved, analogous to the low nitrogen sample in Chapter 6. The denitrided samples contain nitrogen expanded austenite of composition corresponding to the chosen nitriding potentials. Trace amounts of ferrite was indicated by X-ray diffraction for the sample with zero nitriding potential but was not evident in Mössbauer spectra (see Section 6.4). Diffractograms are shown in Figure B.9.

The required nitriding time is thus sufficiently reduced by the nickel pretreatment to obtain saturated nitrogen expanded austenite while nitride formation is avoided. These samples therefore formed the basis for characterization of structural and magnetic properties of nitrogen expanded austenite in Section 6.4. The deposited nickel constitutes a negligible fraction of the foils and should thus not influence the characterization.

Note that an increased treatment temperature would also reduce the required nitriding time but could also promote nitride formation. The temperature of 693 K was kept due to this being used for the powder samples described in Section 6.1. Finally, it should be noted that for similar experiments performed at 718 K with lower amounts of sample, the

otherwise used proprietary process for surface activation has been sufficient in order to obtain a satisfactory treatment time.

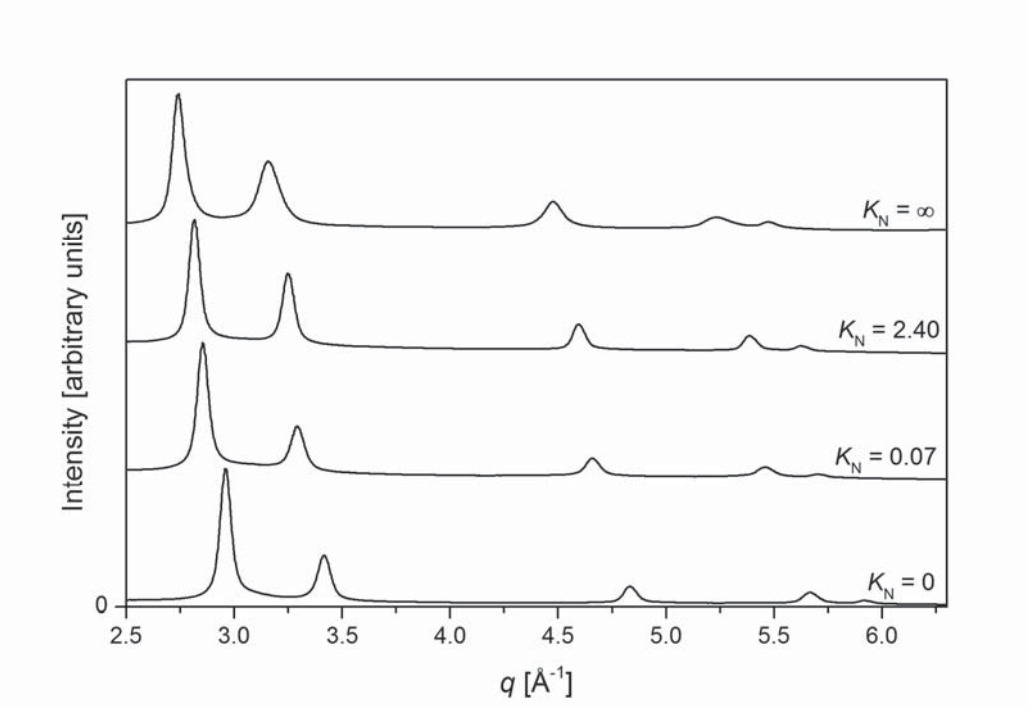

Figure B.9: Diffractograms of 12.5 μm AISI 316 foils annealed at 1323 K and nitrided in NH_3 at 693 K. Nitriding potentials less than infinity were applied after full saturation was achieved. A higher nitriding potential corresponds to higher nitrogen content and thus larger shifts towards lower q. Nitriding potentials are given in $atm^{-1/2}$.

For higher sample amounts, crucibles are more densely packed with steel foils and this apparently affects the ability of nitrogen to enter the steel from the gas phase. This is presumably caused by reduced local flow of ammonia around the available surface. Nickel activation has thus only been necessary for these experiments were a maximum sample yield was required in order to obtain sufficient material for all analyses of the same homogeneous sample.

B.2 X-ray Raman Spectroscopy

Characterization of interstitial solid solutions of nitrogen and/or carbon in iron-based lattices based on X-ray methods, like diffraction and absorption spectroscopy, primarily yields information on the metallic structure. This is due to the low energy absorption edges and low scattering factors for atoms with low atomic number compared to the metallic elements. Only a few experimental methods can potentially directly probe nitrogen and carbon in iron-based metallic matrices, one of which is X-ray Raman Spectroscopy (XRS).

As the name suggests, XRS is comparable to Raman scattering where inelastic scattering of photons in the near infrared to ultraviolet range is used to study vibrational, rotational and other low-frequency modes. XRS is based on non-resonant inelastic scattering of X-rays from core electrons. The excitation of core electrons is analogous to X-ray absorption spectroscopy but instead of absorption, energy transfer is measured using hard (high energy) X-rays. Soft X-ray spectra contain element-specific information of local structure and chemistry of light elements, but studies are constrained by the low probe depth of the low energy radiation. The surface sensitivity is overcome by using hard X-rays to obtain bulk structural information. The energy transfer, ΔE, of an inelastically scattered photon with initial energy E_0 results in a photon with final energy E_f. A spectrum of $\Delta E = E_0 - E_f$ is obtained by changing the incident energy while the final energy is fixed to E_f with analyzer crystals.

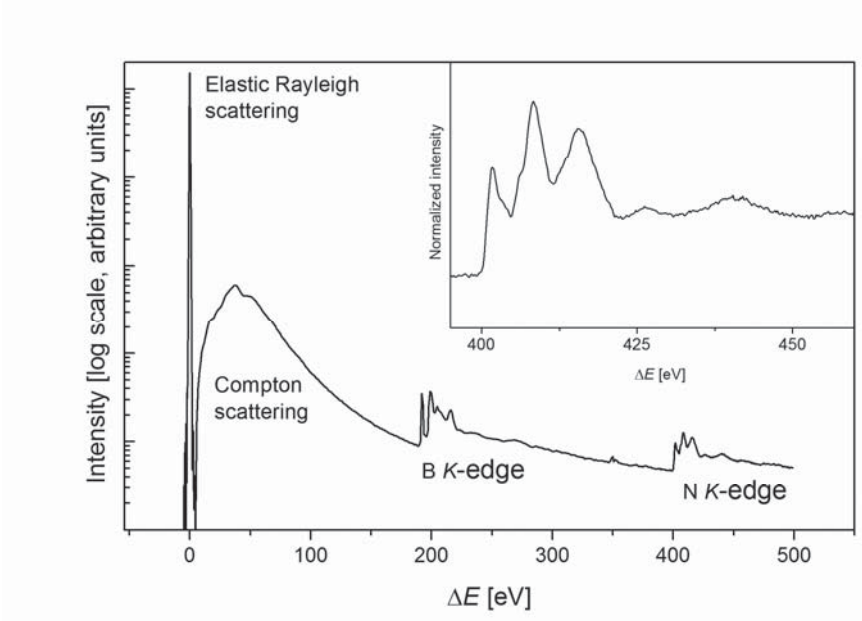

Figure B.10: Full XRS spectrum (low-q) of BN sample showing Rayleigh and Compton scattering and K-edges of nitrogen and boron (logarithmic scale). Inset shows normalized spectrum of the nitrogen K-edge (linear scale).

Figure B.10 shows a full XRS spectrum from forward scattering angles (low-q) obtained for boron nitride, BN, where Rayleigh and Compton scattering, as well as K-edges, of both nitrogen and boron can be seen. Similar edges were observed for analyzers positioned at backscattering angles (high-q). Measurements were performed at beamline ID20 at ESRF using 72 Si(660) analyzer crystals (3 horizontal and 3 vertical modules of 12 analyzers each) with an incident photon energy of approximately 10 keV.

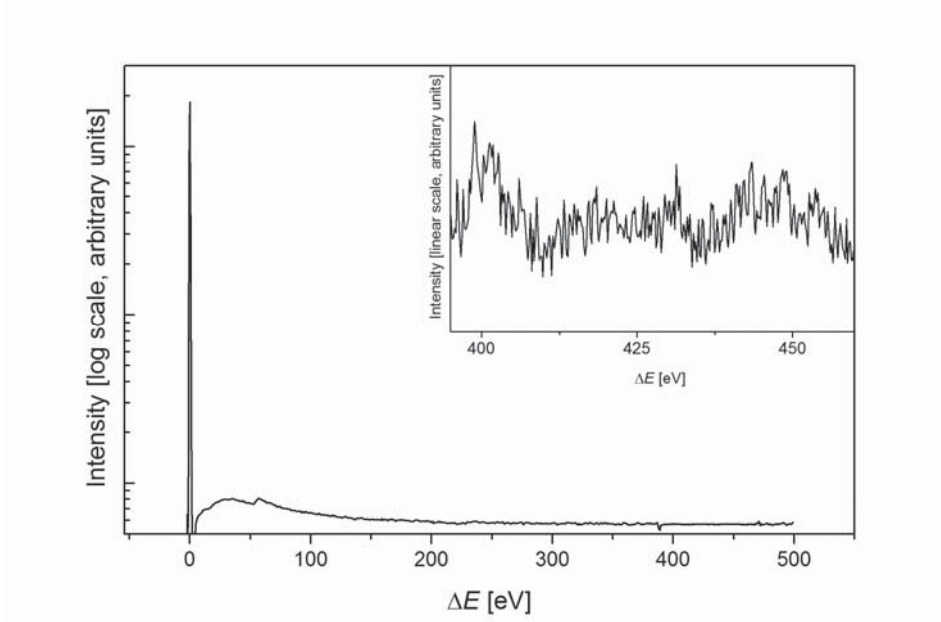

Figure B.11: Full XRS spectrum (low-q) of nitrogen expanded austenite sample (logarithmic scale). Inset shows the barely discernable nitrogen K-edge (linear scale); compare to Figure B.10.

The nitrogen K-edge is barely discernable in the low-q spectrum obtained for expanded austenite, even with measurement times up to 14 hours (Figure B.11), compared to one hour for the BN spectrum (Figure B.10). Similar observations apply to the high-q spectrum and consequently no structural information can be extracted. XRS was also performed for samples of ε-iron carbonitrides, again with no distinct carbon or nitrogen edges.

The lack of observable edges may be caused from fluorescent radiation from the samples adding to the background, or simply be caused by absorption from the relatively dense metallic structures, suppressing the signal from the light elements. In any case, signals from carbon and nitrogen cannot be adequately resolved from the background, even for samples containing more than 30 atomic percent nitrogen. Structural information from direct probing of nitrogen and carbon does therefore not seem attainable from XRS spectra of ε-iron carbonitrides or expanded austenite.

DTU Mechanical Engineering
Section of Materials and Surface Engineering
Technical University of Denmark

Produktionstorvet, Bld. 425
DK- 2800 Kgs. Lyngby
Denmark
Phone (+45) 4525 2205
Fax (+45) 4593 6213
www.mek.dtu.dk
ISBN: 978-87-7475-427-5